JAERI-Review
96-006

JAERI-Review--96-006
JP9607021

GROWTH OF LARGE ISOMETRIC $YBa_2Cu_3O_x$ SINGLE CRYSTALS AND THEIR FLUX PINNING PROPERTIES

March 1996

Hidehito ASAOKA

日本原子力研究所
Japan Atomic Energy Research Institute

本レポートは，日本原子力研究所が不定期に公刊している研究報告書です。
入手の問合わせは，日本原子力研究所技術情報部情報資料課（〒319-11 茨城県那珂郡東海村）あて，お申し越しください。なお，このほかに財団法人原子力弘済会資料センター（〒319-11 茨城県那珂郡東海村日本原子力研究所内）で複写による実費頒布をおこなっております。

This report is issued irregularly.
Inquiries about availability of the reports should be addressed to Information Division, Department of Technical Information, Japan Atomic Energy Research Institute, Tokai-mura, Naka-gun, Ibaraki-ken 319-11, Japan.

編集兼発行　日本原子力研究所
印　　刷　㈱原子力資料サービス

JAERI-Review 96-006

Growth of Large Isometric $YBa_2Cu_3O_x$ Single Crystals and Their Flux Pinning Properties

Hidehito ASAOKA

Department of Material Science and Engineering
Tokai Research Establishment
Japan Atomic Energy Research Institute
Tokai-mura, Naka-gun, Ibaraki-ken

(Received February 22, 1996)

Large, isometric and high-quality single crystals of $YBa_2Cu_3O_x$ (123), which are undoubtedly one of the most important materials for understanding the origin of high-temperature superconducting transitions (T_c) above liquid nitrogen temperatures, have successfully been grown from a mixed region of solid Y_2BaCuO_5 (211) and melt. The crystals have sharp, shiny habits with a maximum thickness of about 7 mm along the c-axis. The best growth condition is that the solvent composition is $7BaCuO_2 \cdot 11CuO$, which is close to the binary eutectic of $BaCuO_2$-CuO, and the optimum concentration of the growth system is that the ratio of 1/6 (123) to 1/25 ($7BaCuO_2 \cdot 11CuO$) equals 3:7. The use of Y_2O_3-crucibles prevents contamination from containers during growth, and facilitates the synthesis of high-purity crystals. Temperature gradient and seed crystals are both effective for controlling nucleation.

The annealed crystals have a sharp superconductive transition at 91 K. The temperature dependence of the resistivity is found to be metallic in the $a(b)$- as well as the c-direction. Sufficient diamagnetism is manifested as a sharp transition at T_C with a complete shielding effect at temperatures below T_C. Remarkable anisotropy, in the broadening of the resistive transition, can be observed under magnetic fields parallel or perpendicular to the c-axis.

Investigations on the crystal growth mechanism of the 123 crystal have revealed the occurrence of diffusion of the 123 phase to the surrounding melt in three-phase, 123, 211 and the melt, region. This fact suggests the solubility of the 123 phase to the

melt, and induction of Ostwald ripening, which acts on the solid-melt interfaces to lower the interface free energy of the growing crystals. These lead to the growth of 123 crystals which progresses due to the peritectic reaction between the 211 solid and the surrounding melt phase.

The study of critical current density (J_c) is quite important both for fundamental studies of superconductivity and for practical applications. The enhancement of J_c is associated with various crystalline imperfections such as point defect, void, dislocation, twin boundary, strain field and so on. These imperfections may return the superconducting state to normal with an increase in the magnetic field or temperature, and consequently, work as pinning centers of the vortices. In this study, we have focused on the relationship between J_c and crystalline imperfections in 123 single crystals which have been grown from various conditions as a result of the coexistence of the 211 solid and the melt phase. By decreasing the melt composition, an increase in the concentration of the voids are observed. These voids enhance the Meissner fractions, J_c and also the effective pinning energy. These facts indicate strong flux pinning due to the voids.

The effect of the twin boundaries on J_c has been studied by using densely twinned and perfectly detwinned domains in the same 123 single crystal. The most successful thermomechanical detwinning of the 123 crystals is observed in a treatment in inert gas. The influence of the twin boundaries on J_c depends on temperature. At low temperatures, J_c of the twinned domain has a smaller value than that of the detwinned one. However, as the temperature increases, the twin boundaries works as being strong pins and J_c of the twinned domain provides a larger value than that of the detwinned one.

Keywords: Oxide Superconductor, Single Crystal, $YBa_2Cu_3O_x$ Crystal Growth, Flux Pinning, Critical Current Density, Twin Boundary

大形$YB_2Cu_3O_x$単結晶育成と磁束ピンニング特性

日本原子力研究所東海研究所材料研究部
朝岡　秀人

(1996年2月22日受理)

本論文では、酸化物超伝導体$YBa_2Cu_3O_x$の単結晶育成と結晶成長機構、並びに結晶性とピンニング特性について述べる。以下にその概要を示す。

1. 大形$YBa_2Cu_3O_x$単結晶育成

$YBa_2Cu_3O_x$(123)結晶は液体窒素温度77Kを越える高い超伝導転移温度(T_c)を示し安定した結晶構造を持つ物質として注目されており、大形で高品質な単結晶による研究は超伝導特性の解明に不可欠であると共に、応用分野への発展が期待されている。一般に均一な溶液から123結晶を合成した場合、多くは小形板状晶しか得られず厚さ(c軸)方向の物性測定が極めて困難な状況にある。そこで等温に近い状態で固体と液体を共存させ、次に示すような包晶反応を用いて大形単結晶の育成を試みた。

$$Y_2BaCuO_5(\text{固相}) + \text{液相} \rightarrow YBa_2Cu_3O_x(\text{固相}) \quad (1)$$

固相反応法を用いて合成した123粉末と、$BaCuO_2$-CuOの共晶点を示す$7BaCuO_2$-11CuOとの比率を系統的に変化させ混合しY_2O_3るつぼに充填した。Y_2O_3るつぼの使用により、るつぼ材からの123相への不純物の混入を防ぎ高純度単結晶の育成が可能となる。出発混合物質をY_2BaCuO_5(211)と液相の2相共存状態が得られる1050℃まで昇温・保持した後、徐冷法による結晶成長を行い、970℃において123結晶と残留溶液を分離した。1/6(123)と1/25($7BaCuO_2$-11CuO)との比率を3：7に混合した出発組成について、最大7×7×7 mm^3 (a×b×c軸)程に成長し光沢のあるフラットな面{100}、{001}で囲まれた立方状結晶が得られ、さまざまな条件下で酸素アニールを行うことによりシャープな超伝導転移を示す酸素量x = 7.0の均一な123結晶を得ることができた。各方位に対する抵抗率-温度特性に関してa(b)、c軸方向いずれも$T > T_c$において金属的振舞いがみられ、c軸方向の抵抗率はa(b)軸方向のおよそ100倍程高い値を示した。また各方位に対して超伝導転移幅(ΔT_c)の外部磁場依存性を測定した結果、測定電流方向によらずc軸方向に磁場を印加した場合にΔT_cの低温側へのシフトが観測された。

東海研究所：〒319－11　茨城県那珂郡東海村白方白根2－4

2. 結晶成長機構

大形で高品質な123結晶を得ることができた固液共存状態からの結晶成長は123相、211相、液相が共存する領域において包晶反応(1)が主な役割を果たしていると考えられるが、Y_2O_3-BaO-CuO系における3相共存領域の存在は3成分系以上でのみ許される極めて珍しいもので、この系でも未だ完全に確認されていない。また、3相共存領域が123相の結晶成長に有利に作用するか否かも仮説の段階である。そこで各成長段階にある固液共存状態をクエンチし、包晶反応を伴う固液界面の観察を試みた。溶液温度の低下に伴い、固相(211)と液相の共存状態から、211相、反応生成物(123)との包晶組織の存在する3相共存領域が確認され、最終的には123相への進行が観察された。3相共存領域において、包晶相表面から反応生成物(123)の液相への拡散がみられたことから、123粒子の間では表面自由エネルギーの差異に起因するオストワルド成長が進行しうる環境が存在し、最終的には∞の粒径を持つ平面結晶の成長が得られたと考えられる。

3. 育成環境と磁束ピンニング特性

液相が溶質の移送を担う固液共存状態からの結晶成長において、液相量の変化は得られる123単結晶の結晶性に大きく影響を与えると考えられる。第2種超伝導体である123結晶は $T < T_c$ において外部磁場の増加に伴い混合状態となるが、無損失で流しうる臨界電流密度（J_c）の大きさは、侵入した量子化磁束を止めておくための結晶内の欠陥や析出物などのピン止め力に大きく影響を受ける。また層状構造に起因する異方性が極めて大きい酸化物高温超伝導体においては高品質な単結晶がピン止め機構の研究には不可欠である。固液共存状態における液相比率を系統的に減少させ123結晶を育成した結果、結晶内に液相比率の減少に伴いボイドが現われると共にボイドの密度の上昇がみられた。結晶内に不純物相の析出はみられず、酸素アニールを行った結晶はいずれも92.5Kにシャープな超伝導転移を示し均一な123相が得られていた。ただし液相比率の減少に伴い、5～80Kすべての温度域においてJ_cに比例する磁化のヒステリシス曲線の幅（ΔM)が増加し、1T、80KにおいてJ_cが10倍程の上昇を示した。磁化の時間緩和曲線から求められる磁束の活性化エネルギーも液相比率の減少に伴い増加し、ピン止め力の増加が示された。

4. 双晶境界と量子化磁束運動

不定比酸素を持つ123結晶は酸素の増加に伴う正方晶系から斜方晶系への相転移の際に双晶となる。双晶境界が量子化磁束に対しいかなる影響を及ぼすかについてさまざまな議論がなされているが、比較的微小な影響である上に、双晶境界のない高品質な123単結晶を得ることが困難であるため明確な結論が得られていない。そこで液相量が十分に存在する固液共存状態から育成された最も高品質の123結晶の双晶境界を除去し、双晶領域との比較検討を行った。不活性ガスによるアニーリングを行い、再び正方晶系に相転移させた123結晶に対して$a(b)$軸方向から加圧を行いつつ酸素を導入した結果、同一123結晶内に双晶領域と完全に双晶境界のない領域を得ることができた。これらは同一結晶内から得られたため双晶境界の有無以外は全く同一の結晶性を持つ。酸素アニーリングを行った結晶はいずれも92.5Kにシャープな超伝導転移を示す酸素量 $x = 7.0$の均一な123相が得られた。磁化のヒステリシス曲線において5～20Kの低温域では双晶領域のΔMの

減少がみられたが、60～84Kの高温域では逆転しΔMの増加が見られる。つまり高磁場中の低温域では双晶境界に沿った量子化磁束の結晶外へのはきだしが行われていたが、温度の上昇と共に量子化磁束の束としての運動が主になり双晶境界に沿ったはきだしが困難となった結果、逆に双晶境界が量子化磁束の運動を阻害する方向に作用したと考えられ、双晶境界と量子化磁束との関係が温度によって顕著に変化することが示された。

なお以上の内容は下記の論文を取りまとめ新たに考察を加えたものである。

1) H. Asaoka *et al.*: Physica C 190 (1991) 64-66.
2) H. Asaoka *et al.*: Jpn. J. Appl. Phys. 32 (1993) 1091-1096.
3) H. Asaoka *et al.*: Jpn. J. Appl. Phys. 33 (1994) L923-926.
4) H. Asaoka *et al.*: Physica C (to be published).
5) H. Asaoka *et al.*: Physica C (to be published).

Contents

目　　次

Chapter 1. Introduction

In mid-1987, the initial discovery by Bednorz and Müller of the 35 K superconductivity in the La-Ba-Cu-O system[1] stimulated the search for higher-temperature superconductors worldwide. Elemental substitution proved to be most effective for rising the transition temperature, and the substitution of Sr for Ba was able to produce 40 K superconductivity.[2] Less than a year later, the substitution of Y for La produced a new high-temperature superconductor[3] using formula $YBa_2Cu_3O_x$ with a transition temperature of 90 K which is much higher than the boiling point of liquid nitrogen. Superconducting compounds of the form $RBa_2Cu_3O_x$ have been explored by further substitutions of other types of rare earth (R) for Y. All these high-temperature superconductors required a rare earth, an alkaline earth, copper and oxygen. In 1988, superconductivity in rare-earth-free systems, Bi-Sr-Ca-Cu-O[4] and Tl-Ba-Ca-Cu-O,[5] with the superconductive transition between 110 and 125 K were reported. Recently, superconductivity above 130 K in the Hg-Ba-Ca-Cu-O[6] system has been reported.

Among these oxide superconductors, the Y-Ba-Cu-O system, which we treated as the materials for this research is undoubtedly one of the most important targets for investigating the origin of such properties. Since the discovery of the Y-Ba-Cu-O system, a great deal of research has already been undertaken, and their characterization has also been advanced to a great extent.

Most of these reports have treated nonstoichiometry as one of the main subjects, because the superconductive material in the Y-Ba-Cu-O system has been identified as a nonstoichiometric compound in oxygen by the formula $YBa_2Cu_3O_x$,[7] denoted as 123, where x is the nonstoichiometry of oxygen. This compound has an unusually wide range in high oxygen

nonstoichiometry between x=6 to 7 accompanied by a tetragonal-to-orthorhombic phase change. Twinning occurs along the {1 1 0} planes[8] to alleviate the stress associated with the phase transition. The highly defective structure[9-11] was suggested to be attained by the formation of oxygen vacancies in the O-site which is adjacent to the Cu[1] site on the basal plane, as shown in Fig. 1-1. Furthermore, nonstoichiometry was reported to be a predominant factor for the superconducting transition as well as the phase change and transport properties during the normal state.[12,13]

The characterization of 123 has advanced considerably by using homogeneous ceramics. Due to the variety in the data of the physical properties, which has often been affected by the shape and size of grains, more studies on well-characterized single crystals are needed.

During the early stage of crystal growth, 123 single crystals for X-ray structure analyses were prepared on plates using various sintering methods.[14,15] The single crystals obtained were very tiny, about 0.1 mm in diameter with a thickness of less than 0.05 mm. Large single crystals cannot be grown from a melt having a stoichiometric composition, because a 123 single crystal is an incongruent-melting substance.[16] In other words, it decomposes before melting at high temperatures. Therefore, a growth technique other than the melt growth method has to be employed to synthesize 123 single crystals. In 1987, preparation of larger single crystals were attempted by using a solution of CuO and/or BaO.[17-23] These single crystals were plate-like, about 2 mm in diameter with a thickness up to 0.5 mm, and often displayed a gradual superconductive transition below 90 K. Various attempts have been made to prepare larger and higher quality single crystals. Recently, 123 single crystals with a thickness of up to 2 mm have been obtained by slow cooling of the solution[24-26] using favorable fluxes.

For a more detailed study of the anisotropic properties and a better

understanding of superconductivity, we tried to obtain large, isometric and high quality 123 single crystals. As a result of various attempts, isometric crystals having large aspect ratios, thickness/diameter, with a thickness of about 7 mm were obtained by this experiment. The crystals had well-developed flat surfaces indicating idiomorphic growth.

The temperature dependence of *ab*-plane resistivity ρ_{ab} and the *c*-axis resistivity ρ_c where reported by S. W. Tozer *et al.*[27] (1987) and Y. Iye *et al.*[28] (1988). However, both reports showed different temperature dependences regarding ρ_c. According to the former report, ρ_c showed semiconductor-like temperature dependence. On the contrary, the latter said that there was a metallic behavior in ρ_c. As our single crystals are large enough to measure the anisotropic physical properties, the temperature dependence of resistivities in both the *a* (*b*)- and *c*-directions could be precisely determined.

Measurements on the resistivity changes as a function of the applied magnetic field are important for determining the magnet-electric parameters, such as the upper critical field and the critical current (J_c).[29,30] Until now, 123 single crystals have been not large enough to apply the DC four-probe method along the *c*-axis. Using our single crystals, the resistive transition under the different magnetic fields can be measured by the electric current along or perpendicular to the *c*-axis. The temperature dependence of the magnetic susceptibility was also measured by the superconducting quantum interference device (SQUID) magnetometer when different magnetic fields were applied along or perpendicular to the *c*-axis.

For a fundamental aspect and also for practical applications, a study of the vortex motion is very important. Especially, as regards practical applications, high J_c in a high magnetic field is a problem, which is strongly correlated with flux pinning of the vortex motion. An increase in the current

is associated with various crystalline imperfections such as point defect,[31,32] dislocation,[33] twin boundary,[34-44] grain boundary[45,46] and so on. In the mixed state of type-II superconductors, a supercurrent can flow without resistance in the presence of a high magnetic field below the threshold field, the upper critical field (H_{c2}). Below H_{c2}, as the external field partially penetrates the superconductors, it forms magnetically quantized and elastically flexible flux lines with normal cores. The transport supercurrent interacts with these flux lines and causes a Lorentz force which pushes the flux lines away from the equilibrium position. Driven by this Lorentz force, a phenomenon called a "flux flow" occurs, generating an electric field in the superconductors. In this case, the material shows resistivity as a result of this "flux flow" in the superconductors. In type-II superconductors, various crystal defects inevitably exist and can interact with the flux lines, preventing them from flowing. Flux pinning is usually the term to describe such a flux line-defect interaction. To understand the pinning mechanism and achieve a high J_c, we synthesized 123 single crystals using the various conditions of the coexistence of the solid 211 and the melt phase and focused on the relationship between J_c, and the crystal defects.

The effect of the twin boundaries on J_c has been studied using various techniques: magneto-optical flux visualization,[34,35] Bitter decoration,[36,37] resistivity,[38,39] magnetization[40-42] and torque.[43,44] These experimental studies directly indicated the importance of the twin boundaries for flux pinning. However, there are some difficulties for correct determination because of the relatively small contribution of the twin boundaries to J_c, and because the well-defined twin free 123 single crystals were hard to obtain. The contamination of impurity cations with a different ionic radius and valence from the crucibles during crystal growth has a great influence on the microstrains near the twin boundaries.[46] The detwinning processes in 123

crystals were carried out by applying a uniaxial stress at a temperature up to 600°C,[47-51] However the detwinned crystals were twinned again when oxygen annealing was performed without a uniaxial stress. Therefore, it is difficult to obtain perfectly detwinned crystals which are fully oxidized. When the J_c measurements are carried out in the twinned and detwinned crystals, there is always the possibility of variations in the density of both twin boundaries remained and other defects, such as impurity cations and oxygen vacancies. These defects can mask any contribution to the twin boundaries. We tried to separate the effect of the twin boundaries from that of the other defects in densely twinned and perfectly detwinned domains in the same 123 single crystal by using the data from the magnetic studies. The thermomechanical detwinning of 123 crystals was made under inert atmoshere to obtain a perfect detwinned domain. The contribution of the twin boundaries to J_c was studied using various temperatures and magnetic fields.

The construction of the present paper is as follows. In the next chapter (Chapter 2), crystal growth of large isometric 123 single crystals and determination of their anisotropic properties are described. In Chapter 3, crystal growth mechanism of 123 single crystals through the peritectic reaction is investigated and Ostwald ripening mechanism under coexisting region of solid with melt is discussed. In Chapter 4, relationship between growth condition and flux pinning in 123 single crystals is focused. In Chapter 5, effect of twin boundaries on flux pinning in densely twinned and perfectly detwinned 123 single crystals is mentioned. Finally, the paper is summarized with the concluding remarks in Chapter 6.

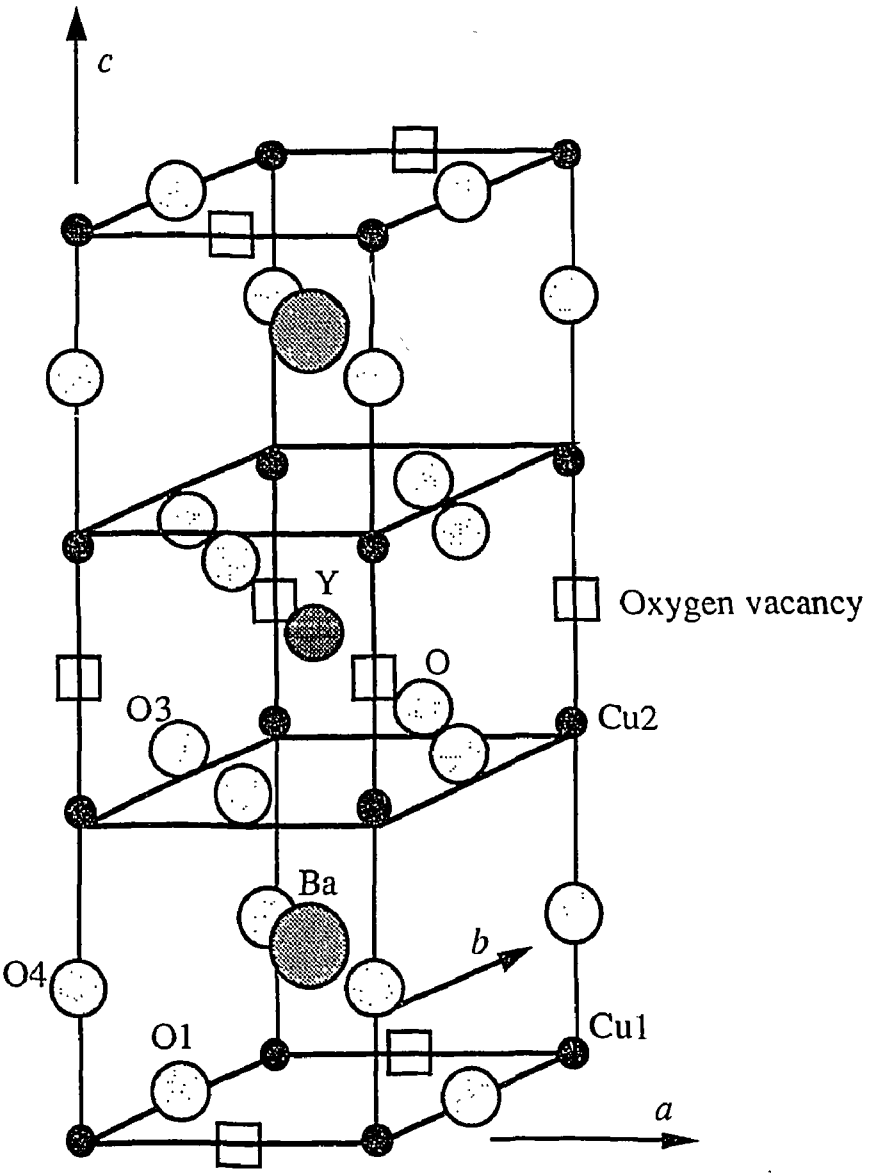

Fig. 1-1. Crystal structure of orthorhombic $YBa_2Cu_3O_x$.[7-9]

Chapter 2. Growth of Large Isometric $YBa_2Cu_3O_x$ Single Crystals from a Coexisting Region of a Solid with a Melt

2.1 Introduction

The synthesis of large, isometric and high-quality single crystals of $YBa_2Cu_3O_x$ (123) will make an essential contribution in an effort to understand the mechanism of high-temperature superconductors. In this chapter, we have described the method for preparation of large single crystals and their characterization. There are many critical problems for the growth of 123 single crystals. The phase diagram in the ternary system Y_2O_3-BaO-CuO reported by Dembinski *et al.*[52] indicates that the composition of 123 exists outside the primary crystallization field, as shown in Fig. 2-1. This indicates that 123 melts are incongruent and require a solution growth technique for obtaining single crystals. The commonly used solvent is an excess of CuO and/or BaO.[17-26] Other solvents, however, provide unacceptable results as a regards crystal size and quality. The other main solvents already reported[52-60] are summarized in Table 2-1. Further difficulties exist in the preparation of large single crystals, even when $BaCuO_2$-CuO was used as a solvent, because the primary crystallization field of 123, bounded by the one peritectic line and the two eutectic lines, is very narrow in composition and also as regards temperature. All compounds except for 123 easily solidify in such a narrow composition range, and consequently, the growth of large 123 single crystals can not occur.

In addition to the restriction of choosing the adequate solvents, the growth process is hampered by the pronounced reactivity of the melt with most crucible materials, which tends to contaminate the growth of 123 crystals. Thus, the choice of crucible materials is very limited.

The separation of crystals from the residual solution is another important problem. Since 123 crystals have almost the same chemical reactivity with extraction reagents as with solvent materials, no regent has been found which will enable chemical separation of 123 crystals from a solvent.

In the present experiments, various attempts have been made to overcome these problems. The concentration of 123 in a solution was systematically varied to determine the most suitable composition for growth. We also checked the contamination of a melt from crucible materials. Many types of separation techniques of 123 crystals from the residual solution were also tested. Eventually, we succeeded in obtaining thick, large and high-quality 123 single crystals with developed habits.

2.2 Experimental

2.2.1 Choice of solvent

Various self-flux systems of Y_2O_3-BaO-CuO were tested, and finally, the flux composition $7BaCuO_2$-11CuO, which shows the lowest eutectic point of 915°C, was adopted. The six main compositions used in the pseudo-binary system are indicated by arrows in Fig. 2-2.

Typical growth conditions were determined as follows: powders of Y_2O_3 (99.99%), $BaCO_3$ (99.99%) and CuO (99.99%) were mixed in an agate mortar with acetone added to facilitate mixing. After the powders were dried, the mixture, packed into an aluminum crucible, was heated to 1050°C in a furnace and soaked for 24 h in air. Then, the temperature was lowered at a rate of 0.5°C/h. In several runs, the separation of crystal grains from the remaining solution was performed at 970°C as described in detail in a later section. The separated crystal grains were then cooled

slowly to room temperature.

2.2.2 Crystal growth

After determination of the optimum composition of the solvent, as well as the concentration of the nutrient, preparation of 123 single crystals was carried out. To minimize the soaking time for reducing possible crucible corrosion, starting materials were presynthesized 123 powders and preheated $BaCuO_2$-CuO mixtures, which were prepared from powders of Y_2O_3, $BaCO_3$ and CuO with a 99.99% purity. The mixtures were placed in yttrium crucibles or, in some cases, aluminum crucibles. The typical procedure consisted of heating the furnace from room temperature to 1050°C, and soaking at this temperature for 24-72 h in air. According to the phase diagram of Dembinski *et al.*,[52] compositions No.1 to 5 in Fig. 2-2 lie in a two-phase region of Y_2BaCuO_5 (211) and liquid during the soaking period. The mixture was cooled at a rate ranging from 1-0.5°C/h and when the mixture reached a temperature between 1010 and 980°C, below the peritectic line, three phases, 123, 211 and liquid appeared with the assumed peritectic reaction of the solid and the liquid phase. The temperature was maintained in this range long enough for the reaction to progress, and at 970°C, the crystal grains were separated from the remaining solution. The residual crystals in the crucible were cooled to room temperature at a rate of about 50°C/h.

It should be noted that large crystals were grown in the Y_2O_3 crucibles, whereas much smaller crystals were obtained in the Al_2O_3 crucibles, especially in the regions near the crucible walls. The result suggests that Al_2O_3 has a tendency to dissolve into the self-flux systems and to obstruct the growth of 123 crystals.

2.2.3 Control of spontaneous nucleation

Most of the crystals obtained were rather small in size, since multinucleation was assumed to have occurred. To prevent spontaneous nucleation, we controlled the temperature gradient in the crucibles and experimented with the addition of seed crystals. Figure 2-3 shows a typical temperature gradient in the 100 ml crucible heated in a muffle furnace. The temperature gradient was induced by cooling the crucible wall, where the temperature of the right side was lower by 7-10°C than that of the left. The gradient was controlled by changing the diameter of the hole bored into the right side of the furnace wall by about 10 mm^2.

Seeding was performed to reduce spontaneous nucleation which might be enhanced by the roughness of the crucible wall. The procedure was as follows: the mixture in the Y_2O_3 crucible was heated from room temperature to 1050°C in air and was soaked for 24 to 72 h. Seed crystals, which were preheated in the furnace, were quickly placed into the crucible, and the mixture was rapidly cooled to 990°C to prevent dissolution of the seeds. The mixture was held for 5 to 10 days, and then, the temperature was lowered at a rate of 0.5°C/h. At 970°C, the remaining solution was separated.

2.2.4 Separation of crystals from solution

Three methods of separation were tested. In the first method, the residual solution was drained through holes bored in the bottom of the crucible (Fig. 2-4(a)). Various sizes and numbers of holes were used. In the second method, a porous ceramic bar was dipped into the crucible to absorb the residual solution, and then withdrawn, (Fig. 2-4(b)), as reported by Boutellier *et al.*[61] These techniques were found to be not very convenient for crystal-

solution separation because a considerable amount of residual solution still remained in the crucible.

In the third method, the hot crucible was quickly removed from the furnace and the grown crystals were separated from the residual solution by decanting as shown in Fig. 2-4(c). This is the simplest and most successful method for separation. This method, however, resulted in a large thermal shock to the crystals, and the as-grown crystals tended to crack, especially when the crystal size was large as shown in Fig. 2-5. Therefore, the decantation method was improved by inclining the crucible in the heating furnace, and then by reducing the temperature of the furnace very slowly. As a consequence, the number of cracks could be reduced.

2.2.5 Oxygen nonstoichiometry

Oxygen annealing was performed at a temperature between 450 and 600°C for 0.3 to 7 days under various oxygen pressures so as to increase the oxygen content in the as-grown crystals. The content of oxygen was determined by an iodometric titration under argon atmoshere. The unit cell parameter was determined by the X-ray powder diffraction (XPD) method using Cu Kα radiation with a graphite monochromator.

2.2.6 Anisotropic properties

The oxygen-annealed single crystals, which were large enough to allow measurement of the resistivity along the *a* (*b*)- and *c*-axes, were adopted for use with the Montgomery method which is one of DC four-probe techniques. The resistivity change was measured as a function of the applied external field (***H***) by flowing a current along or perpendicular to the *c*-axis.

The temperature (T) dependence of the magnetic susceptibility (χ) was also measured by a SQUID magnetometer at H of 0.3 or 1 T along or perpendicular to the c-axis. The shielding effect was measured as follows: the specimen was cooled down to 4 K in a zero field, then, H of 3.5 x 10^{-4} T was applied and the χ-T relation was measured as the temperature increased.

2.3 Results and discussion

2.3.1 Crystal growth

We succeeded in synthesizing large 123 single crystals under the conditions where the solid 211 phase and liquid phase coexisted. The composition most conducive to producing large crystal was No.4 in Fig.2-2, in which the ratio of 1/6 (123) to 1/25 ($7BaCuO_2 \cdot 11CuO$) equaled 3:7. The established phase diagrams[52] support the assumption that the growth of crystals progressed with an aid of the peritectic reaction between 211 and the surrounding liquid phase,[62] as indicated in the following equation.

$$Y_2BaCuO_5\ (\text{solid}) + 3BaO\ (\text{liquid}) + 5CuO\ (\text{liquid}) + (x\text{-}6.5)O_2 \rightleftharpoons 2YBa_2Cu_3O_x\ (\text{solid}) \qquad (2.1)$$

The results of analysis performed by using electron probe microanalyzers (EPMA) show that the residual materials remaining on the crystal surfaces contain only a small amount of Y, and that an actual 211 phase did not exist in the 123 single crystals when the mixture was held at temperatures between 1010 and 980°C for a sufficient period of time. This result is an evidence for the completeness of the reaction during the 123 growth.

In the present experiment, we determined conditions of the temperature gradient in the crucible which prevented spontaneous nucleation (Fig. 2-3). The gradients higher than those indicated in Fig. 2-3 resulted in the production

of smaller crystals. On the other hand, the lower gradients were not effective for suppressing multinucleation. The largest single crystals, existing at the corner of the crucible bottom, had shiny flat surfaces with maximum dimensions of 4.3 x 4.3 x 3.6 mm^3 which correspond to orthorhombic *a* (or *b*) x *b* (or *a*) x *c* axes (Fig. 2-6).

In the next stage, we attempted to prepare large crystals using seed crystals, and found that the growth was facilitated by the use of the seed which was carefully cast in a solution at an optimum temperature after soaking. Because of the opaque properties of the high-temperature solutions, the identification whether crystal growth or dissolution occurred was difficult directly with the naked eyes. Thus, experiments were carried out using a trial-and-error method technique to determine the soaking, seeding and decanting temperatures. They were carefully conducted in this study in the same manner as those already described in Section 2.2.3. As a result of these attempts, the largest single crystal was found to exist at the center of the crystal cluster. Figure 2-7 shows the as-grown crystal with well-developed habits and a maximum thickness of about 7 mm along the *c*-axis.

Typical polyhedral crystals have shiny flat surfaces of {1 0 0} and {0 0 1}, and some single crystals are surrounded by {1 0 0}, {0 0 1} and {0 9 10} surfaces as shown in Fig. 2-8. Until now, most of the prepared 123 single crystals[19-23] have had a small aspect ratio. As shown in Fig. 2-9, single crystals having aspect ratios larger than unity are often present among the crystals. Similar thick crystals along the *c*-axis have been obtained by Sadowski and Sheel,[24] Wolf *et al.*[25] and Schonmann *et al.*[26] The platelet shape of 123 single crystals suggests rapid growth or dendritic growth toward the *a*- or *b*-axis due to supercooling with no indication of their "stratified" structure.

In addition to these studies, we also investigated the usefulness of the

following solvents for growing large 123 crystals. The solvent compositions were $7BaCuO_2 \cdot 11CuO$ including 5 mol% of NaF, NaCl, KF, KCl, BaF_2, B_2O_3, V_2O_5, PbO, Bi_2O_3, NaOH and KOH. However, none of these solvents could obtained successful results.

2.3.2 Characterization

The compositional distribution of the constituent metal atoms on the cross section along the *c*-axis was determined by EPMA. The data supports the finding that the crystals are very homogeneous in Y, Ba and Cu along the *c*-axis as shown in Fig. 2-10. After determination of the oxygen content in the crystals, we found that the as-grown crystals were not fully oxidized and application of more than 1 atm of oxygen pressure was necessary to increase the oxygen content to the stoichiometric level. Table 2-2 lists the annealing conditions and the results which are described as a change in the unit cell parameters or oxygen contents.

The as-grown single crystals showed high resistivity, whereas the annealed single crystals showed low resistivity with a sharp superconductive transition at 91 K as seen in Fig. 2-11. It became clear that oxygen annealing resulted in both an increase in the superconducting onset temperature and a sharp transition. The temperature dependence of the resistivity was found to be metallic in the *a* (*b*)- and *c*-directions. This behavior agrees with the results reported by Iye *et al.*[28] and Ito *et al.*,[65] but is different from those of Tozer *et al.*,[27] and those on $La_{2-x}Sr_xCuO_4$[64,65] or on $Bi_2Sr_2CaCu_2O_x$,[66] where the values of ρ_{ab} were metallic but those of ρ_c were semiconductive near T_c. Ito *et al.*[63] has discussed the origin of the metallic conduction along the *c*-axis in 123 and suggested that such a behavior was attributable to the exceptional crystal structure of the oxide superconductors, where -Cu-O-

Cu-O- sequences were realized along the *c*-axis.

To certify the uniform distribution of oxygen in annealed crystals, two types of experiments were conducted. In the first experiment, a crystal was gradually polished parallel to the *c*-plane, and the ρ_{ab}-T relationships were subsequently measured on the polished surfaces. No apparent change was observed in the ρ_{ab}-T curves between the as-annealed and polished planes. In the second experiment, an annealed crystal was cut perpendicular to the *ab*- and *c*-planes into nine pieces of equal size. The temperature dependence of χ was measured for each piece, and sharp transitions at 91 K with the same diamagnetic contributions were found in all specimens. These findings lead to the conclusion that O_2-annealed crystals are homogeneous as regards oxygen content.

The temperature dependence of χ of the annealed 123 crystals showed a weak paramagnetism in the normal state, as shown in Fig. 2-12. For both directions of the applied field, parallel and perpendicular to the *c*-axis, apparent diamagnetism was observed just below T_c, which confirmed the occurrence of the superconductivity. The saturation values of the diamagnetic susceptibility at low temperature were evaluated to be about 190% of the perfect diamagnetism for $\boldsymbol{H}$ applied along the *c*-axis (i.e., perpendicular to the CuO_2 plane), and about 130% for $\boldsymbol{H}$ applied perpendicular to the *c*-axis. These excessively high values in χ are attributed to the demagnetization effect of the specimen, i.e., the actual field which existed around the sample is much larger than the applied field. The difference in the demagnetization effect for each field direction is consistent with the shape of the sample examined; the crystal is slightly flattened over the *ab*-plane.

As shown in Fig. 2-12, both the sharpness of the magnetic transition at T_c and a value of the diamagnetic susceptibility between 4 and 80 K, guarantee the high quality of the single crystals,[67,68] indicating a homogeneity

as regards oxygen content.

The $\boldsymbol{H}$ applied parallel to the c-axis, *i.e.*, perpendicular to the CuO_2 plane, caused a remarkable broadening of the resistive transition, whereas the effect of the magnetic field for the transition was smaller when $\boldsymbol{H}$ was applied perpendicular to the c-axis, as shown in Figs. 2-13 and 2-14. This result has a close resemblance to those obtained in $La_{2-x}Sr_xCuO_4$ single crystals[65,69]: the transition widths depend not on the current direction, but on the direction of $\boldsymbol{H}$ relative to the c-axis. If the resistivity is measured by flowing the current along the c-axis and perpendicular to it, the Lorentz force exerted on the fluxoid lines by the current should be zero and maximum, respectively. These facts lead to the conclusion that the Lorentz force is not always an origin of the broadening mechanism of the transition region under the magnetic field. Therefore, this phenomenon should be interpreted in terms of the rather direct effect of the magnetic field on some anisotropic factor.

As shown in Fig. 2-15(a), the slope of the χ-T curve for $\boldsymbol{H}$=0.3 T applied along the c-axis, decreases as the temperature approaches 4 K. This indicates that the lower critical field (H_{C1}) approaches $\boldsymbol{H}$=0.3 T in this temperature range. On the other hand, no decrease is found in the slope of the curve for $\boldsymbol{H}$ applied perpendicular to the c-axis, as shown in Fig. 2-15 (b). These observations lead to the following conclusion that H_{C1} of 123 for $\boldsymbol{H}$ applied along the c-axis, is much larger than that for $\boldsymbol{H}$ applied perpendicular to the c-axis. The first deviations of the χ-T curves from nearly zero susceptibility above T_c occur at the applied $\boldsymbol{H}$, becoming the H_{C2} of these temperatures, in Figs. 2-16(a) and 2-16(b). These H_{C2} values agree well with those obtained from the ρ-T curves in Figs. 2-13 and 2-14.

2.4 Summary

Large isometric single crystals of oxide superconductor 123 have been successfully grown from a mixed region of the solid 211 and the melt phase. The crystals had sharp, shiny habits with a maximum thickness of about 7 mm along the *c*-axis. The best growth conditions were determined for obtaining large single crystals, where the solvent composition was $7BaCuO_2$-11CuO which is close to the binary eutectic of $BaCuO_2$-CuO, and the optimum concentration of the growth system was in the ratio of 1/6 (123) to 1/25 ($7BaCuO_2$•11CuO) of 3:7. The use of the Y_2O_3-crucible which is expected to be free from the contamination of impure metals from containers due to heating was found to result in the production of crystals of the highest purity. Both the introduction of the temperature gradients and the use of seed crystals were essential for controlling nucleation.

The oxygen-annealed crystals showed a sharp superconductive transition at 91 K. The temperature dependence of the resistivities was found to be metallic both in the *a* (*b*)- and *c*-direction, and was very different from those of other oxide superconductors such as $La_{2-x}Sr_xCuO_4$ and $Bi_2Sr_2CaCu_2O_x$. Sufficient shielding was observed both in the sharpness of the transition at T_c and in the required value of the diamagnetism at low temperatures below T_c.

The marked anisotropy is observed in the transition region in the resistivity (ρ)-temperature (T) curve under the applied magnetic field parallel or perpendicular to the *c*-axis. It becomes clear that the transition width depends not on the direction of the transport current but on the direction of the applied magnetic field. A remarkable broadening of the resistive transition is observed when the magnetic field is applied perpendicular to the CuO_2 plane. These phenomena should be interpreted in terms of some anisotropic

factor without any Lorentz force, as those obtained in $La_{2-x}Sr_xCuO_4$ single crystals.

The anisotropic behavior in the susceptibility (χ)-temperature (T) curve is also apparent between the applied magnetic field parallel and perpendicular to the c-axis; a large diamagnetism is observed when the magnetic field is applied along the c-axis and vice versa. This large value is attributed to the complete demagnetization of the specimen, *i.e.*, the actual field seen by the sample is much larger than the external magnetic field. Comparison of the anisotropic temperature dependence of the upper critical field which is observed in the ρ-T and χ-T curves, shows excellent agreement. The slope of the χ-T curve for H=0.3 T applied along the c-axis decreases as the temperature approaches 4 K. This indicates that the lower critical field (H_{c1}) approaches H=0.3 T in this temperature range. On the other hand, no such decrease is found in the slope of the curve for H applied perpendicular to the c-axis. These can be reasonably explained in terms of anisotropy in penetration of the magnetic field to the superconductive 123 crystals.

Table 2.1. Reported solvents other than BaO-CuO for the growth of $YBa_2Cu_3O_x$ and prepared crystal size

<Successful solvents>

Solvent	Crystal size (mm) *a* (or *b*) x *b* (or *a*) x *c*
$PbO-B_2O_3$	2x2x0.03
B_2O_3	2 x 1.5 x 0.1
In_2O_3	2-5 x 2-5 x 0.2-0.5
BaF_2	2 x 2 x 0.3
K_2CO_3	3 x 3 x 1.5
NaCl-KCl	5 x 4 x 3

<Unsuccessful solvents>

Li_2CO_3, Na_2CO_3, K_2CO_3, K_2CO_3-$K_2B_4O_7$, $K_2B_4O_7$, KOH, KCl, KCl-B_2O_3, KCl-$K_2B_4O_7$, BaB_2O_4, BaO_2, BaF_2, BaF_2-KF, $BaCl_2$, $BaCl_2$-BaO, KF, KF-NaF-$K_2B_4O_7$, KF-B_2O_3, KF-B_2O_3-TiO, KF-BaO, KF-BaO-B_2O_3, PbO_2, PbO, PbO-PbF_2, Bi_2O_3, MoO_3, Li_2MoO_4, PbO-PbF

Table 2.2. Oxygen-annealing effect on the oxygen concentration and the unit cell parameters of $YBa_2Cu_3O_x$ single crystals

Partial pressure of O_2 (atm)	Temperature (°C)	Annealing duration (days)	Oxygen content (x)	Unit cell parameters a_0 (nm)	b_0 (nm)	c_0 (nm)
0.2 (As-grown)	——	——	6.76	0.3825	0.3888	1.1711
1	550	7	6.87	0.3820	0.3892	1.1689
5	550	7	7.00	0.3819	0.3890	1.1680
350	600	0.3	7.02	0.3818	0.3887	1.1690

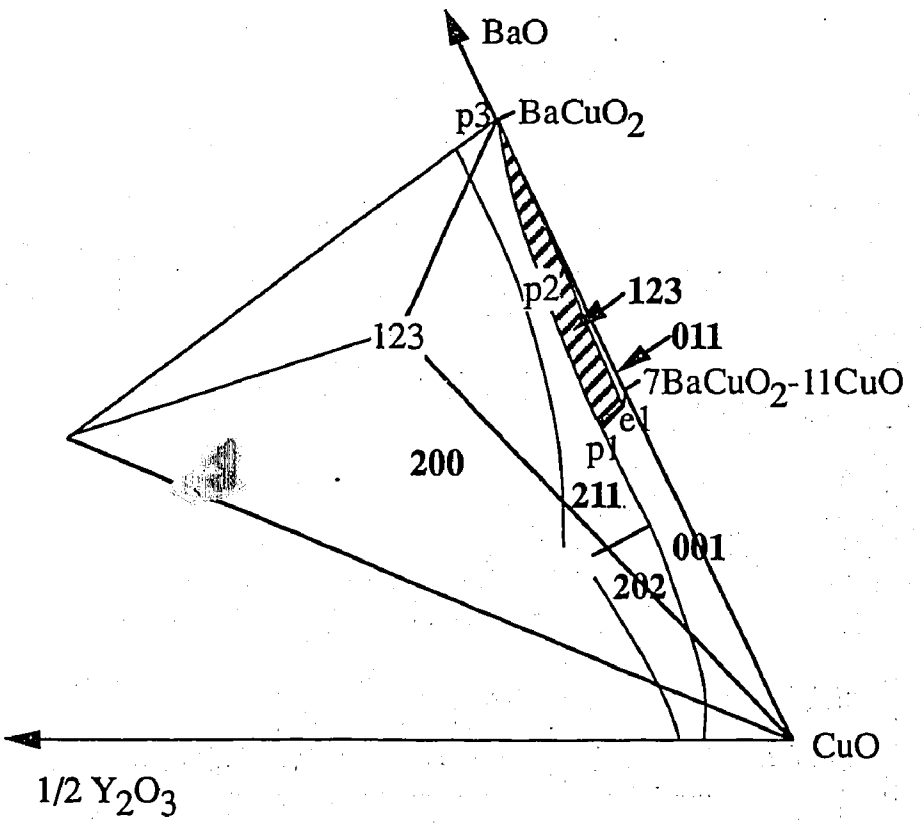

e1 915°C 123+011+001 ⇄ L　　p1 940°C 123+001 ⇄ 211+L

p2 1010°C 123 ⇄ 211+L　　p3 1000°C 011+123 ⇄ 211+L

Fig. 2-1. A phase diagram[52] in the pseudo-ternary system 1/2 Y_2O_3-BaO-CuO. The shaded portion is the primary crystallization field of 123 which is bounded by the peritectic line p1-p2-p3 and two eutectic lines p1-e1 and p3-e1. The bold characters show primary crystallized materials. The phases are labeled as follows: 123: $YBa_2Cu_3O_x$, 011: $BaCuO_2$, 001: CuO, 211: Y_2BaCuO_5, 200: Y_2O_3, 202: $Y_2Cu_2O_5$

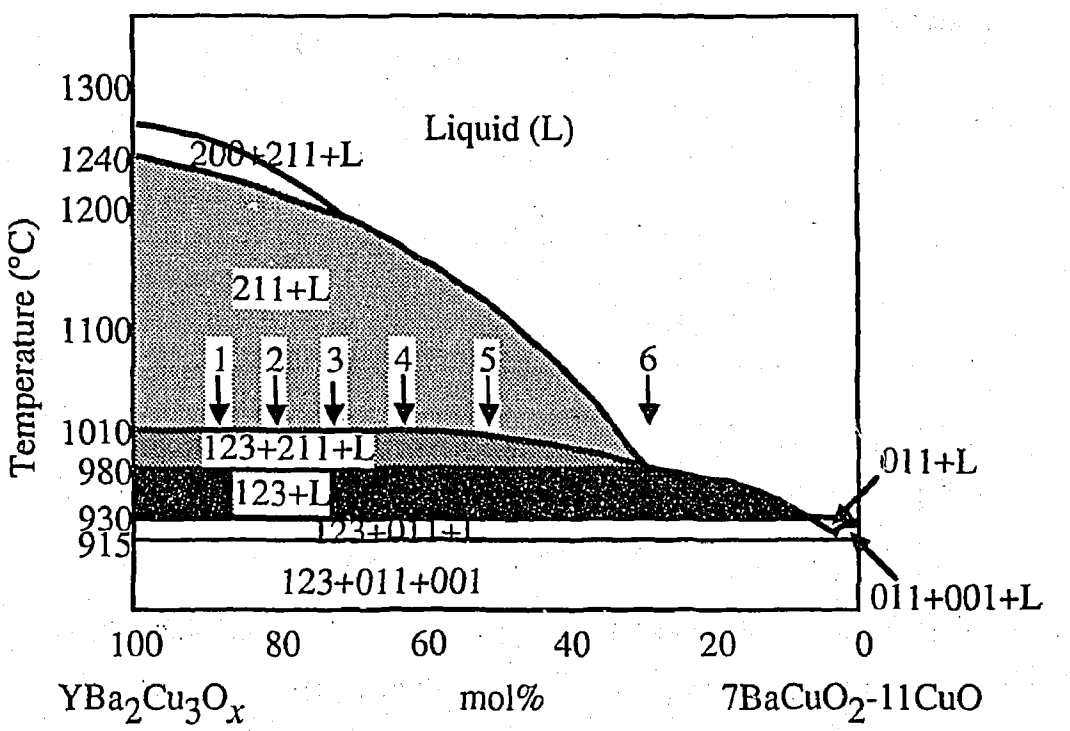

Fig. 2-2. A pseudo-binary phase diagram of $YBa_2Cu_3O_x$ being joined to $7BaCuO_2 \cdot 11CuO$.[52] The arrows show the selected compositions for preparation of $YBa_2Cu_3O_x$ single crystals in the present experiment. The phases are labeled as follows: 123: $YBa_2Cu_3O_x$, 011: $BaCuO_2$, 001: CuO, 211: Y_2BaCuO_5, 200: Y_2O_3

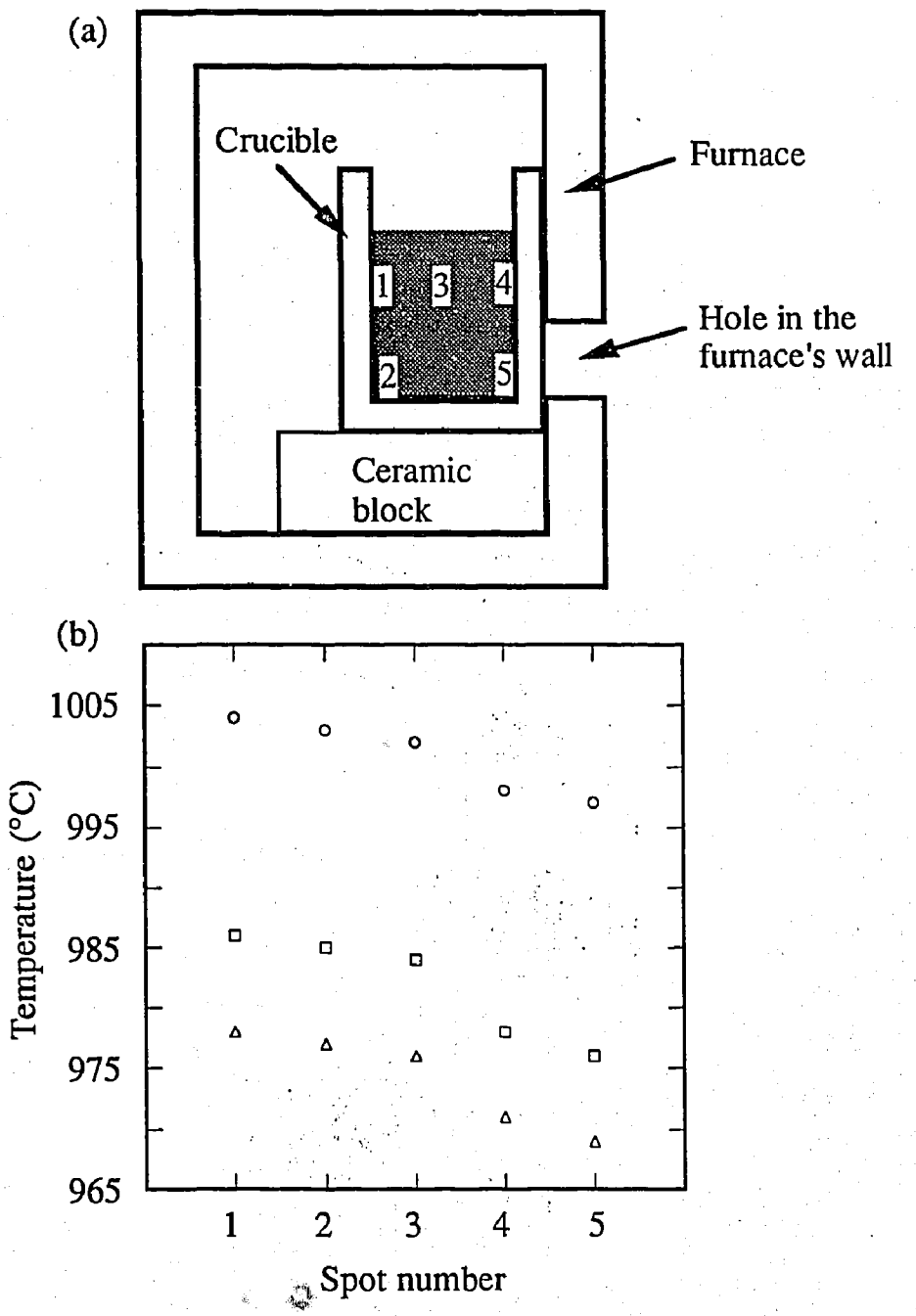

Fig. 2-3. (a) Correspondence of the spot number to the position for a temperature measurement in the crucible. (b) Optimum temperature gradient in the crucible under various soaking temperatures for crystal growth.

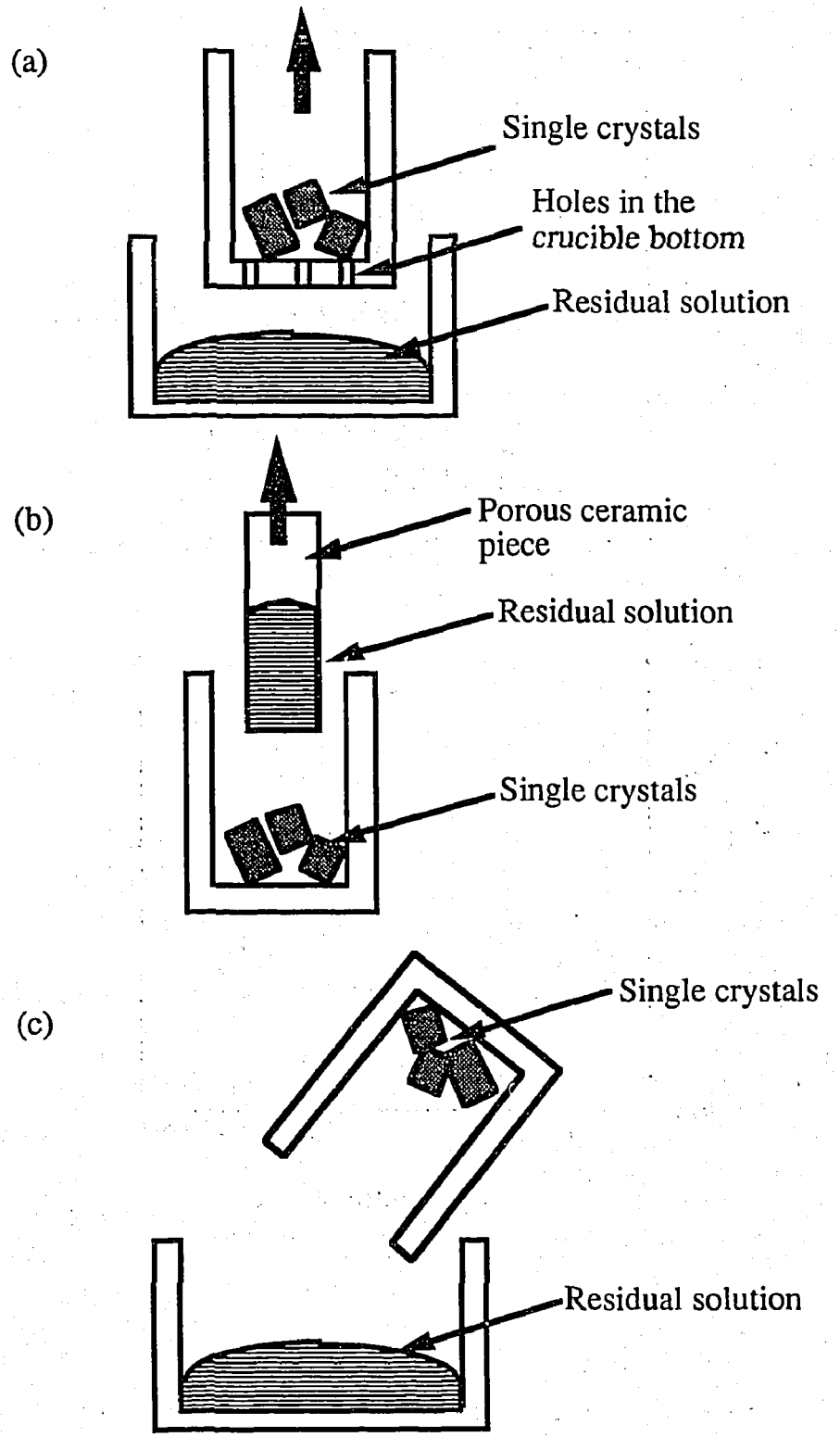

Fig. 2-4. Three methods for separation of grown crystals from a residual solution.

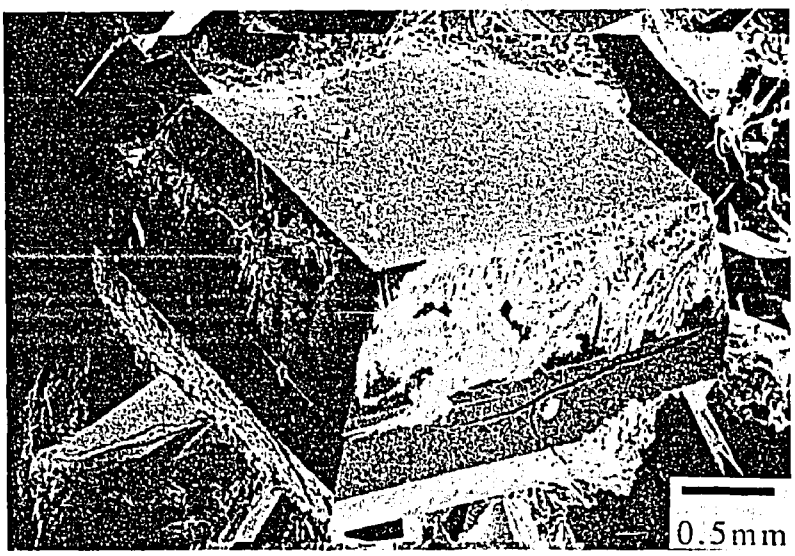

Fig. 2-5. A SEM photograph of $YBa_2Cu_3O_x$ single crystals showing thermal cracks.

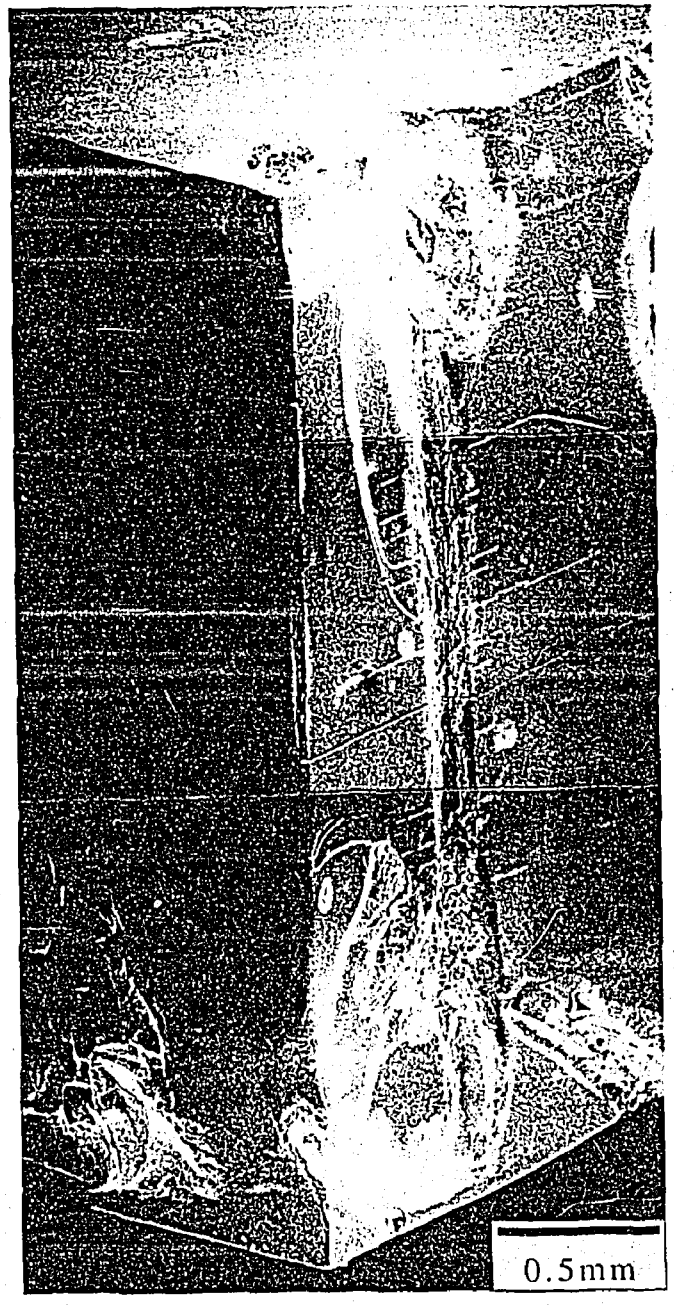

Fig. 2-6. A SEM photograph of a large isometric $YBa_2Cu_3O_x$ single crystal which has a thickness of 3.6 mm along the *c*-axis. The longitudinal direction is along the *c*-axis.

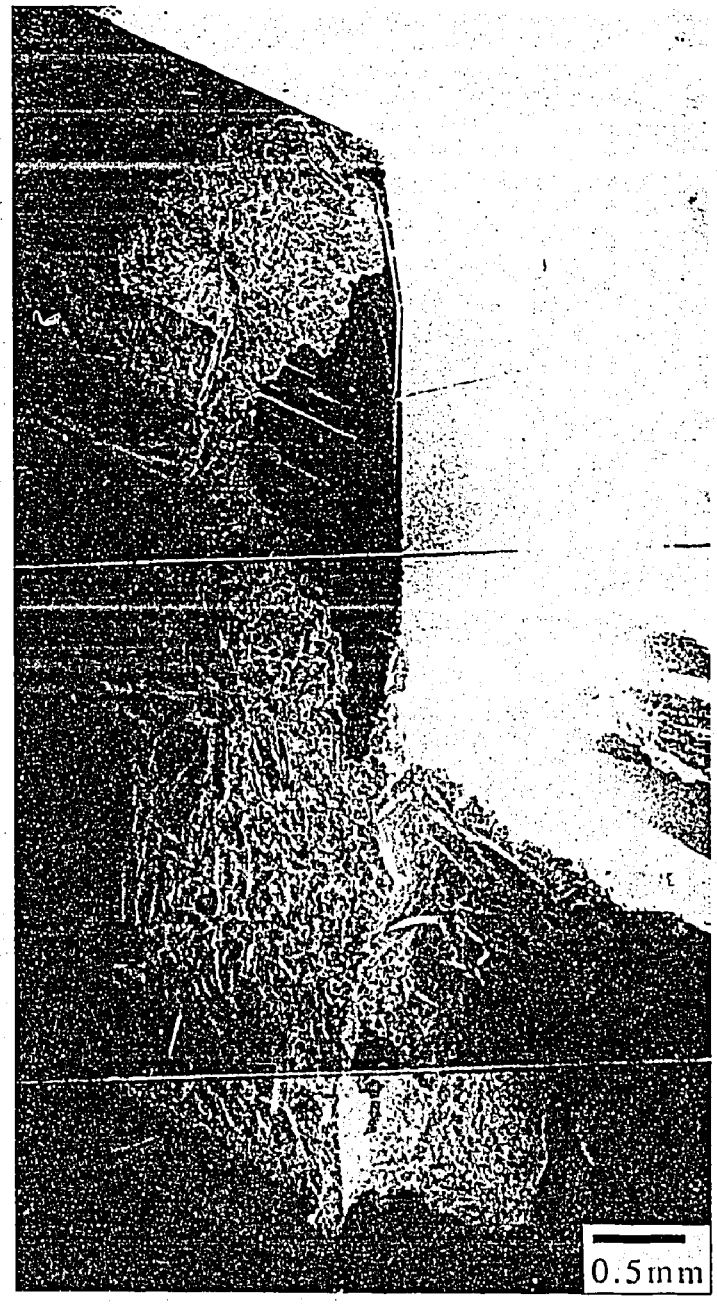

Fig. 2-7. A SEM photograph of a large isometric $YBa_2Cu_3O_x$ single crystal which has a thickness of 6.4 mm along the *c*-axis. The longitudinal direction is along the *c*-axis.

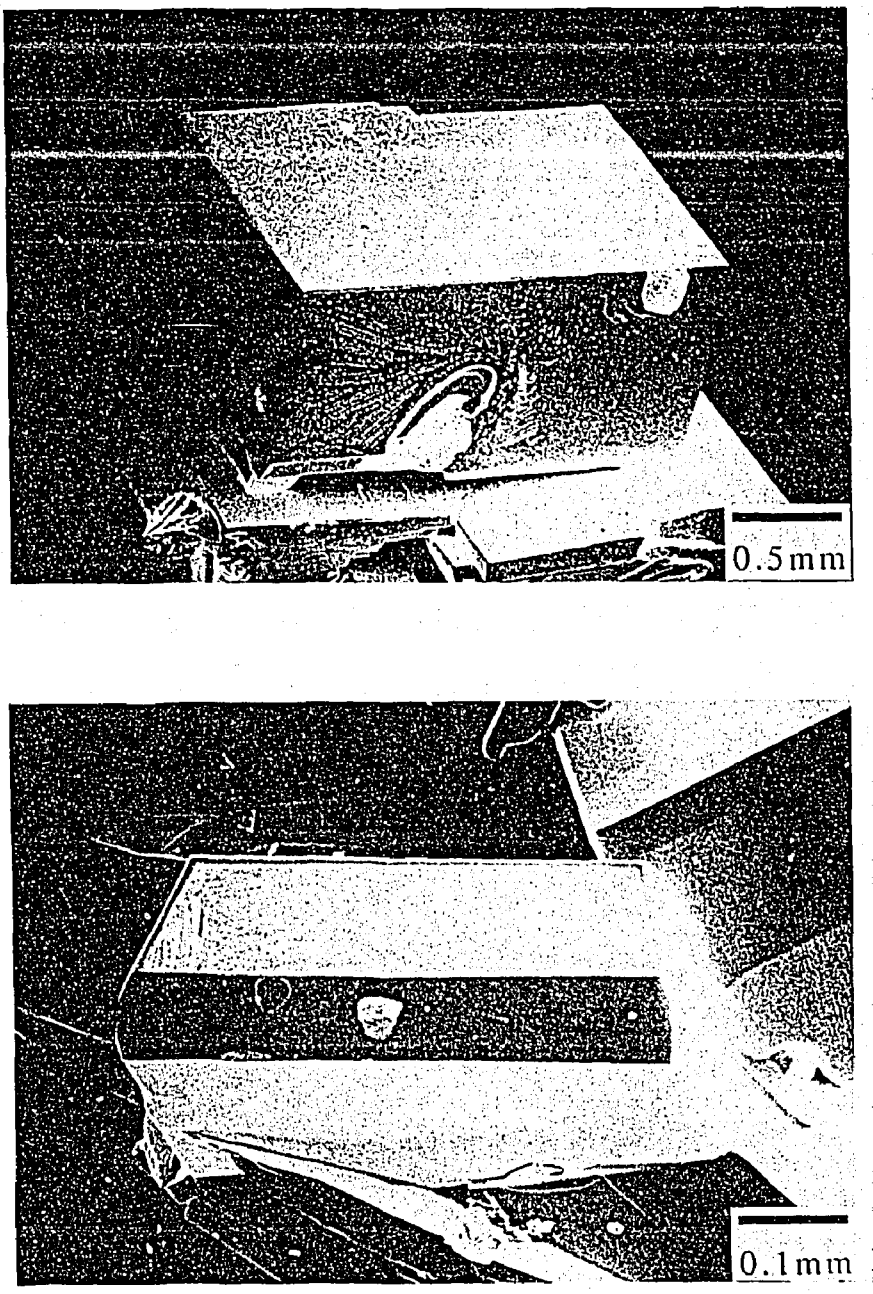

Fig. 2-8. SEM photographs of typical polyhedral $YBa_2Cu_3O_x$ single crystals. The longitudinal direction is along the *c*-axis.

Fig. 2-9. A SEM photograph of $YBa_2Cu_3O_x$ single crystal which has an aspect ratio much larger than unity. The longitudinal direction is along the *c*-axis.

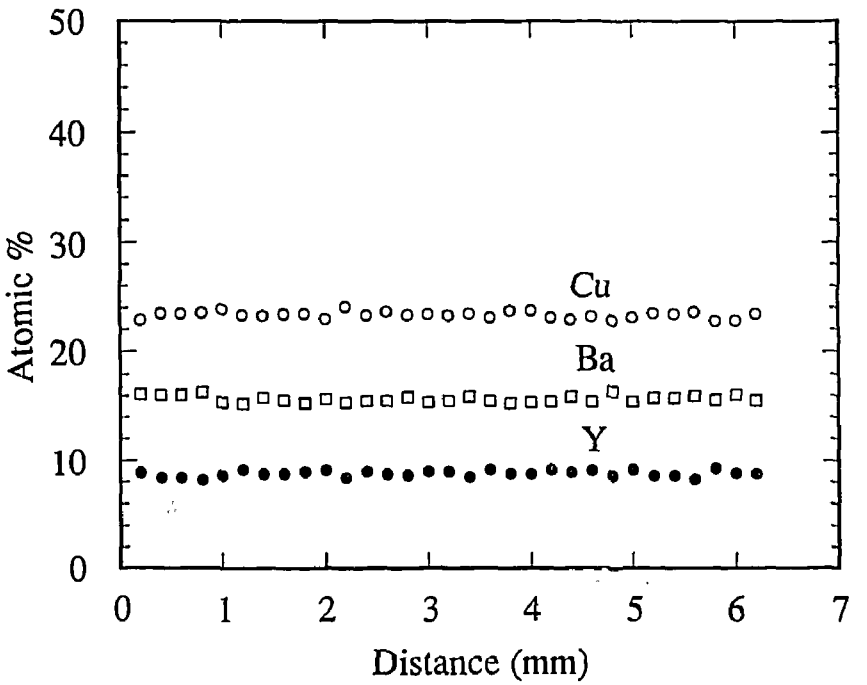

Fig. 2-10. Compositional distribution of Y, Ba and Cu atoms in the cross section along the *c*-axis. The data were determined using EPMA.

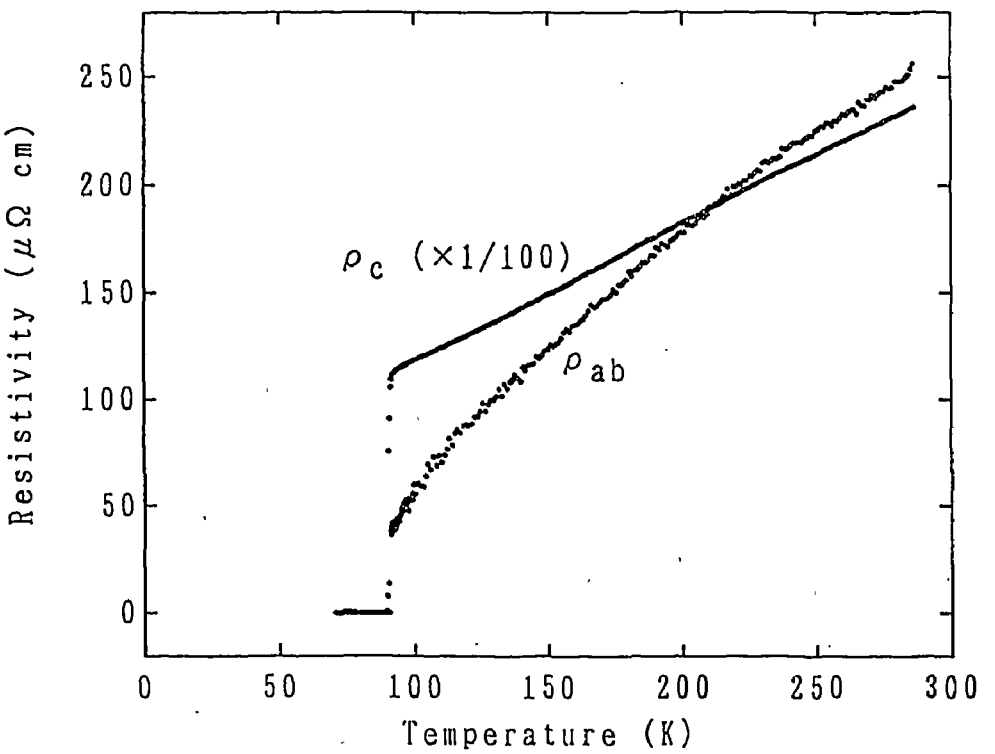

Fig. 2-11. Temperature dependence of the resistivity of an O_2-annealed $YBa_2Cu_3O_x$ single crystal. The resistivity is measured from the current flowing along or perpendicular to the *c*-axis.

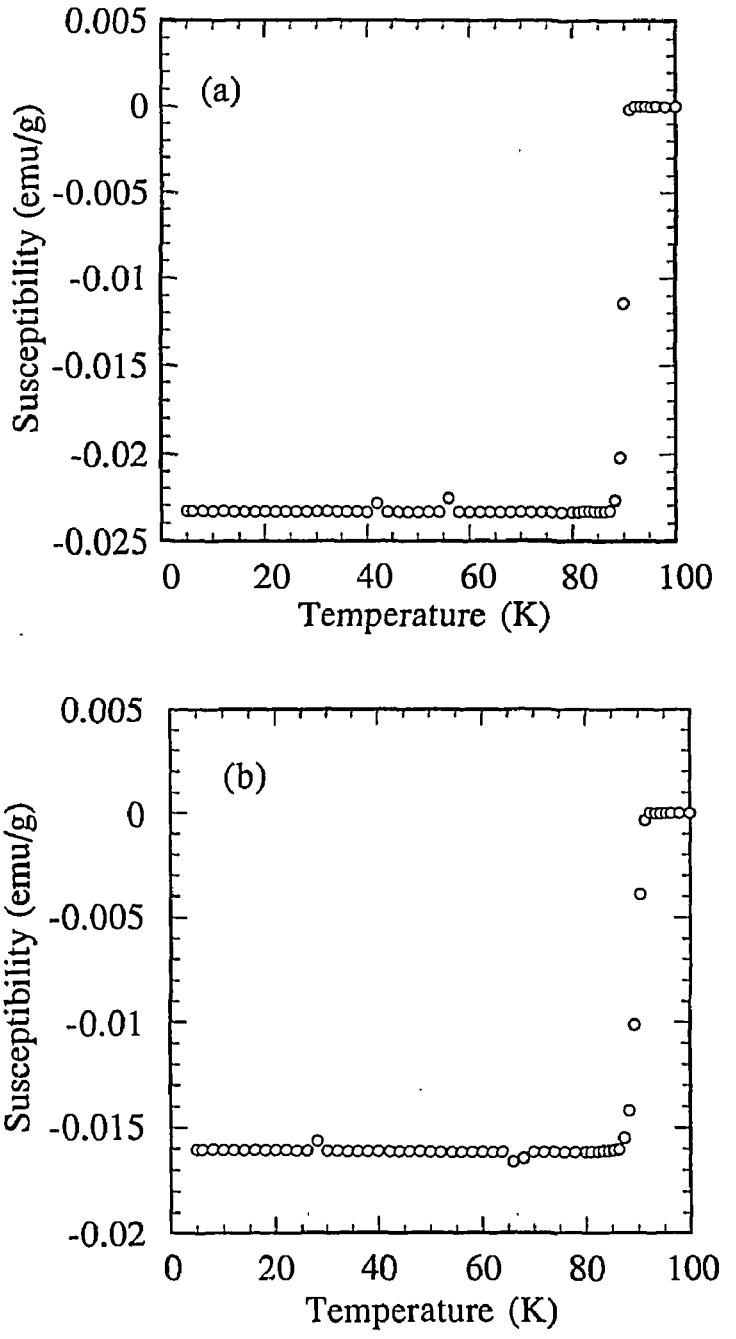

Fig. 2-12. Temperature dependence of the magnetic susceptibility of an O_2-annealed $YBa_2Cu_3O_x$ single crystal. The magnetic field of 3.5×10^{-4} T was applied along or perpendicular to the *c*-axis in (a) and (b), respectively.

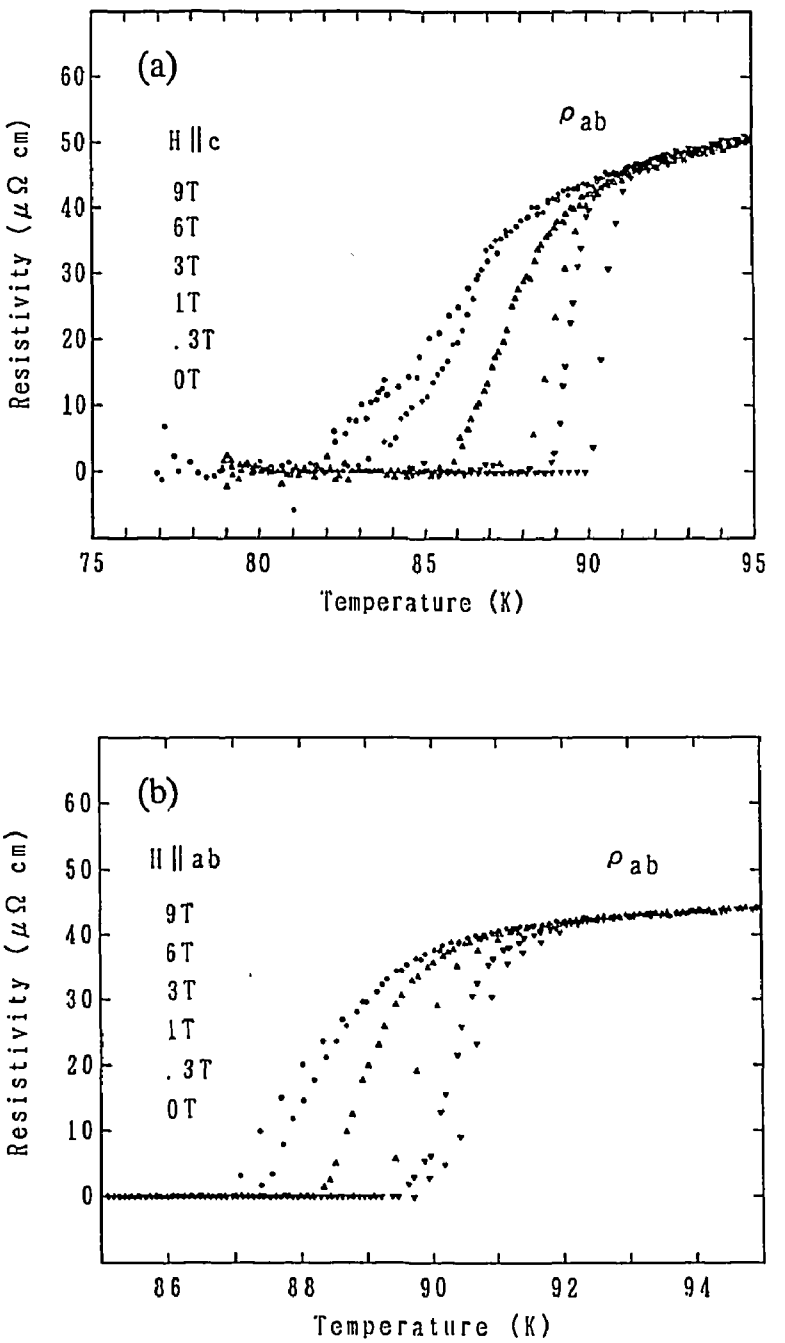

Fig. 2-13. Resistive transition of an O_2-annealed $YBa_2Cu_3O_x$ single crystal under magnetic fields up to 9 T which are applied along or perpendicular to the *c*-axis in (a) and (b), respectively. The resistivity is measured by flowing current perpendicular to the *c*-axis.

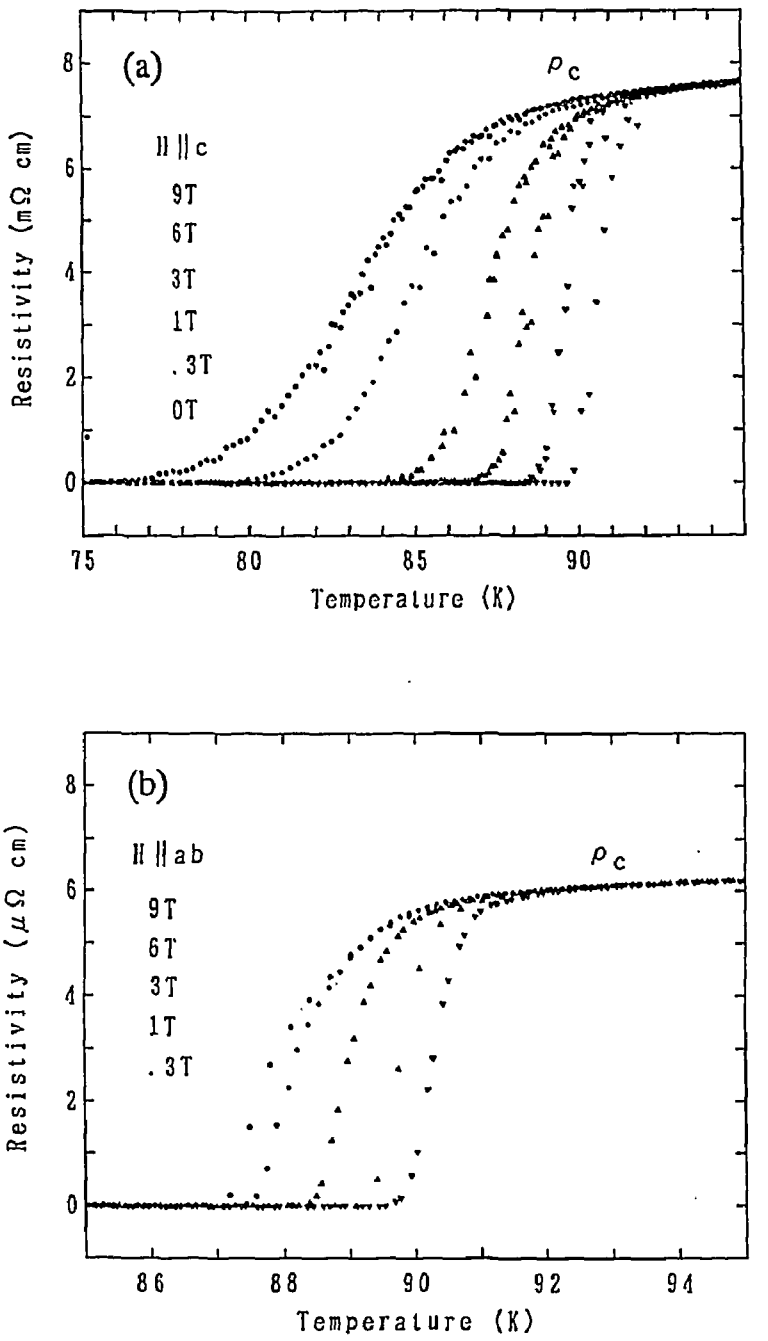

Fig. 2-14. Resistive transition of an O_2-annealed $YBa_2Cu_3O_x$ single crystal under magnetic fields up to 9 T which are applied along or perpendicular to the *c*-axis in (a) and (b), respectively. The resistivity is measured by flowing current along the *c*-axis.

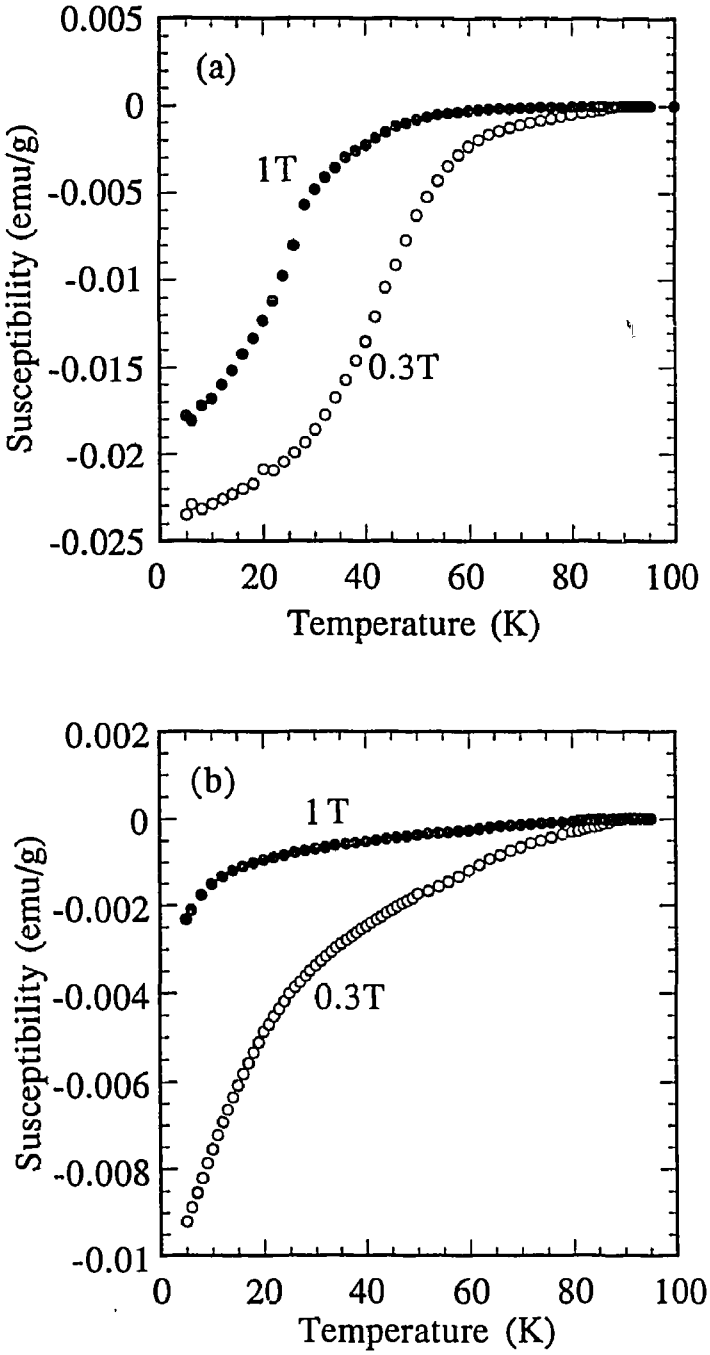

Fig. 2-15. Temperature dependence of the magnetic susceptibility of an O_2-annealed $YBa_2Cu_3O_x$ single crystal under magnetic fields of 0.3 and 1 T applied along or perpendicular to the *c*-axis in (a) and (b), respectively.

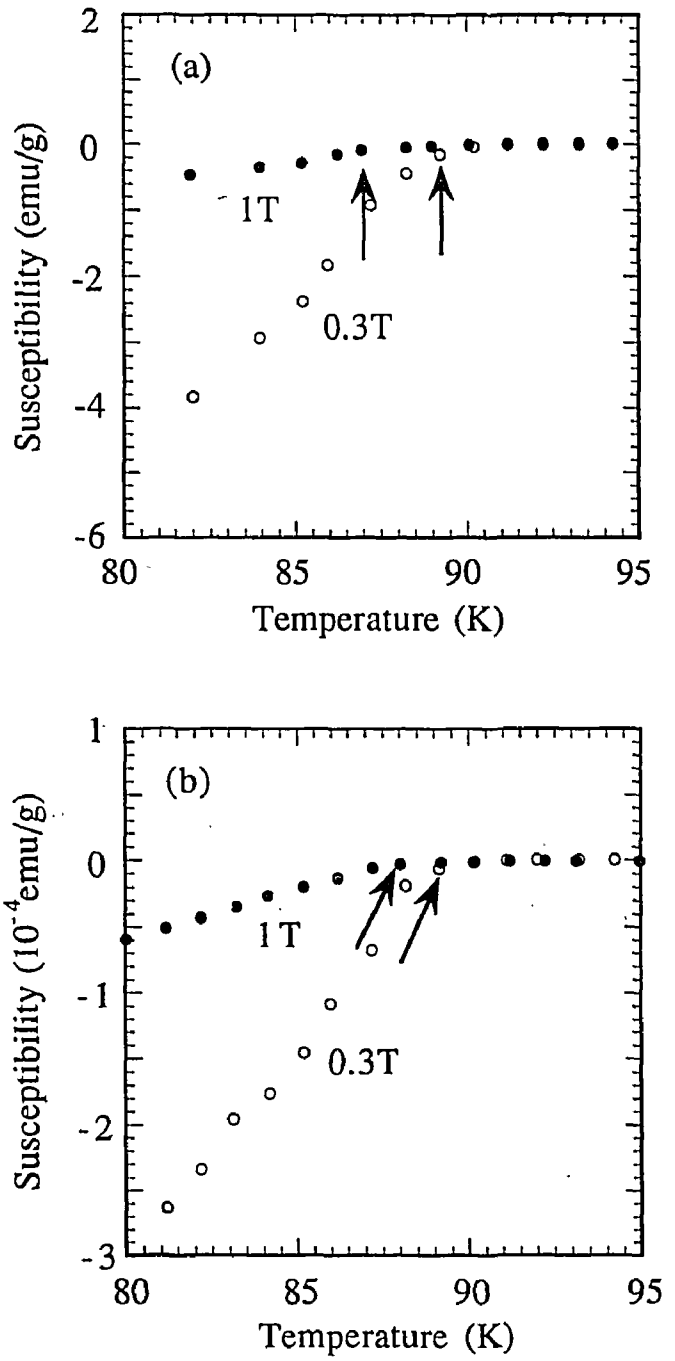

Fig. 2-16. Temperature dependence of the magnetic susceptibility of an O_2-annealed $YBa_2Cu_3O_x$ single crystal around the transition range under magnetic fields of 0.3 and 1 T applied along or perpendicular to the *c*-axis in (a) and (b), respectively.

Chapter 3. Crystal Growth Mechanism of $YBa_2Cu_3O_x$ Single Crystals from a Coexisting Region of a Solid with a Melt

3.1 Introduction

Large, isometric and high-quality single crystals of $YBa_2Cu_3O_x$ (123), which are undoubtedly one of the most important materials to understand the mechanism of high-temperature superconductors, are in great demand and numerous trials have been carried out so as to satisfy this demand. The crystals which have commonly been prepared from high-temperature solutions are thin plates with small aspect ratios (thickness/diameter).[17-24] Wolf *et al.*[25] and Schönmann *et al.*[26] have prepared single crystals with a thickness of up to 2 mm by very slow cooling of the solution to 970~960°C. On the other hand, we succeeded in synthesizing large isometric 123 single crystals with a maximum thickness of about 7 mm along the *c*-axis under the conditions where the solid Y_2BaCuO_5 (211) and the melt phase existed together. At temperatures below the peritectic point, the reaction proceeds so as to form the 123 layers on the surface of 211 particles as shown in Eq. (2.1). We think that growth of the crystals progressed due to the peritectic reaction (2.1) between 211 and the surrounding melt phase.[62] The utility of such a crystallization technique from solid-melt mixtures will increase because of its easiness in obtaining large, single crystals of metastable or unstable materials at high temperatures. However, the growth mechanism has yet to be clarified.

This chapter describes the 123 crystal growth mechanism due to the peritectic reaction, which was investigated using a quenching technique. Discussions were carried out in terms of the Ostwald ripening mechanism on the growing interfaces under the coexisting conditions of the solid and

the surrounding melt.

3.2 Experimental

The solid-melt mixtures were prepared according to the same method as that described in Section 2.2.2. Starting materials of 123 powders and $7BaCO_3$-18CuO mixtures were prepared from the reagent powders of Y_2O_3, $BaCO_3$ and CuO with the 99.9% purity by sintering. They were packed into five aluminum crucibles, which were buried in bubbled ZrO_2 to minimize the differences in their temperatures, as shown in Fig. 3-1. The typical heat treatment was: heating the furnace from room temperature to 1050°C, and soaking at this temperature for 6~12 h. According to the phase diagram of Dembinski *et al.*,[52] this condition lies in a two-phase region of the solid 211 and the melt. The mixtures were cooled in the range 1~0.5°C/h, when the mixtures reached a temperature below the peritectic line, three phases, 123, 211 and the melt appeared under the predescribed peritectic reaction (2.1). To observe the growing interfaces of the solidifying 123 phase, as well as the composition changes, the samples at various temperatures between 1050 and 900°C were quenched by dropping the samples into liquid N_2. To observe the microstructures, the samples were embedded in resin and polished in to a fine surface finish using 1 μm diamond paste, and finally, carbon was coated by evaporation over the entire surface. The microstructures of the cross section at several different positions in the samples were observed using a polarized optical microscope and an electron probe X-ray microanalyser (EPMA). The samples were powdered and a phase identification was made using the X-ray powder diffraction method. The experiments were all carried out under atmospheric conditions.

3.3 Results and discussion

Changes in the X-ray powder diffraction patterns at different quenching temperatures are shown in Fig. 3-2. The main peaks correspond to the 211 phase at 1010°C, indicating that the condition lies in the two-phase region of the solid 211 and the melt. The weak peaks existing in all the X-ray diffraction patterns are $BaCuO_2$ and CuO. They are considered to be formed by quenching, because the intensity of these peaks is constant for all quenching temperatures between 1010 and 970°C. When the mixtures reached 980°C, the diffraction pattern of the 123 phase appeared, which is supposed to be formed by the peritectic reaction (2.1) of 211 and the coexisting melt phase. As the temperature was lowered to 970°C, the peak intensity due to the 123 phase increased, whereas that of the 211 peaks decreased. These results indicate that the growth of 123 crystals is controlled due to the progress of the peritectic reaction (2.1).

Observations of the interface regions of the 123 phase quenched at various temperatures lead to the following results: as the temperature was lowered to the peritectic point, the content of the mixtures changed from a two-phase region of the 211 particles and the melt to a three-phase region, the nuclei of 123, the 123-coated 211 particles and the melt. The 123 phases, which were formed by the peritectic reaction (2.1), have rough surfaces of about 10 μm in thickness or diameter, as shown in Fig. 3-3(a). The diffusion feature of the yttrium ingredient to the surrounding melt was observed by its concentration mapping, as shown in Fig. 3-3(b). The gray grains and black matrices are defined as 123 and the melt, respectively. It should be noted that the diffusion feature was almost completely independent of the interfacial condition between the solid and the melt, because the uneven signal intensity was observed on the polished flat surface, as shown

in Fig. 3-3(b). Fig. 3-4(a) shows an X-ray reflection mapping with Y-concentration on the sharp, faceted 123 crystals formed on the 211-melt interfaces. Fig. 3-4(b) represents a background reflection of Y which was obtained from a carbon-coated resin prepared under the same condition as the specimen. It is clean that the signal intensity of the melt (liquid phase) in the specimen is 5~20 times stronger than that of the region, indicating that the dissolution and diffusion of Y into the melt apparently occur at the peritectic condition. Figures 3-5(a), 3-5(b) and 3-5(c) show the diffusion features of the yttrium, barium and copper contents from the 123 phase having an acute angle or a small curvature radius to the surrounding melt and Figures 3-6 is the illustration. The figures reveal the active diffusion of these contents from the top of the acute angled phase to the melt. This means that the phase of the 123 compound dissolves and diffuses from the position of the higher interface free energy of the solid.

It is normal to consider that the formation of the 123 peritectoid around 211 particles reduces the reaction rate because the diffusion velocity of the reactant through the solid peritectoid is generally very low, and this situation is thought to be very unfavorable for growing the 123 crystals. The present observations suggest that the reduction of the peritectic reaction (2.1) is overcome by a large solubility of the 123 peritectoid to the surrounding melt, as shown in Fig. 3-7(a). In addition to this, the Ostwald ripening mechanism should act during this situation, where small particles tend to disappear and large ones become more large. Therefore, the 123 peritectoid formed on the small 211 particles are peeled off and the reaction from 211 to 123 progresses. On the other hand, the 123 crystals, possessing flat surfaces, have a high ability to gather the nutrient molecules of 123, as shown in Fig. 3-7(b).

The driving force for the volume diffusion of the Ostwald ripening has

the following Gibbs-Thomson's effect:

$$\log_e \frac{C(r)}{C(\infty)} = \frac{A}{r} \qquad (3.1)$$

$$A = \frac{2\rho V}{RT} \qquad (3.2)$$

where $C(r)$ and $C(\infty)$ are the concentrations of the liquid that are in equilibrium with the particles having the radii r and ∞, A the activation energy for the Ostwald ripening, s the surface free energy, V the molecular volume, R the gas constant and T the temperature. $C(\infty)$ becomes minimum in the growing interfaces of the solidified 123 phase in three-phase region, 123, 211 and the melt. As the temperature increases to 1000°C, s decreases and becomes very small, and T has a sufficiently high enough value. Therefore, A in Eq. (3.2) is very small in a high-temperature solution, and the diffusion layers whose thicknesses are d and d' are formed at the interfaces of the particles having r and ∞ radii, respectively. The layers are supposed not to be the rate limiting stage of growing the 123 crystals, as can be seen in Fig. 3-8.

Typically the single crystals obtained have shiny flat surfaces of {1 0 0} and {0 0 1}, or are surrounded by {1 0 0}, {0 0 1} and {0 9 10} surfaces, as shown in Fig. 2-8. In accordance with the anisotropy of the surface free energy, the sharp corners, which have a small curvature, tend to act as a growth site, and the {0 9 10} surfaces appears.

3.4 Summary

The crystal growth mechanism of 123 from a mixed region of the solid 211 and the melt was investigated regarding the quenched samples between 1050 and 900°C using a polarized optical microscope, EPMA and the X-ray powder diffraction method. The observations of the growing interfaces

of the solidified 123 phase in the three-phase region revealed diffusion of the 123 phase to the surrounding melt, and consequently, the Ostwald ripening mechanism plays an important role for growing 123 crystals on the solid-melt interfaces. These facts support the idea that the growth of 123 crystals progresses due to the peritectic reaction between the solid 211 phase and the surrounding melt.

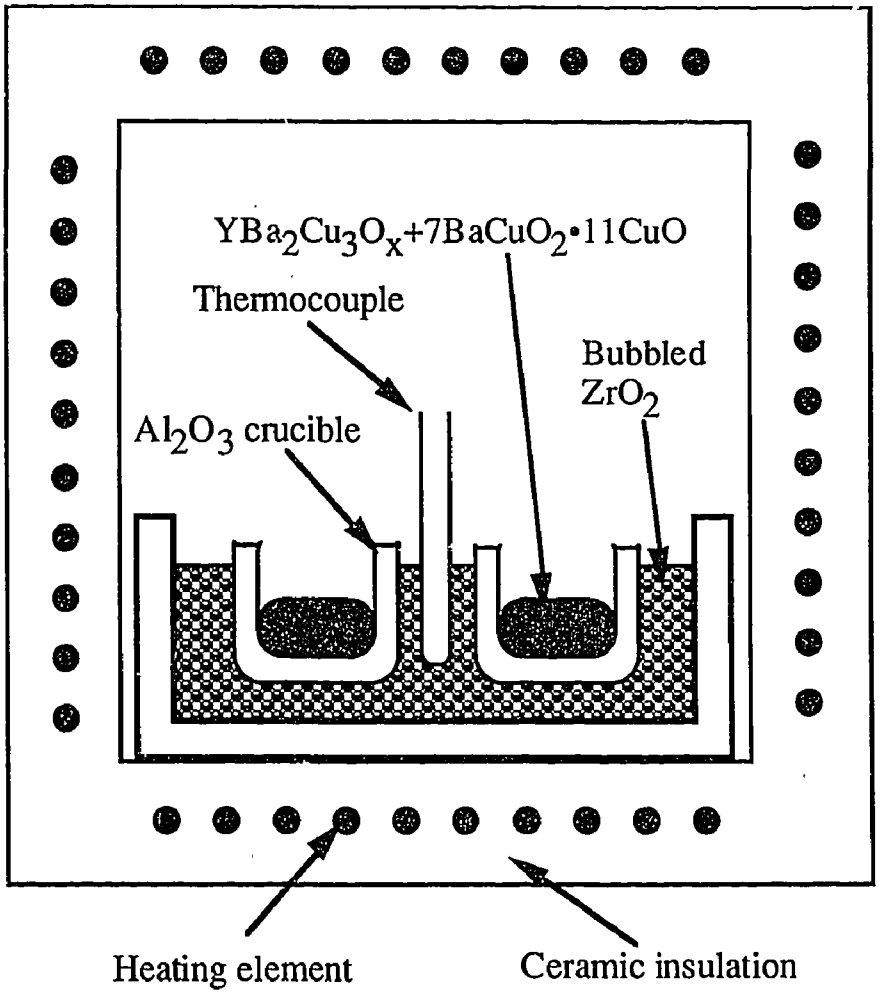

Fig. 3-1. Arrangement of the crucibles in a muffle furnace for preparation of solid-melt mixtures due to the peritectic reaction.

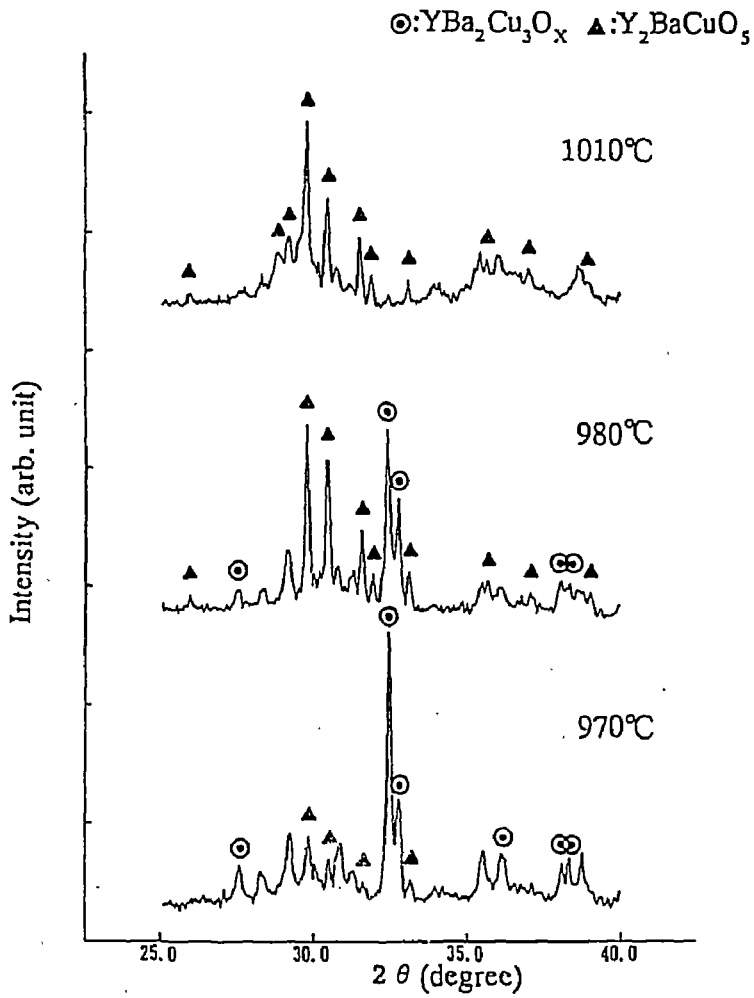

Fig. 3-2. Changes in the X-ray powder patterns of $YBa_2Cu_3O_x$-7$BaCuO_2$·11CuO mixed phase as a function of the quenching temperature. An increase in the diffraction peak intensity of the $YBa_2Cu_3O_x$ phase can be observed as the temperature is lowered.

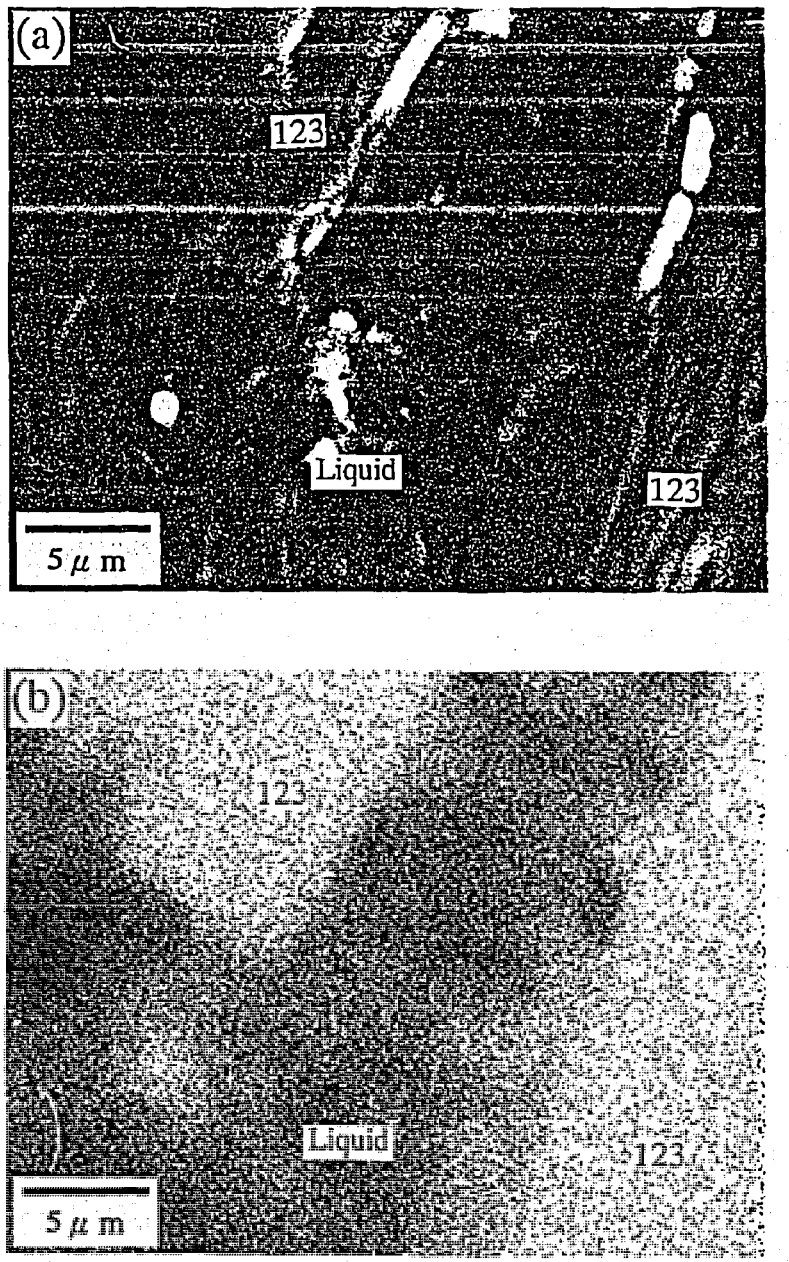

Fig. 3-3. Observations of the solidified $YBa_2Cu_3O_x$ phase at 980°C due to quenching. (a) Microstructures of $YBa_2Cu_3O_x$ layers, which were formed due to the peritectic reaction. (b) Yttrium concentration mapping image of the same specimen as (a). The phases are labeled as follows: 123: $YBa_2Cu_3O_x$, 211: Y_2BaCuO_5

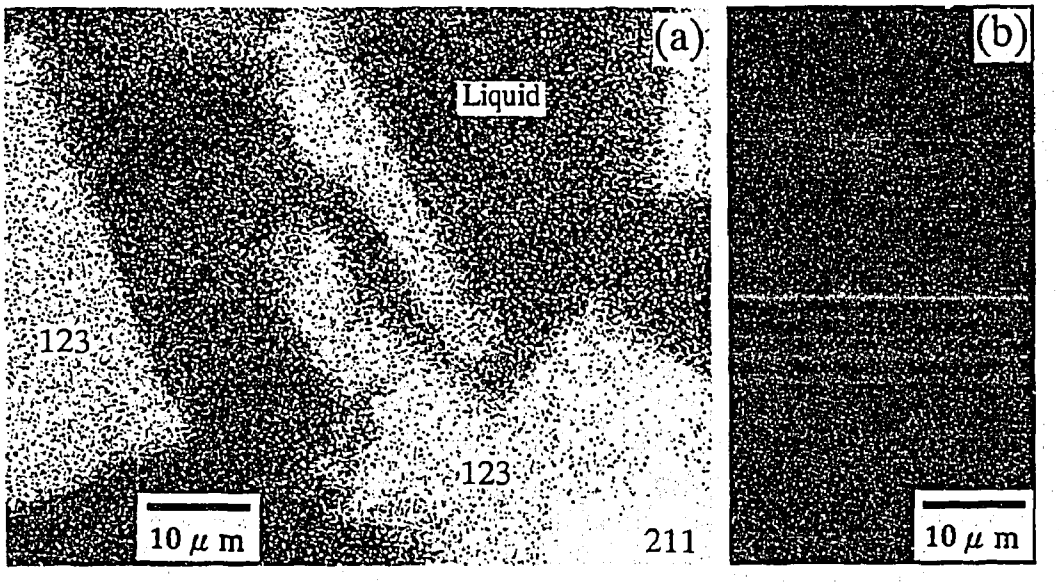

Fig. 3-4. Yttrium concentration mapping images of (a) the growing interface of the $YBa_2Cu_3O_x$ single crystal and (b) the background. The phases are labeled as follows: 123: $YBa_2Cu_3O_x$, 211: Y_2BaCuO_5

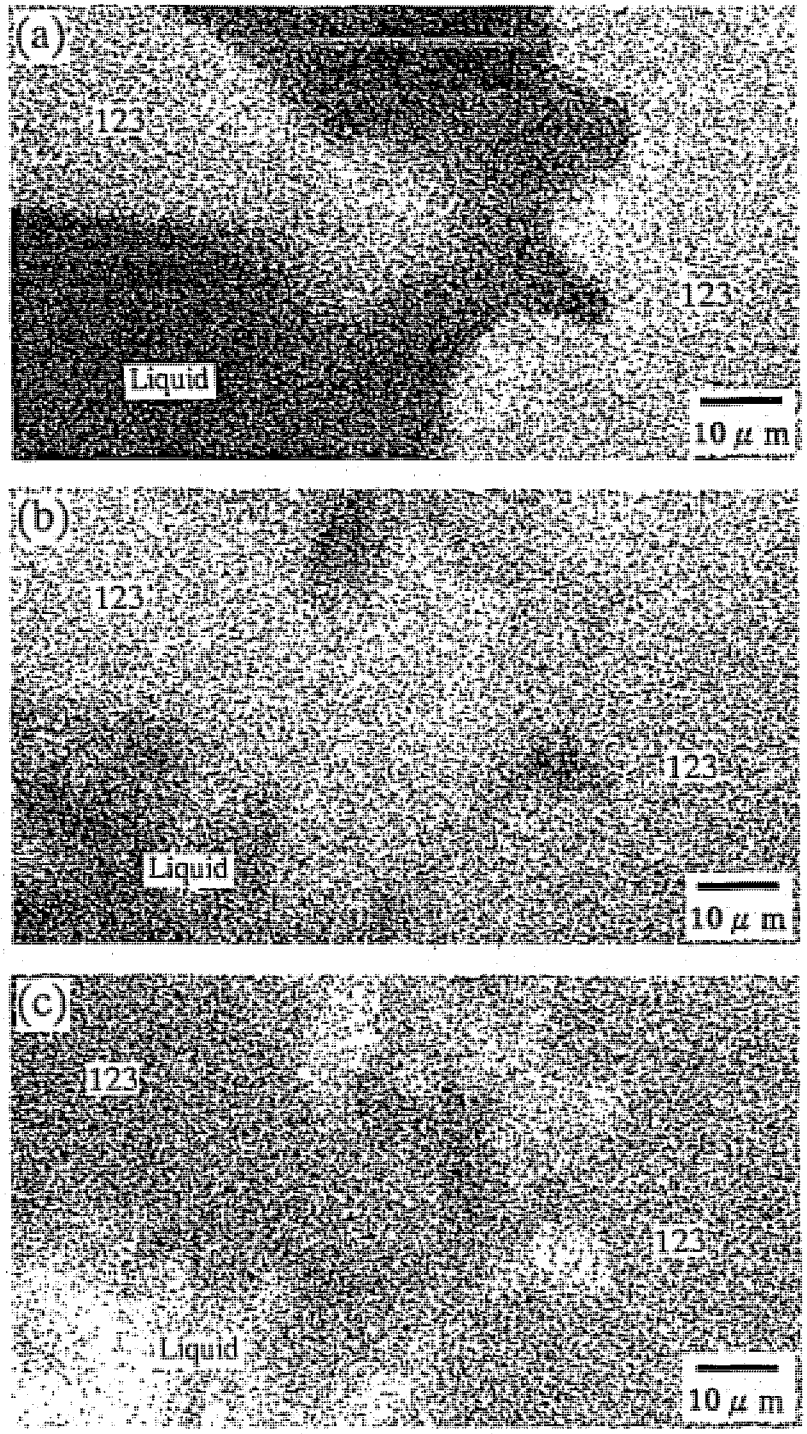

Fig. 3-5. Diffusion features of (a) yttrium, (b) barium and (c) copper contents from the top of the $YBa_2Cu_3O_x$ phase to the ambient melt. The phases are labeled as follows: 123: $YBa_2Cu_3O_x$, 211: Y_2BaCuO_5

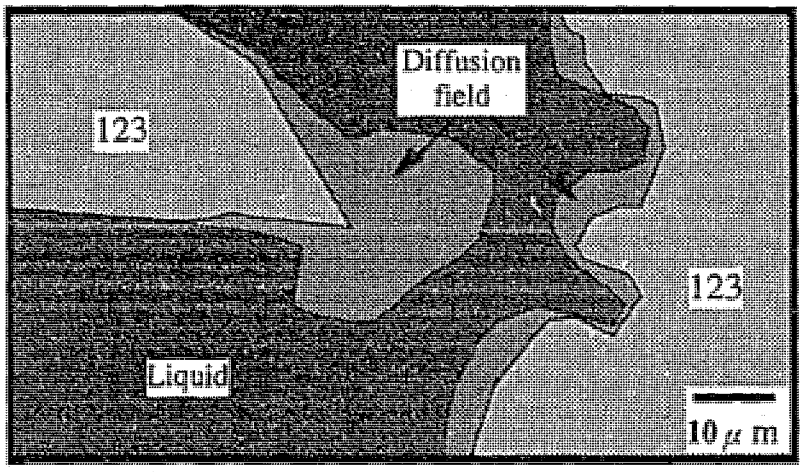

Fig. 3-6. Illustration of the diffusion features from the top of the $YBa_2Cu_3O_x$ phase to the ambient melt. The phases are labeled as follows: 123: $YBa_2Cu_3O_x$, 211: Y_2BaCuO_5

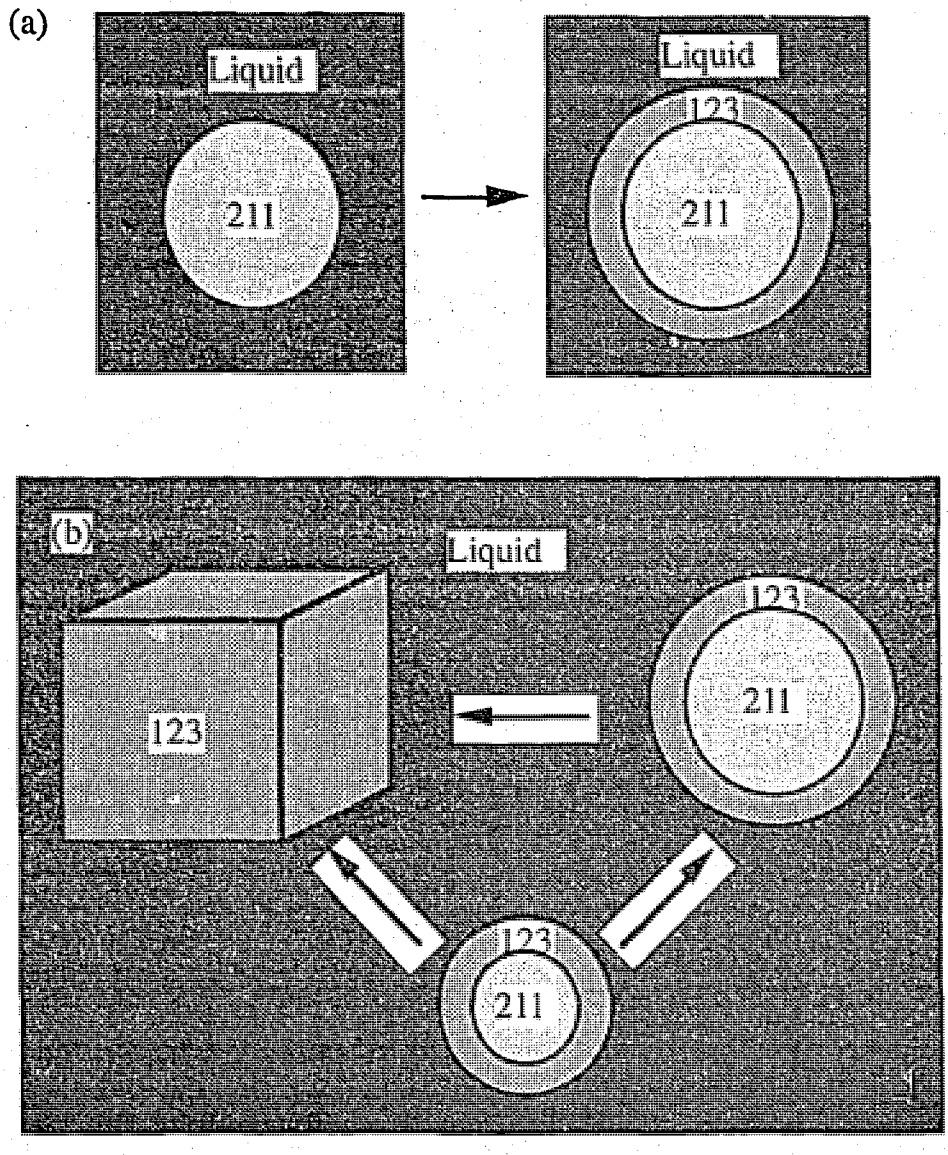

Fig. 3-7. (a) Illustration of a formation of the $YBa_2Cu_3O_x$ layer due to the peritectic reaction. (b) Illustration of the Ostwald ripening mechanism. The phases are labeled as follows: 123: $YBa_2Cu_3O_x$, 211: Y_2BaCuO_5

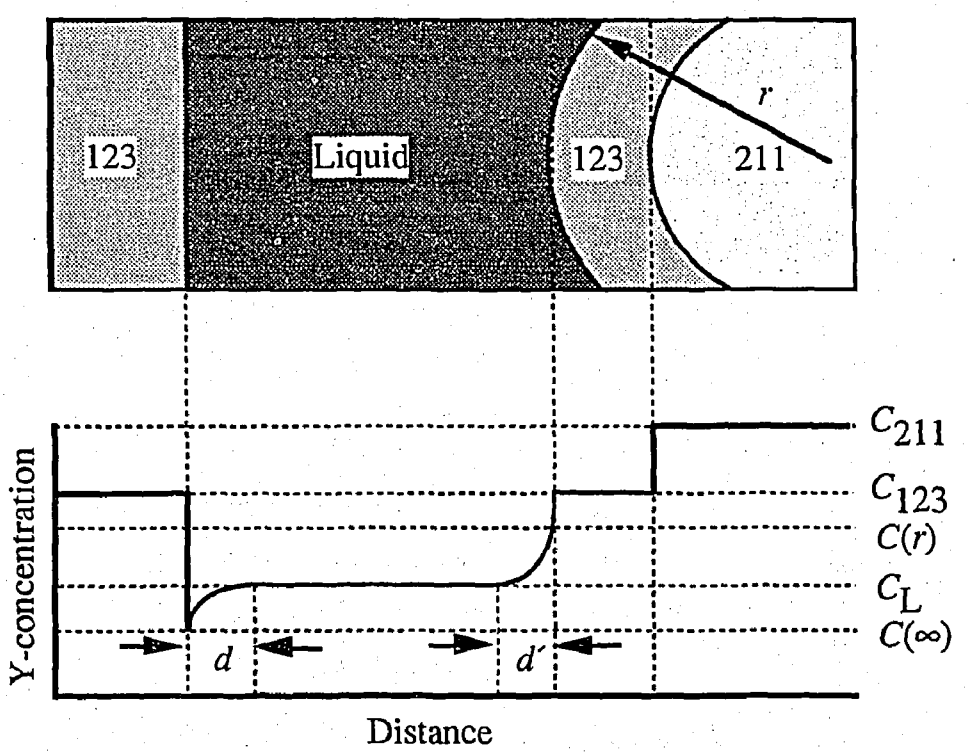

Fig. 3-8. Illustration of the dissolution of the curved $YBa_2Cu_3O_x$ phase formed on Y_2BaCuO_5 phase due to the peritectic reaction and the growth of $YBa_2Cu_3O_x$ single crystal having sharp flat surface. The phases are labeled as follows: 123: $YBa_2Cu_3O_x$, 211: Y_2BaCuO_5

Chapter 4. Influence of Growth Condition of Solid-Melt Mixtures on Flux Pinning in $YBa_2Cu_3O_x$ Single Crystals

4.1 Introduction

The critical current density (J_c) is important both for fundamental studies of superconductivity and for practical applications. Impurities and defects increase the current carrying ability of superconductors. For $YBa_2Cu_3O_x$ (123) single crystals, several kind of defects such as, point defect,[31,32] dislocation,[33] twin boundary[34-44] and grain boundary[32,45] have been identified. In the vortex state of type-II superconductors, a supercurrent can flow without resistance in the presence of a high magnetic field below a threshold, the upper critical field (H_{c2}). Below H_{c2}, as the external field partially penetrates into the superconductors, it forms magnetically and elastically flexible flux lines which are usually quantized with normal cores. The transport supercurrent interacts with the flux lines and generates a Lorentz force which tends to push the flux lines away from equilibrium position. Such a phenomenon called "flux flow" generates an electric field in the superconductors, and the material becomes normal. In type-II superconductors, various crystal defects inevitably exist and interact with flux lines, preventing them from flowing. Flux pinning is usually a term to characterize such a flux line-defect interaction. Obviously, the strong the flux line-defect interaction enhances the pinning effect, and thus, a high J_c value is produced.

To understand the pinning mechanism and achieve high J_c for practical applications, we synthesized the 123 single crystals from various conditions of the solid 211 and the melt existed together. In this chapter is focused on the relationship between the critical current behavior and the crystal defects.

4.2 Experimental

4.2.1 Crystal growth from various conditions of solid-melt mixtures

The concentration of 123 in the solution was systematically changed with the ratio of 1/6 (123) to 1/25 ($7BaCuO_2 \cdot 11CuO$) between 3:7 and 6:4. Under these conditions, 123 single crystals were grown from the coexisting region of the solid 211 phase with the melt according to the phase diagram.[32] The typical heat treatment was carried out, as described in Section 2.2.2. Oxygen annealing was carried out at 550°C for a week under oxygen pressure of 5 atm so as to increase the oxygen content in the as-grown crystals. The content of oxygen was determined by an iodometric titration under argon atmosphere. The microstructures of cross section were observed using a polarized optical microscope, a SEM-EPMA and a TEM

4.2.2 Magnetization

Measurements of magnetization were made between 5 and 80 K under the external field $H//c$ using a magnetometer with a superconducting quantum interference device (SQUID, Quantum Design model MPMS), where the external magnetic fields up to 5.5 T were used. Samples were cooled to a desired temperature in a zero magnetic field. A scan length of 3 cm was provided a field uniformity of ≤0.05% during the measurements. A target temperature was stabilized to within ±0.05 K.

For the measurements of magnetic relaxation, the sample was cooled to a desired temperature in a zero field, the external magnetic field was raised to 5 T, and then lowered to 1 T, and the isothermal magnetization M as a

function of time was recorded over a period ranging from 25 to 20600 s.

4.3 Results and discussion

We succeeded in synthesizing the 123 single crystals from the mixtures whose compositional ratios of the solid 1/6 (123) to the melt 1/25 ($7BaCuO_2 \cdot 11CuO$) were 3:7, 4.5:5.5 and 6:4. The cross sections perpendicular to the *c*-axis were inspected under the optical microscope and SEM. Figures 4-1, 4-2 and 4-3 show that the number of voids increased as the concentration of melt phase decreased. The compositional distribution of the constituent metal atoms on the cross sections was determined by EPMA and TEM. The data supported the findings that the crystals were very homogeneous in Y, Ba and Cu, and that an actual 211 phase did not exist in the 123 single crystals when the mixture was held at a temperature between 1010 and 980°C, below the peritectic line, for a sufficient period of heating. These results are evidence of the completeness of the reaction during 123 growth.

In the three phase region, the liquid phase plays an important role for growing the 123 crystals. At a temperature below the peritectic line, 123, 211 and the melt appeared under the presumed peritectic reaction of the solid and the melt phase. Then, the nutrient of 123 was supplied to the crystals through the melt phase. Decreasing the melt composition caused an insufficient supply of nutrient to the crystals, and consequently, imperfectly flat surface would be made.

The quality of single crystal specimens is normally evaluated by χ-T curves.[67,68] As shown in Fig. 4-4, sufficient shielding in a field of 1.0×10^{-3} T was observed in both the sharpness of the transition at T_c, and the required value of the diamagnetism at low temperature below T_c guarantees

the homogeneity of the crystals in an oxygen content. The Meissner fractions which is an index for a strong flux pinning force increased as the melt composition decreased.

Figure 4-5 shows hysteresis loops measured in the temperature range 10~80 K with $H//c$. The width of the loops increased as the melt composition decreased. Fishtail hysteresis loops were observed in the range 20~70 K, especially in the crystal which was grown from a solid-to-melt ratio of 6:4. The peak of fishtail hysteresis loops shifted to a high magnetic field as the temperature increased.

J_c depends on both the width of loop and sample dimension according to the Bean model.[70] We used the formula[71]

$$J_c=40M_{irr}/L, \qquad (4.1)$$

where M_{irr} is one-half the width of loop at a given field. $L=L_1[1-(L_1/3L_2)]$ is a characteristic lateral dimension, where L_1 and L_2 ($L_1 \leq L_2$) are the length of the sides in a rectangular crystal with the magnetic field applied perpendicular to that face. Figure 4-6 shows J_c measured in the temperature range from 5~80 K with $H//c$, representing that J_c increased as the melt composition decreased. The J_c value at 5 K in a field of near 0 T of the samples from the solid-to-melt ratios of 3:7, 4.5:5.5 and 6:4 were 9.7×10^5, 2.9×10^6 and 3.6×10^6 A/cm^2, respectively. The irreversibility line at 80 K shifted to a high magnetic field as the melt composition decreased.

Figure 4-7 shows a semilogarithmic plot of the temperature dependence of J_c at 1 T. An approximately exponential decrease of J_c with T was observed for $T<50$ K, and followed by a more sharp reduction at higher temperatures. This is consistent with many earlier reports.[72,73] The key observation about these data is that the relative values of J_c were enhanced with a decrease in the melt composition in 3-times at 5 K and 10-times at 80 K.

Effective pinning energy U can be estimated from the measurements of magnetic relaxation[74,75]

$$dM/dt=(B\omega a/2\pi r)\exp(-U/T), \qquad (4.2)$$

where B is the magnetic induction, ω is the attempt frequency for vortex hopping, a is the hopping distance, r is the sample radius, and the energies are measured in K. Solving for $U(J)$ gives

$$U(J)=-T(\ln|dM/dt|-C), \qquad (4.3)$$

where $C=\ln(B\omega a/2\pi r)$. In this work, we determine the C value by fitting the measurements of magnetic relaxation, so as to give the most smooth and continuous curves at low temperatures. This criterion gave the value $C=19$ for the three samples. The temperature scaling function G of U[76,77] is chosen as

$$G(T)=[1-(T/T_c)^2]^{3/2}, \qquad (4.4)$$

where $T_c=92.5$ K. Figure 4-8 shows the curves of $U(J,T)=U(J)/G(T)$ calculated from the measurements of magnetic relaxation. Each segment represents the data collected at a given temperature. The lowest temperature is located on the high J side. As the temperature increased, the J values decreased and $U(J,T)$ values increased. We found good enhancement of the value of $U(J,T)$ with a decrease in the melt composition.

4.4 Summary

We synthesized 123 single crystals from the mixtures whose compositional ratios of the solid 1/6 (123) to the melt 1/25 ($7BaCuO_2$•$11CuO$) were 3:7, 4.5:5.5 and 6:4 and focused on the relationship between J_c and the crystal defects. In the cross section of the three 123 crystals, the number of voids increased as the melt composition decreased . Sufficient shielding in a field was observed in both the sharpness of the transition at T_c, and the

required value of the diamagnetism at low temperature below T_c guarantees the high quality of the three crystals that are uniform in the 123 phase. The Meissner fractions, the magnetic current density and the effective pinning energy were greatly enhanced as the melt composition decreased, indicating a strong flux pinning force.

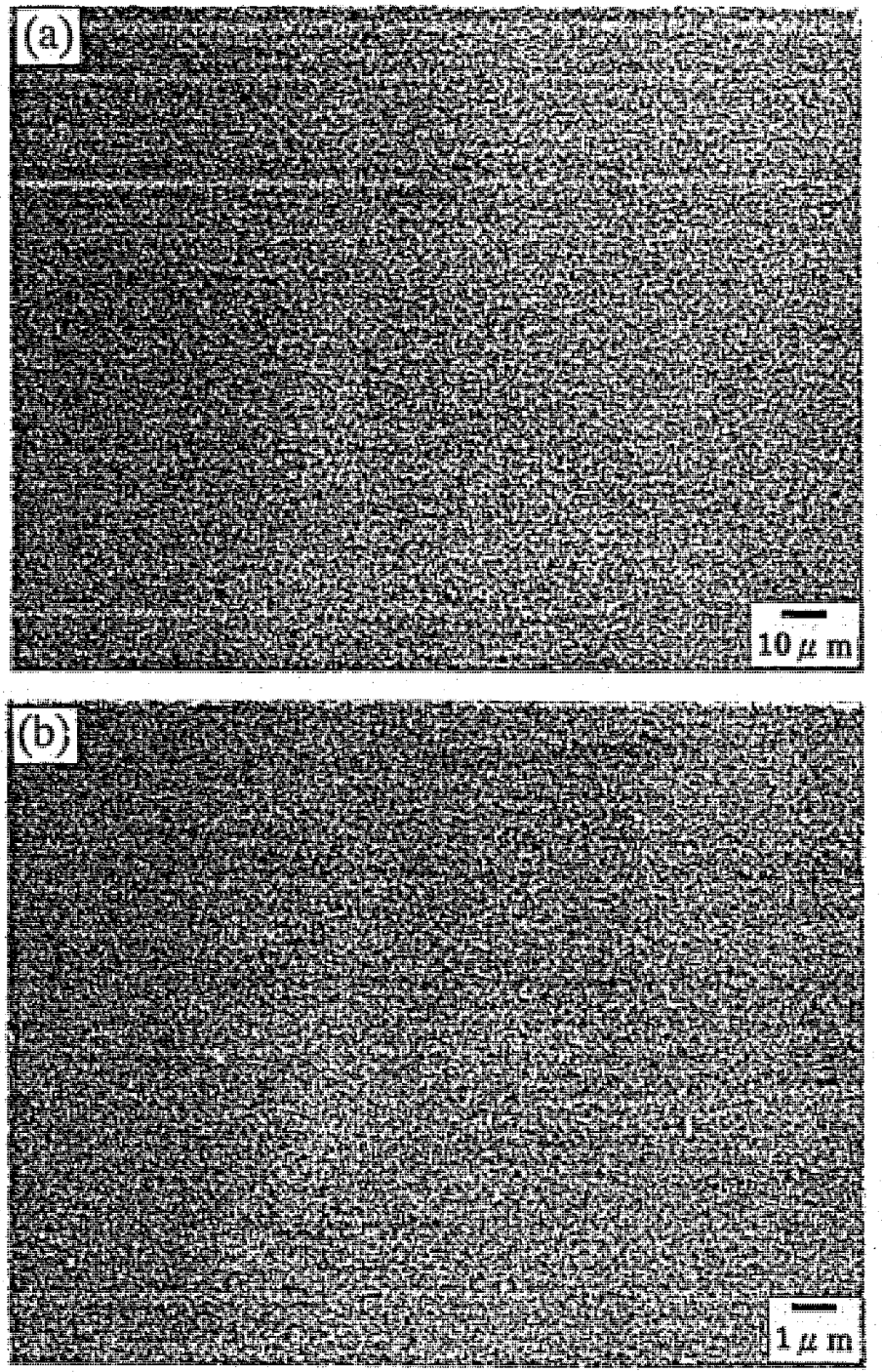

Fig. 4-1. (a) Cross sections perpendicular to the *c*-axis of a $YBa_2Cu_3O_x$ single crystal which was grown from the mixture whose compositional ratio of the solid 1/6 (123) to the melt 1/25 ($7BaCuO_2 \cdot 11CuO$) was 3:7 and (b) its magnification.

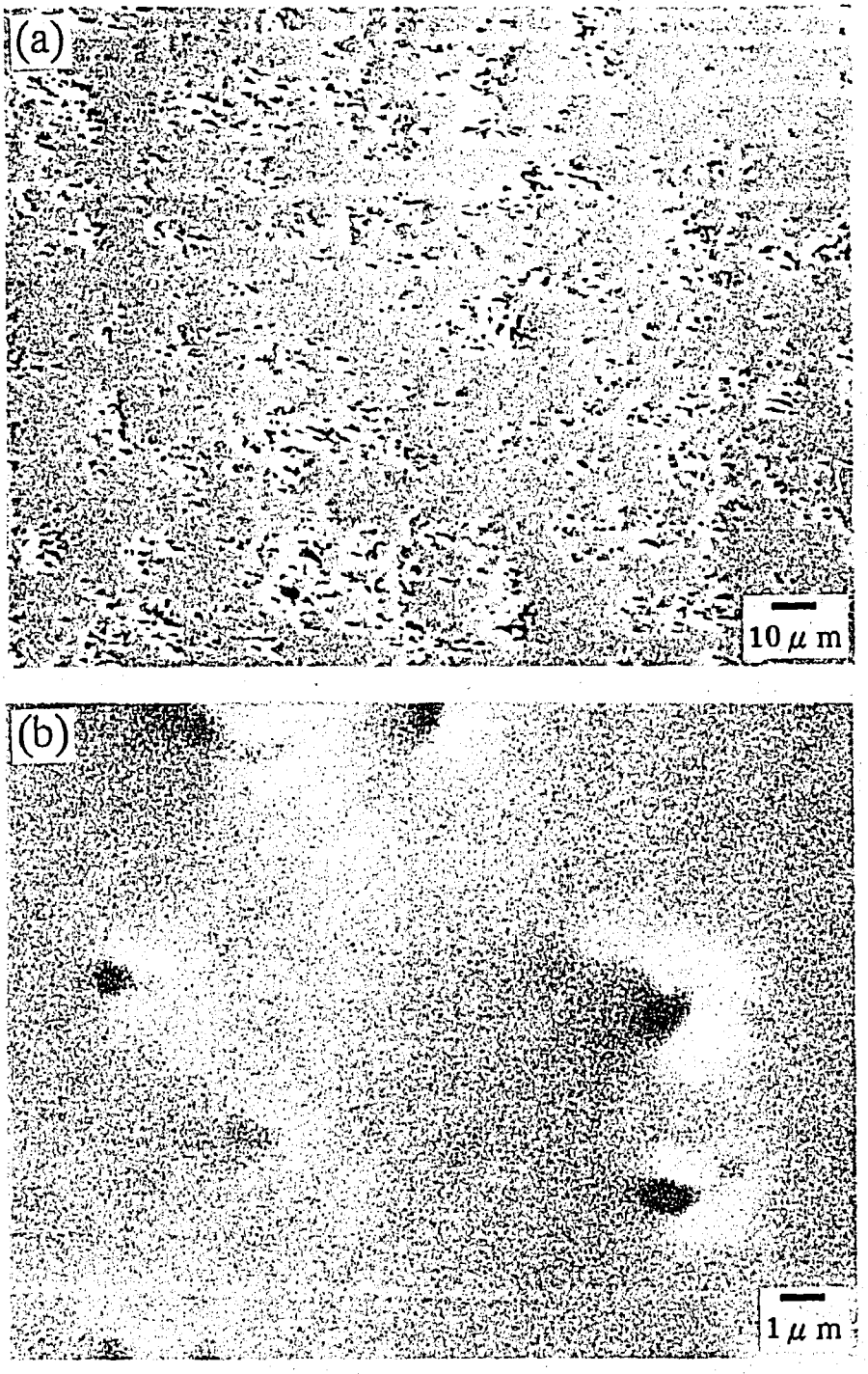

Fig. 4-2. (a) Cross sections perpendicular to the *c*-axis of a $YBa_2Cu_3O_x$ single crystal which was grown from the mixture whose compositional ratio of the solid 1/6 (123) to the melt 1/25 ($7BaCuO_2 \cdot 11CuO$) was 4.5:5.5 and (b) its magnification.

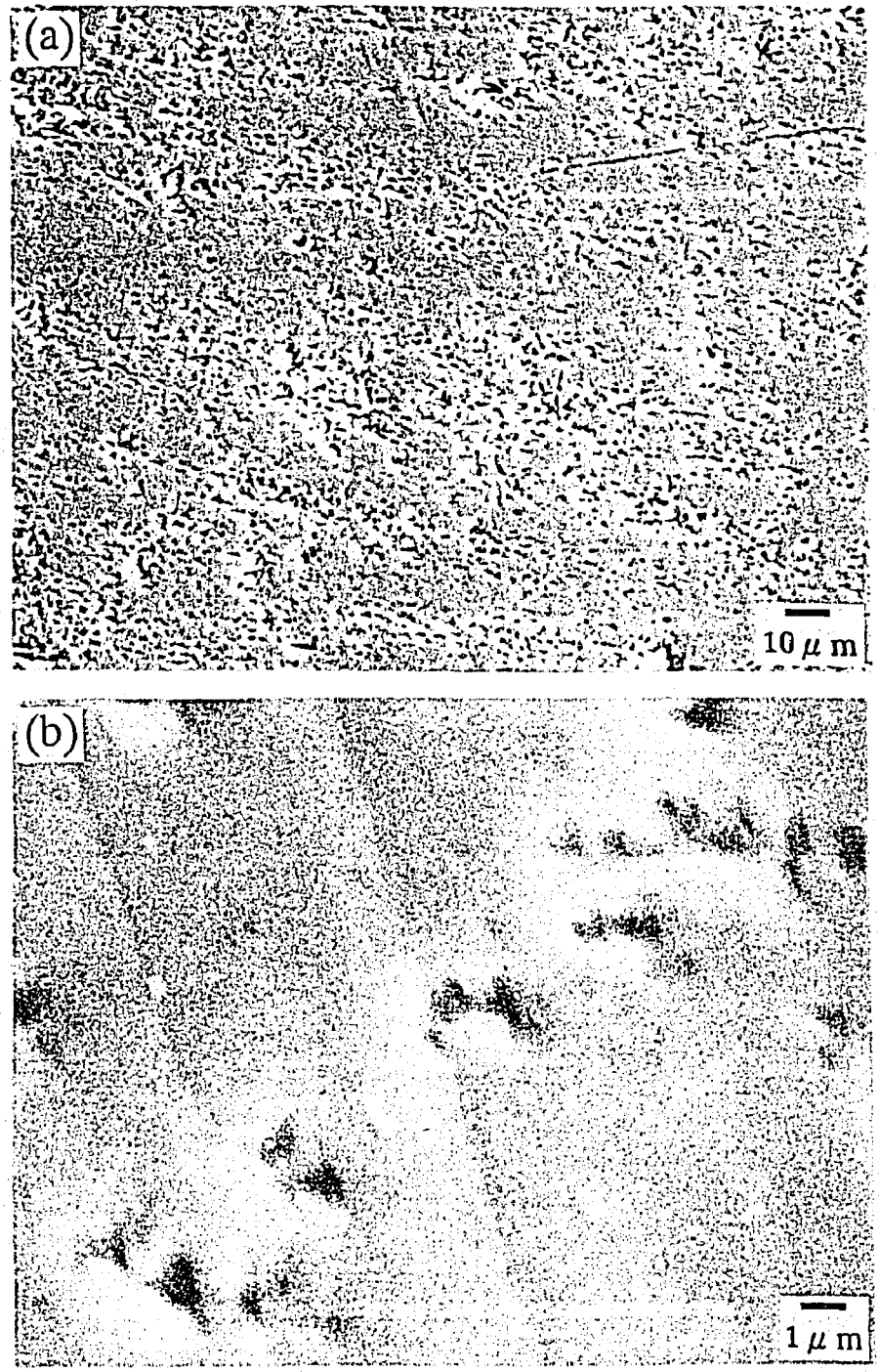

Fig. 4-3. (a) Cross sections perpendicular to the *c*-axis of a $YBa_2Cu_3O_x$ single crystal which was grown from the mixture whose compositional ratio of the soiid 1/6 (123) to the melt 1/25 ($7BaCuO_2 \cdot 11CuO$) was 6:4 and (b) its magnification.

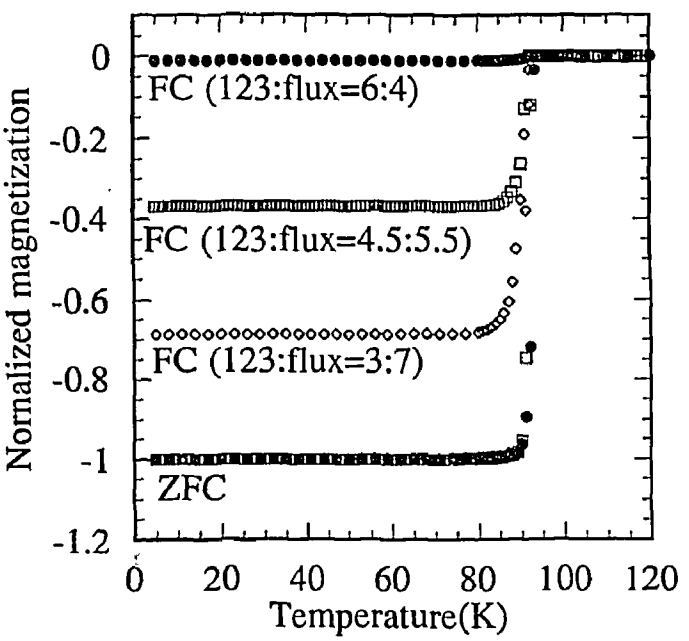

Fig. 4-4. Zero-field-cooled (ZFC) and field-cooled (FC) susceptibility of the three kinds of $YBa_2Cu_3O_x$ single crystals which were grown from the mixtures whose compositional ratios of the solid 1/6 (123) to the melt 1/25 ($7BaCuO_2 \cdot 11CuO$) were 3:7, 4.5:5.5 and 6:4. Magnetic field of 1.0×10^{-3} T was applied along the *c*-axis.

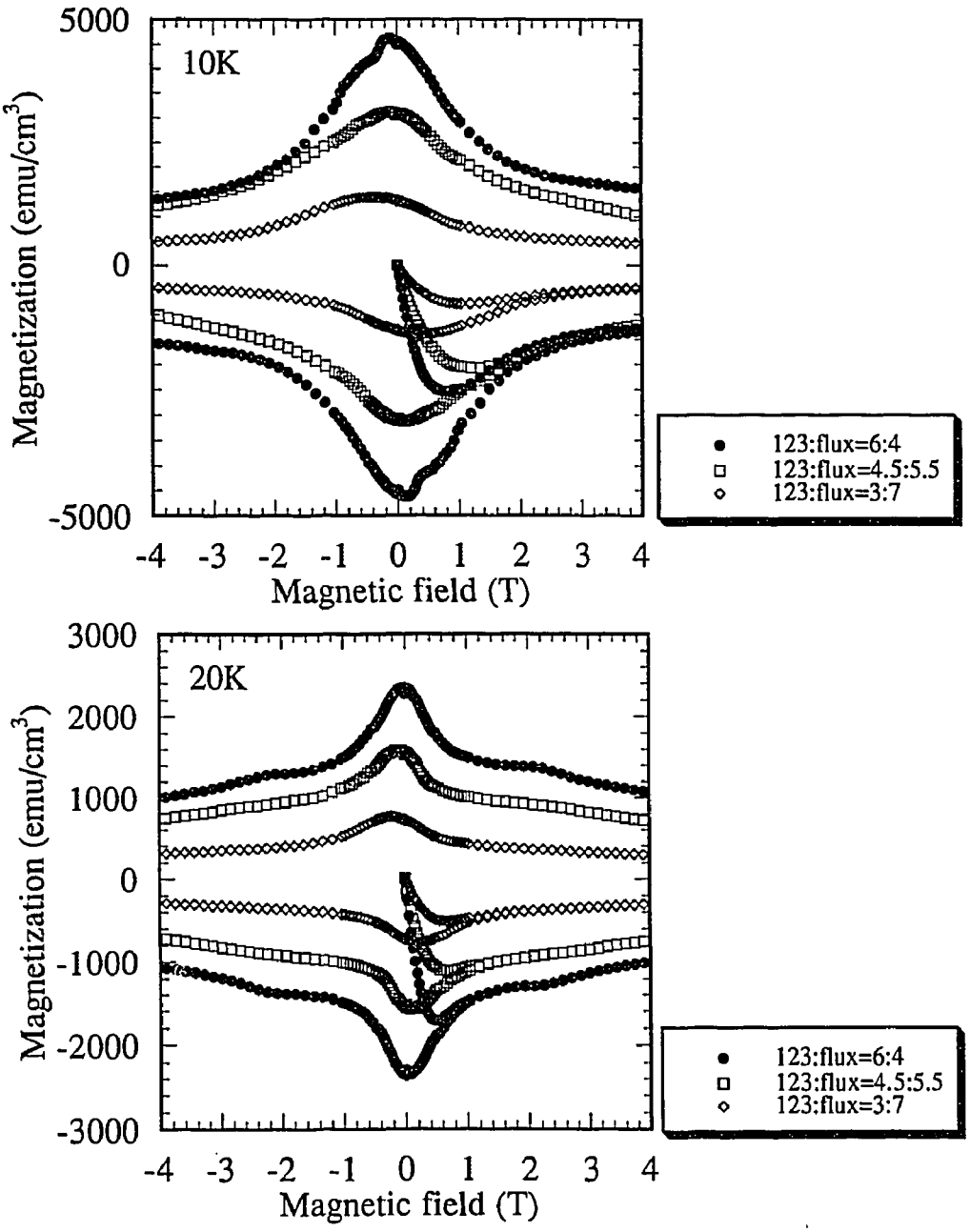

Fig. 4-5. Magnetization hysteresis loops of the three kinds of $YBa_2Cu_3O_x$ single crystals which were grown from the mixtures whose compositional ratios of the solid 1/6 (123) to the melt 1/25 ($7BaCuO_2 \cdot 11CuO$) were 3:7, 4.5:5.5 and 6:4. Magnetic fields up to 5.5 T were applied along the *c*-axis in the temperature range 10~80 K.

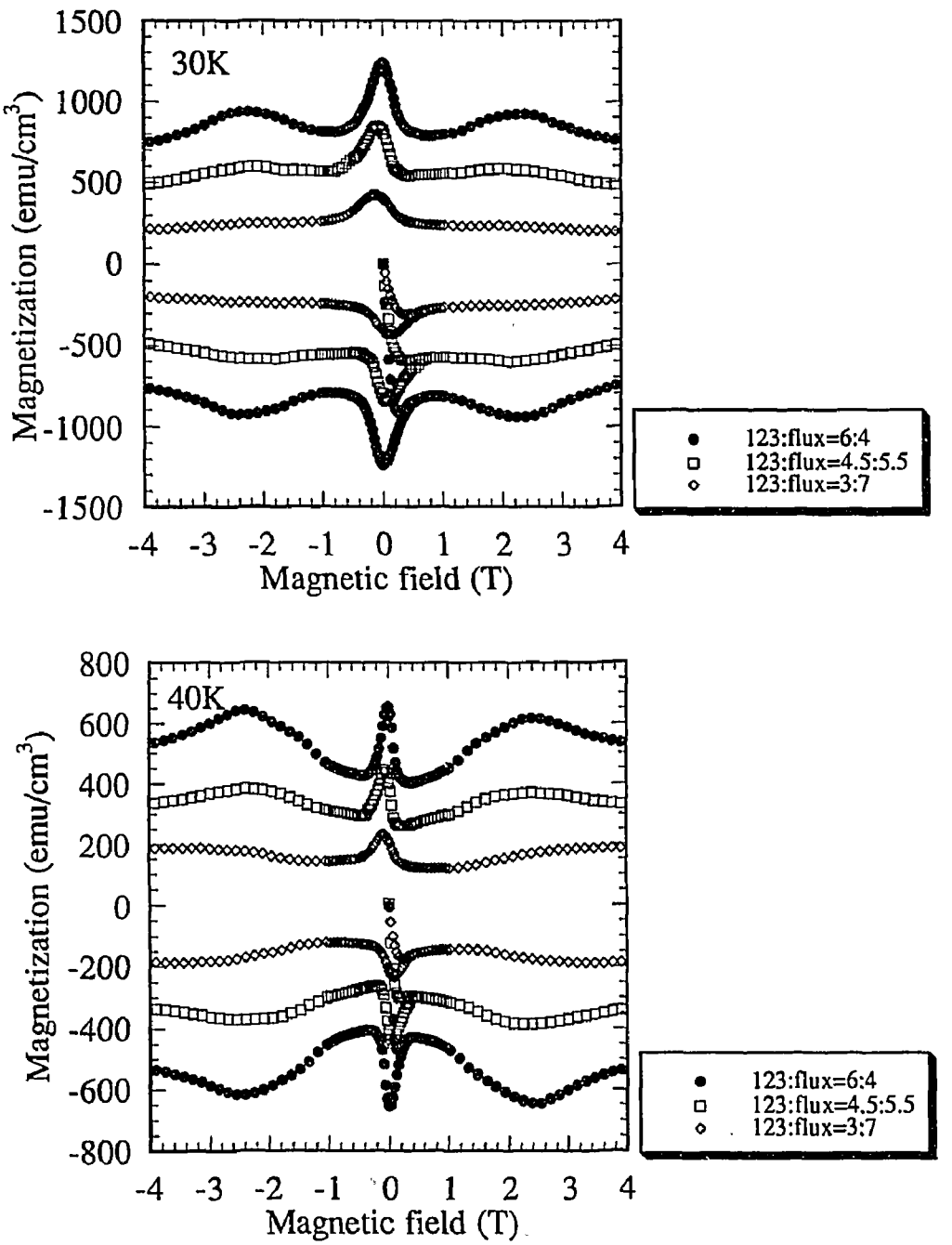

Fig. 4-5. (continued)

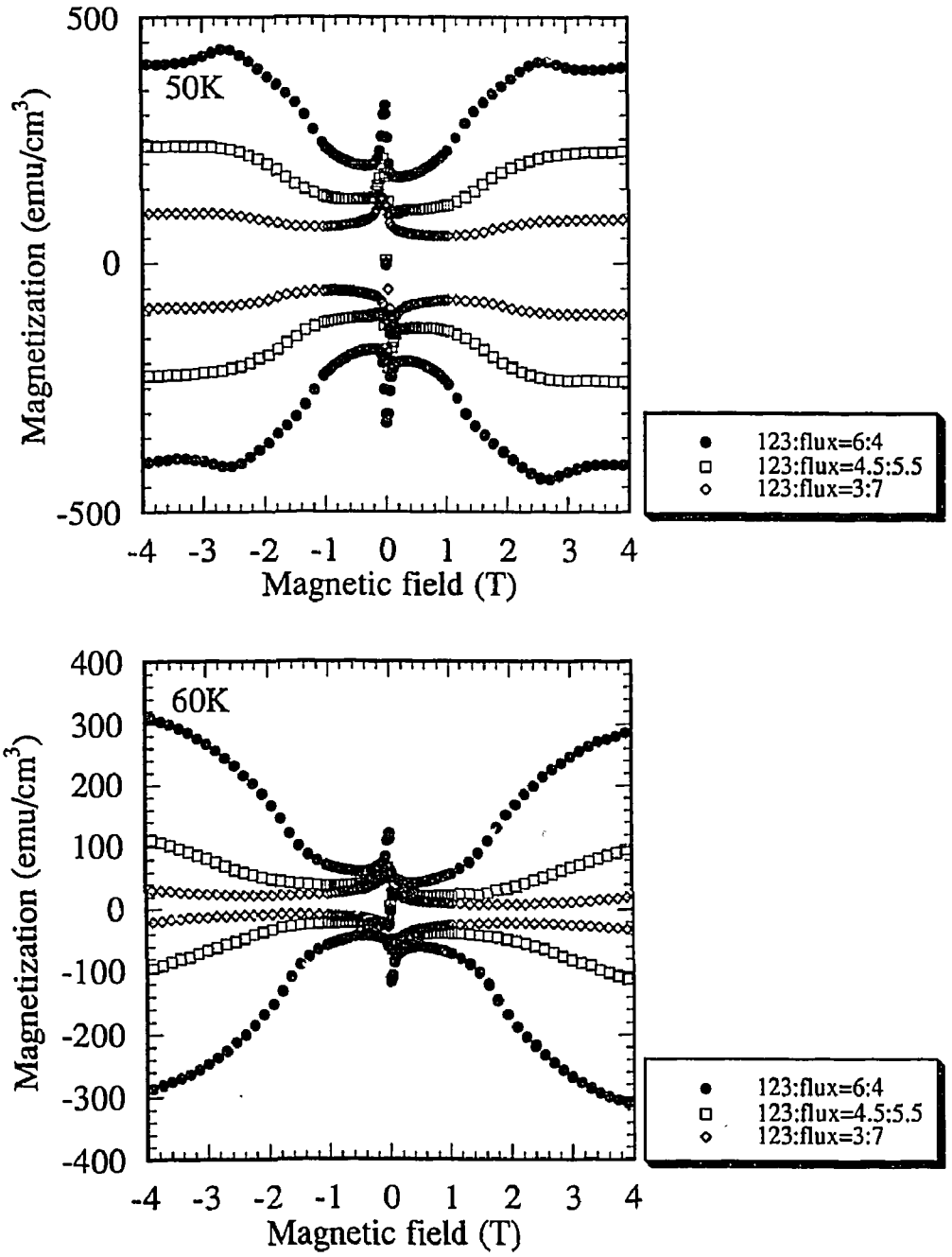

Fig. 4-5. (continued)

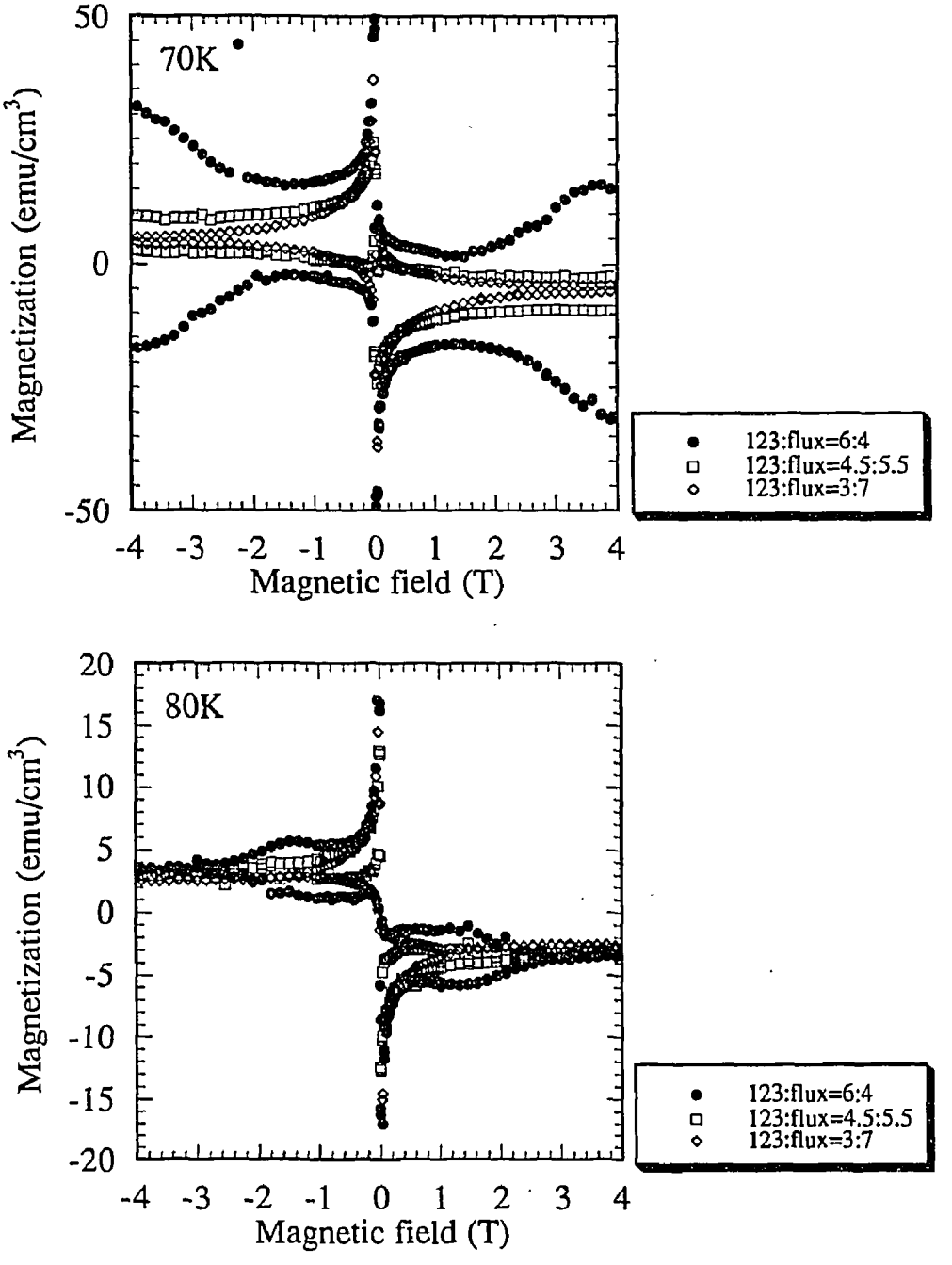

Fig. 4-5. (continued)

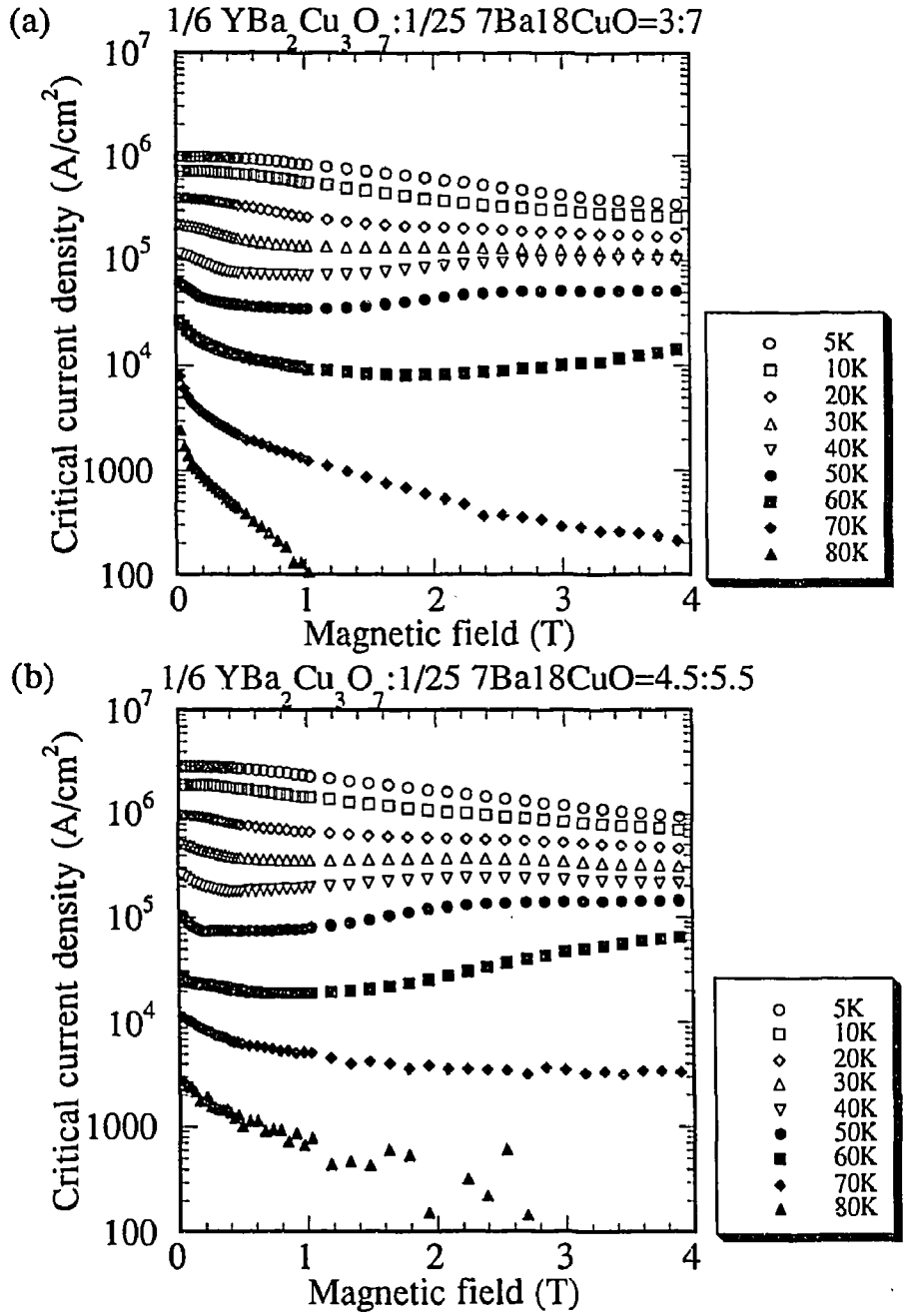

Fig. 4-6. Field dependence of the critical current densities of the three kinds of $YBa_2Cu_3O_x$ single crystals which were grown from the mixtures whose compositional ratios of the solid 1/6 (123) to the melt 1/25 ($7BaCuO_2 \cdot 11CuO$) were 3:7, 4.5:5.5 and 6:4. Magnetic fields up to 5.5 T were applied along the *c*-axis in the temperature range 10~80 K.

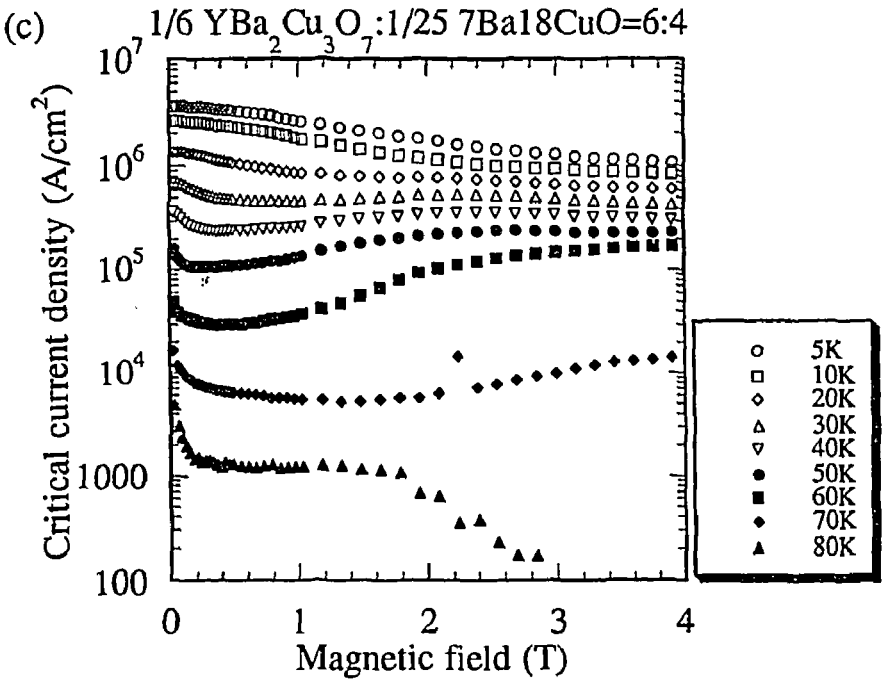

Fig. 4-6. (continued)

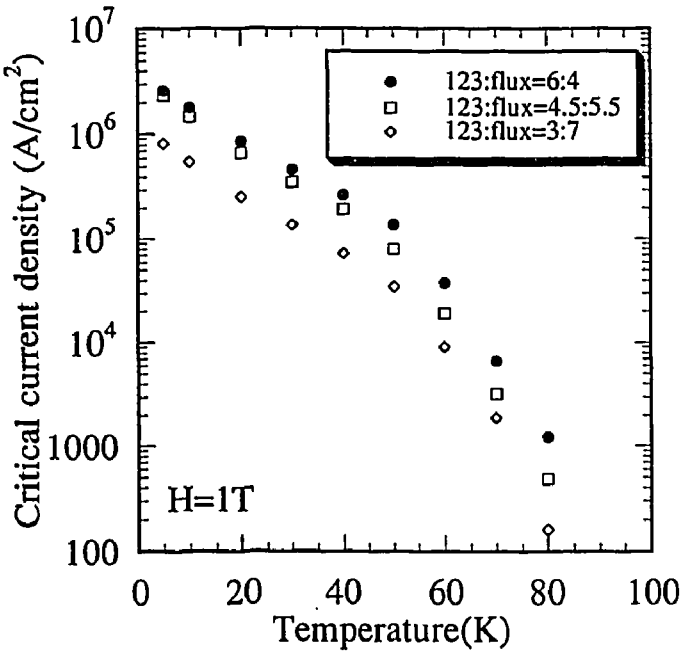

Fig. 4-7. Temperature dependence of the critical current densities of the three kinds of $YBa_2Cu_3O_x$ single crystals which were grown from the mixtures whose compositional ratios of the solid 1/6 (123) to the melt 1/25 ($7BaCuO_2 \cdot 11CuO$) were 3:7, 4.5:5.5 and 6:4. Magnetic field of 1 T was applied along the *c*-axis.

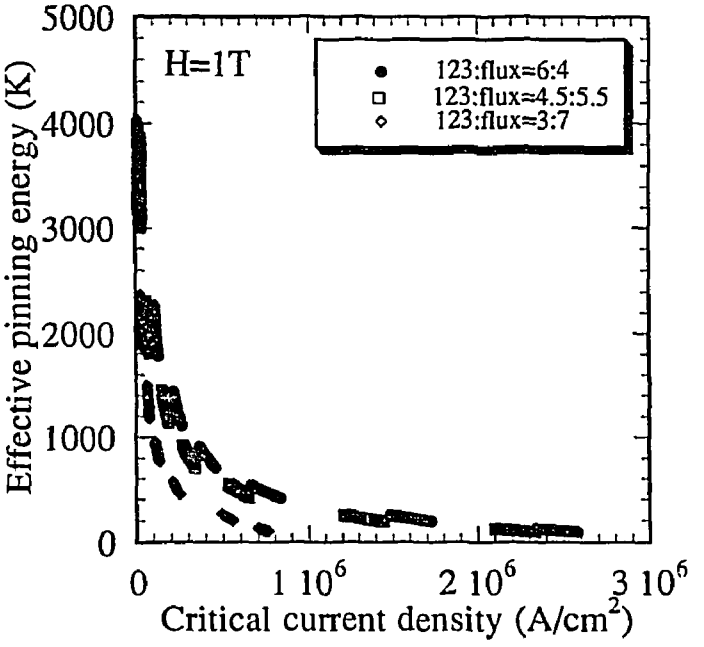

Fig. 4-8. The effective pinning energy as a function of the critical current densities of the three kinds of $YBa_2Cu_3O_x$ single crystals which were grown from the mixtures whose compositional ratios of the solid 1/6 (123) to the melt 1/25 ($7BaCuO_2 \cdot 11CuO$) were 3:7, 4.5:5.5 and 6:4. Magnetic field of 1 T was applied along the *c*-axis.

Chapter 5. Effect of Twin Boundaries on Flux Pinning in $YBa_2Cu_3O_x$ Single Crystals

5.1 Introduction

Flux pinning in high-temperature superconductors is important both for fundamental studies of superconductivity and for practical applications where the superconductor must carry high electric currents in the presence of high magnetic field. The increase in current is associated with the presence of various crystalline imperfections such as point defect,[31,32] dislocation,[33] twin boundary[34-44] and grain boundary.[32,45] In particular, the effect of twin boundaries on the critical current density (J_c) has been studied using various techniques: magneto-optical flux visualization,[34,35] Bitter decoration,[36,37] resistivity,[38,39] magnetization[40-42] and torque.[43,44] These experimental studies mentioned directly indicated the importance of twins for pinning. However, there are difficulties for correct determining the relatively small contribution of twin boundaries to J_c, because well-defined twin free crystals were very difficult to obtain. The contamination of impure cations with a different ionic radius and valence from containers during growth has a great influence on microstrains near twin boundaries.[46] The detwinning processes in $YBa_2Cu_3O_x$ (123) single crystals were carried out by applying uniaxial stress at a temperature up to 600°C.[47-51] However the detwinned crystals were twinned again when the oxygen annealing was performed without uniaxial stress. Therefore, it is difficult to obtain perfectly detwinned crystals which were fully oxidized. When the J_c measurements are done in the twinned and detwinned crystals, there is always the possibility of variations in the density of both twin boundaries remaining and other defects, such as impure cations and oxygen vacancies. These defects can mask the

contribution of the twin boundaries.

In the present experiment, we succeeded in separating the effect of the twin boundaries from that of other defects using magnetic studies in densely twinned and perfectly detwinned domains in the same 123 single crystal. The thermomechanical detwinning of the crystals was performed successfully under inert atmoshere, which is effective for keeping detwinned state perfectly even after oxygen annealing was conducted. The use of the Y_2O_3-crucible which is expected to be free from the contamination of impure metals from containers during growth was found to result in the production of crystals with the highest purity. The sharp superconductive transitions at T_c which guarantees the crystal quality were nearly the same in the both samples, indicating the concentration of point defect being the same magnitude with low values. Here, we describe the effect of the twin boundaries to J_c studied over a wide range of temperatures and magnetic fields.

5.2 Experimental

5.2.1 Thermomechanical detwinning

The 123 single crystals were grown from the coexisting region of the solid 211 with melt, according to the same method as that described in Section 2.2.2. The single crystal obtained was placed between a movable and fixed plate of the detwinned device as shown in Fig. 5-1. The uniaxial compressive stress along $a(b)$ axis was applied through the movable plate at 550°C under argon or air atmosphere. The detwinning process was observed *in situ* under polarized optical microscopy.

Oxygen annealing was performed at 550°C for 7 days under 5 atm so as to increase the oxygen content in the detwinned crystals. The content of

the oxygen was determined by an iodometric titration under argon atmosphere. The unit cell parameter was determined by the X-ray powder diffraction (XPD) method using Cu Kα radiation with a graphite monochromator.

5.2.2 Magnetization

Measurements of the magnetization were made for a set of temperatures between 5 and 84 K, with an external field *H//c* using a SQUID magnetometer of Quantum Design model MPMS. External magnetic fields up to 5.5 T were used. Samples were cooled to a desired temperature in a zero magnetic field. A scan length of 3 cm providing a field uniformity of ≤0.05% during measurement was used. A target temperature was stabilized to within ±0.05 K.

5.3 Results and discussion

5.3.1 Interaction between twin boundaries and crystal imperfections

The uniaxial compressive stress along the *a* (*b*)-axis was applied through the movable plate at 550°C in air, and the detwinning occurred rapidly into a complete single domain. However, when the applied stress was released at this temperature, a domain structure of nearly the same pattern as before reappeared again. Similar phenomena have been observed also in other works.[48] Even though when the crystal was cooled under load so as to prevent it from returning to the twinned state, the twinning structure came back during annealing for oxidation. These results suggest an existence of a strong interaction between the twin boundaries and crystalline

imperfections. The imperfections can be accumulated near the twin boundaries due to the strong mechanical microstrains. To determine how the deficit or extra oxygen atoms have an influence in such a phenomenon, the thermomechanical detwinning of 123 single crystals was conducted under an inert atmosphere before oxygen annealing. The sample was heated in air at 6°C/h and uniaxial stress was applied at 550°C. After the optical disappearance of the twin boundaries without the peripheral part of the crystal, the air atmosphere is changed to argon. The 123 crystals transformed from the orthorhombic to the tetragonal phase, and a single domain was observed throughout the whole crystal area. The temperature was maintained enough for the concentration of imperfections caused by oxygen atoms to be homogeneous. Finally, the atmosphere was changed to air so as to transform the 123 crystal into the orthorhombic phase. After a sufficient enough time for the transformation to be completed, the sample was cooled to room temperature at a rate of about 50°C/h.

An oxygen annealed 123 crystal before and after the detwinning is shown in Figs. 5-2 and 5-3. The images are optical micrographs taken with polarized visible light in a reflect mode. Twin boundaries were observed along the <1 1 0> direction in the whole area and in the corner before and after the detwinned crystals, respectively, which are characteristic of the crystals in the orthorhombic phase. The oxygen content of both annealed crystals was x=7.00 with lattice parameters of a=0.3819 nm, b=0.3890 nm, and c=1.168 nm. The directions of the a and b axes were determined as bisectors of the angle between the adjacent twin boundaries, 91.1 and 88.9 degrees, respectively, as shown in Fig. 5-4. We successfully divided into densely twinned and perfectly detwinned domains in the same crystal by cutting the corners approximately along the {1 0 0} planes using a wire saw. The complete detwinning was confirmed using the polarized optical

microscopy and the reciprocal lattice image taken by an X-ray precession camera, as shown in Figs. 5-5 and 5-6. The twin structure was not restored in the detwinned domain after oxygen annealing. The present thermomechanical detwinning under inert atmosphere is thought to be allow for a homogeneity in distribution of the imperfections caused by the oxygen atoms which would be accumulated near the twin boundaries. These results suggest a possibility of a strong interaction between the boundaries and crystalline imperfections caused by the oxygen atoms.

5.3.2 Magnetization

The quality of single crystal specimens is normally evaluated by χ-T curves.[67,68] As shown in Fig. 5-7, a sufficient shielding effect in a field of 1.0×10^{-3}T was observed as regards both the sharpness of the transition at T_c and the required value of the diamagnetism at low temperature below T_c guaranteeing the high quality of twinned and detwinned crystals which are homogeneous in oxygen content. The Meissner fractions decreased in twinned crystal which implies the existence of a strong flux pinning force.

Figure 5-8 shows the hysteresis loops measured in the temperature range 5~84 K with $H//c$. The influence of the twin boundaries on the width of hysteresis loops (ΔM) was found to change with temperature. In the low temperature region, $T<20$ K, ΔM of the twinned crystal had a smaller value than that of the detwinned one. However, in the high-temperature region, $T>60$ K, ΔM of the twinned crystal provided larger than that of the detwinned crystal. These results implied that the presence of the twin boundaries brought about by a reduction of the flux pinning force in low temperature, but with an increase in temperature, the twin boundaries worked as strong pins. The drastic changes in the shape of the hysteresis loops were observed

in the intermediate temperature range T=20~60 K. Remarkable fishtail hysteresis loops were observed in the higher external field, especially in the detwinned crystal. However, in the high-temperature region, T>70 K, only a monotonic decrease in J_c with H was observed. These results shows that the fishtail effect originates from pinning by the point-like defects and the pinning force of the defects decreases as the temperature decreases.

J_c depends on both the width of the loop and the sample dimension according to the Bean model[70] as shown in Eq. (4.1). Figure 5-9 shows changes of J_c with the external field in the temperature range from 5~84 K with $H//c$. In the low temperature region, a quite large reduction in J_c could be observed in the twinned crystal, showing about a 1/2-times reduction at 5 K. In the high-temperature region, the irreversibility line shifted to the high magnetic field in the twinned crystal.

Figure 5-10 shows on the semilogarithmic plot of J_c with temperature in the field range 1~4 T. An approximately exponential decrease of J_c with T is observed for T<50 K, and followed by a more sharp reduction at higher temperatures. This is consistent with many earlier reports.[72,73] The key observation about these data shows that there is a large reduction in J_c in the twinned crystal and the changing exponential decrease of J_c with T in the detwinned crystal are apparent from a steep slope to a gentle one with an increase in the field at T<50 K.

Theoretical studies still can not decided whether the twin boundaries form regions with a decreased[78-80] or increased[81,82] value for the superconducting order parameter. Suggestions have been made that in case of a decreased order parameter in the twin boundaries, channeling of the vortices along the twin boundaries takes place. The observation of reducing the flux pinning force in the twinned crystal at the low temperature region, supports the fact that the twin boundaries give rise to a guide a vortex

motion.[34,83] With increasing temperature, the pinning force along the twin boundaries is enhanced as compared with the other crystalline imperfections such as point defect.[84]

5.4 Summary

We succeeded in separating the effect of the twin boundaries from that of other defects in the magnetic studies using densely twinned and perfectly detwinned domains in the same 123 single crystal, where the twinned and detwinned parts which were free from the contamination of impure metals from containers, had the same homogeneity in oxygen content, x=7.00. The most successful detwinning of the 123 crystals was a thermomechanical treatment under inert atmoshere, which kept the perfectly detwinned domain after oxygen annealing. The influence of the twin boundaries on J_c strongly depended on temperature. At low temperatures, the twinned domain showed a smaller J_c than that of the detwinned one. However, as the temperature increased, the twin boundaries worked as being strong pins and the twinned domain showed a larger J_c than that of the detwinned one. Remarkable fishtail hysteresis loops were observed, especially in the detwinned crystal.

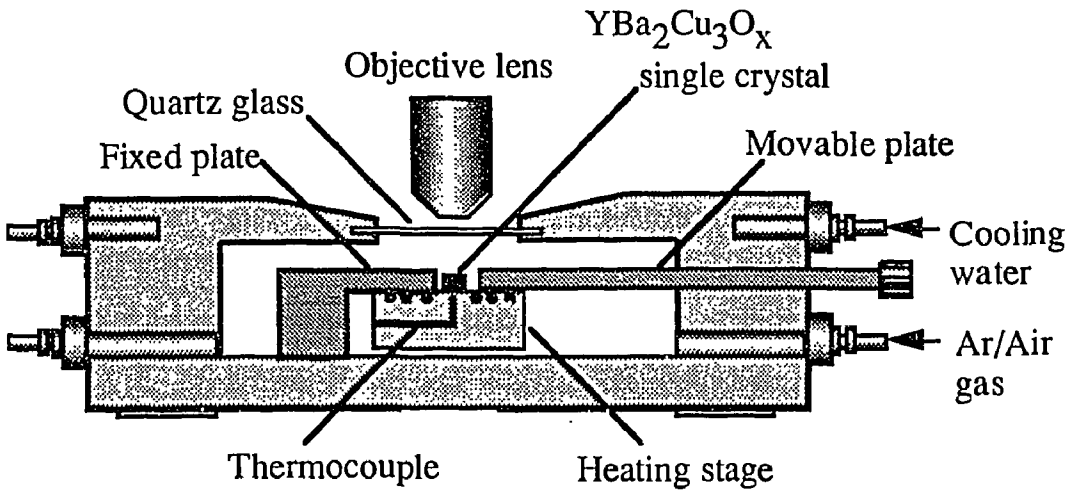

Fig. 5-1. Device for thermomechanical detwinning of $YBa_2Cu_3O_x$ single crystal.

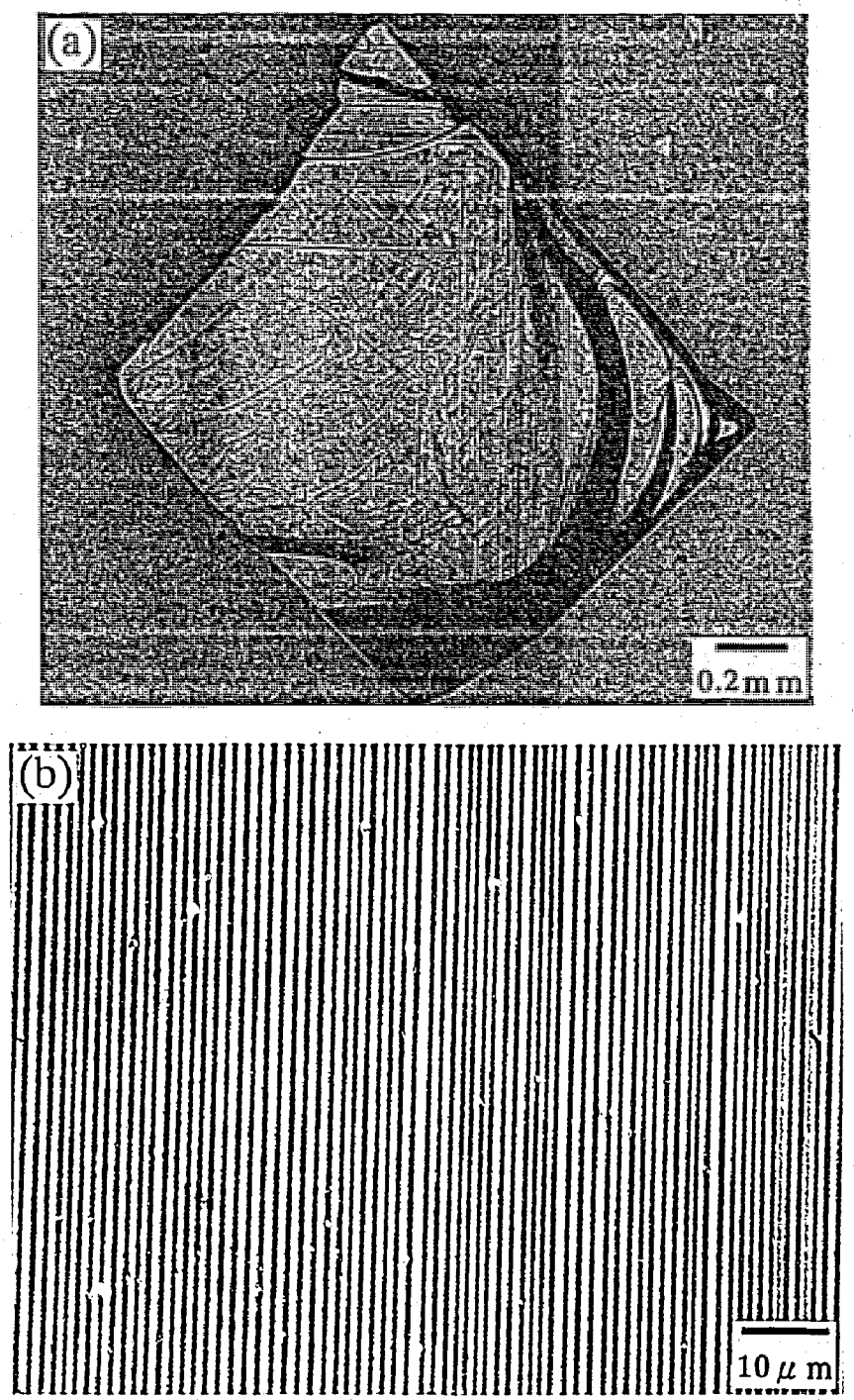

Fig. 5-2. Polarized optical micrographs of (a) an oxygen annealed $YBa_2Cu_3O_x$ single crystal before the detwinning treatment and (b) its magnification of twinned domain.

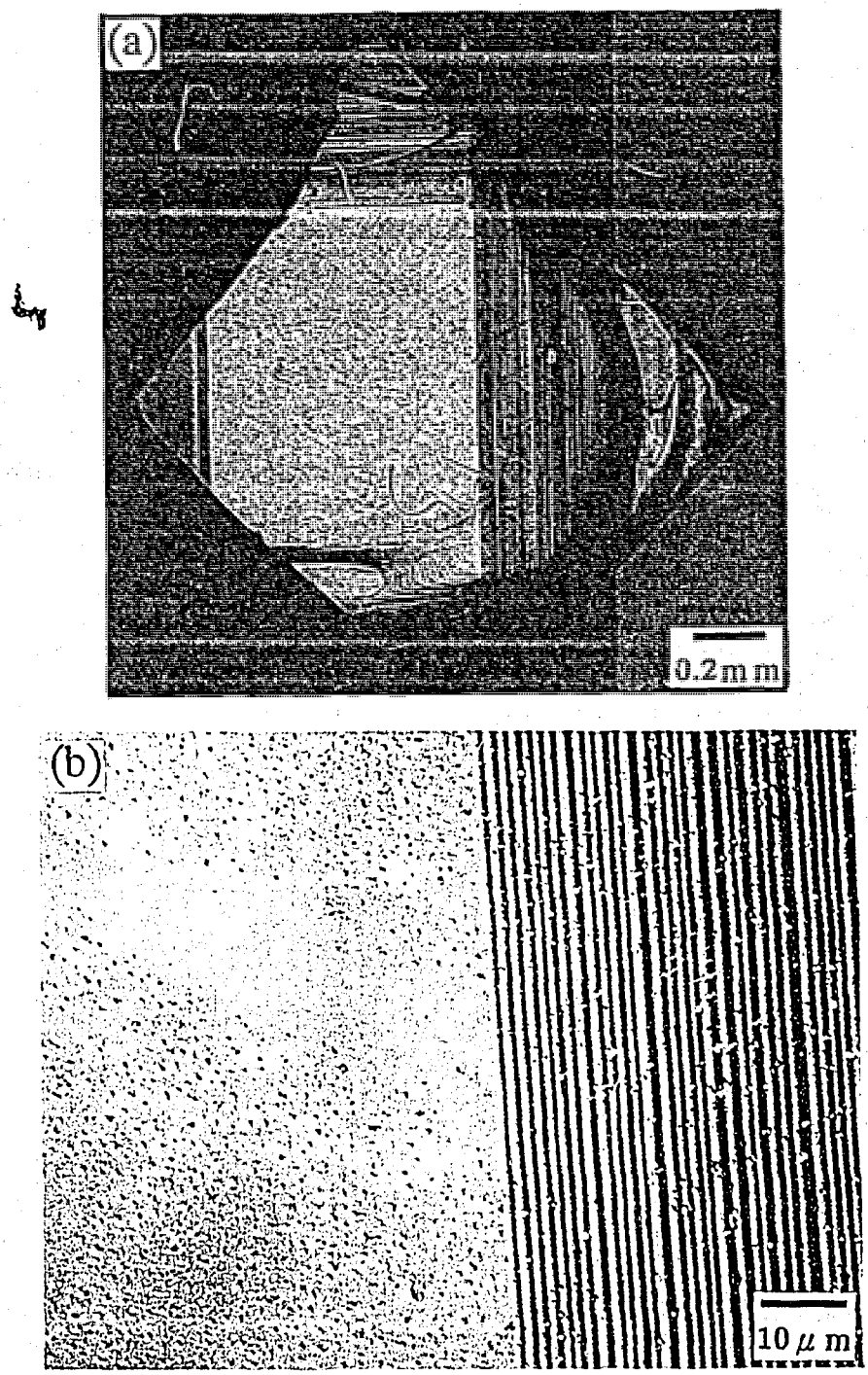

Fig. 5-3. Polarized optical micrographs of (a) an oxygen annealed $YBa_2Cu_3O_x$ single crystal after the detwinning treatment and (b) its magnification of the boundary between twinned and perfectly detwinned domain.

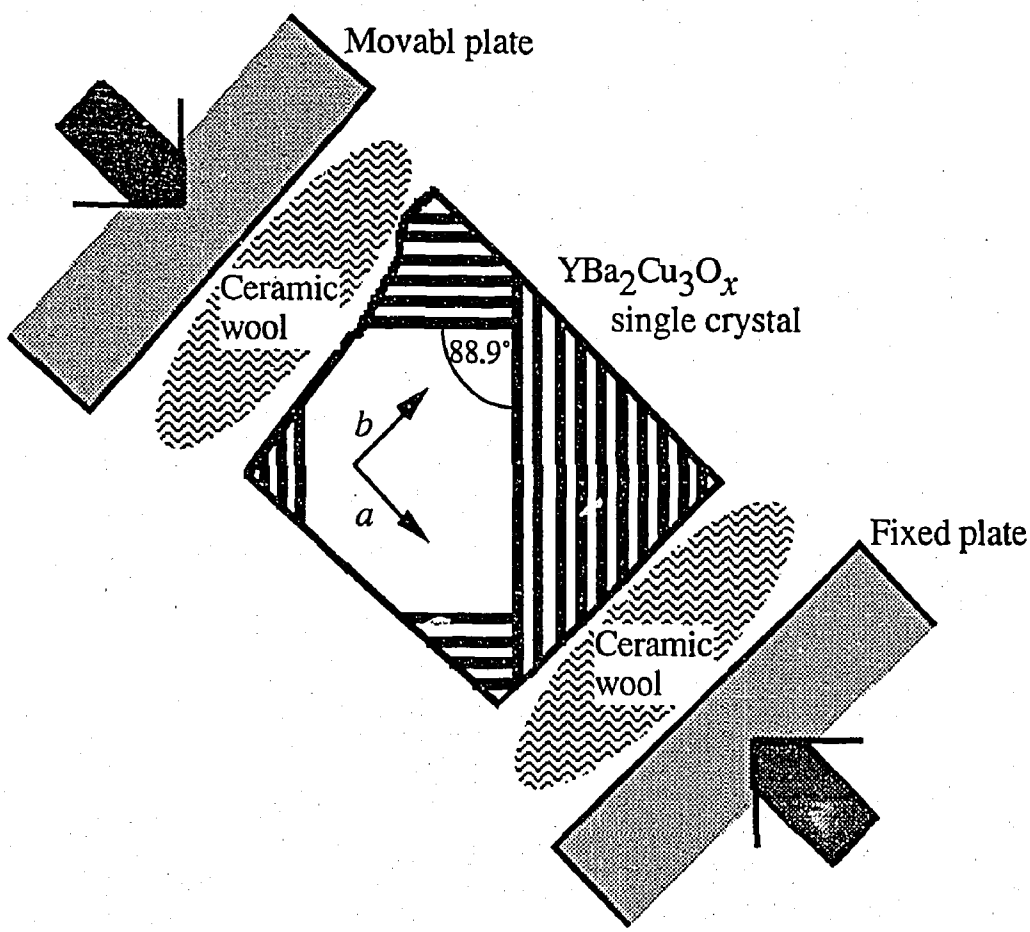

Fig. 5-4. Relationship between the directions of the uniaxial compressive stress and the crystallographic axis which were determined as the bisectors of the angle between adjacent twin boundaries.

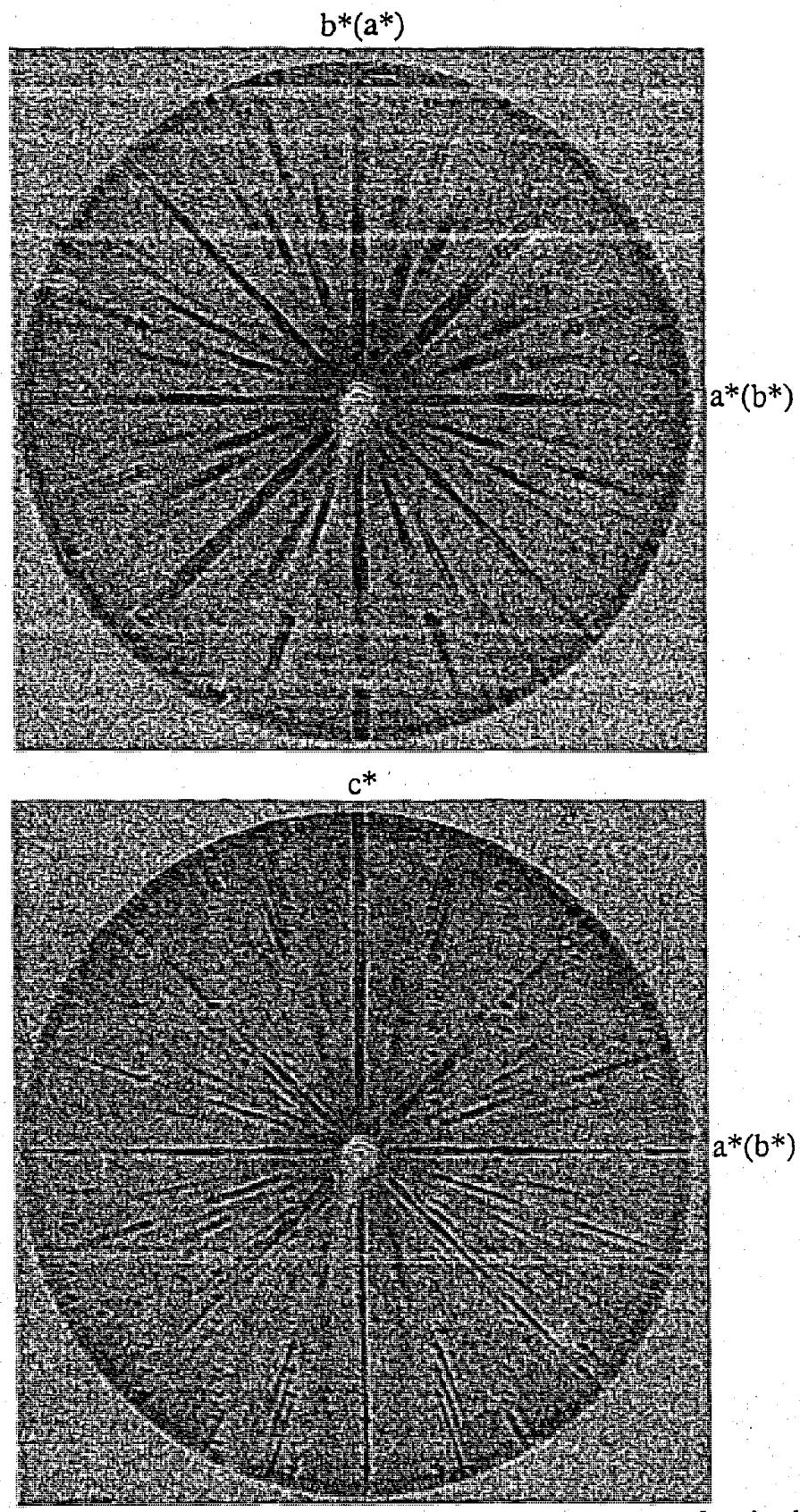

Fig. 5-5. X-ray precession photographs of a twinned $YBa_2Cu_3O_x$ single crystal on the (a) (*h k 0*) and (b) (*0 k l*) plane.

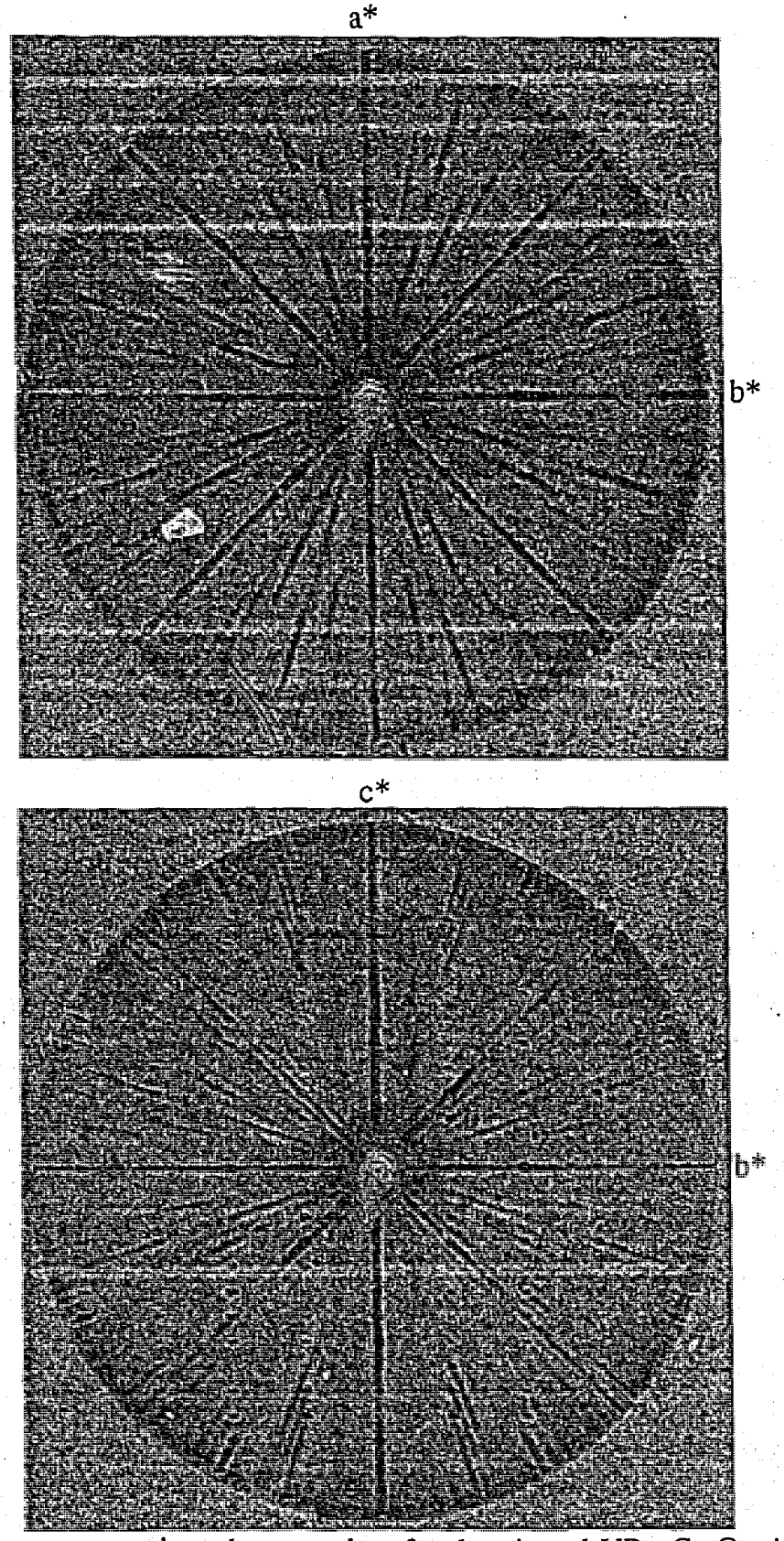

Fig. 5-6. X-ray precession photographs of a detwinned $YBa_2Cu_3O_x$ single crystal on the (a) (*h k 0*) and (b) (*0 k l*) plane.

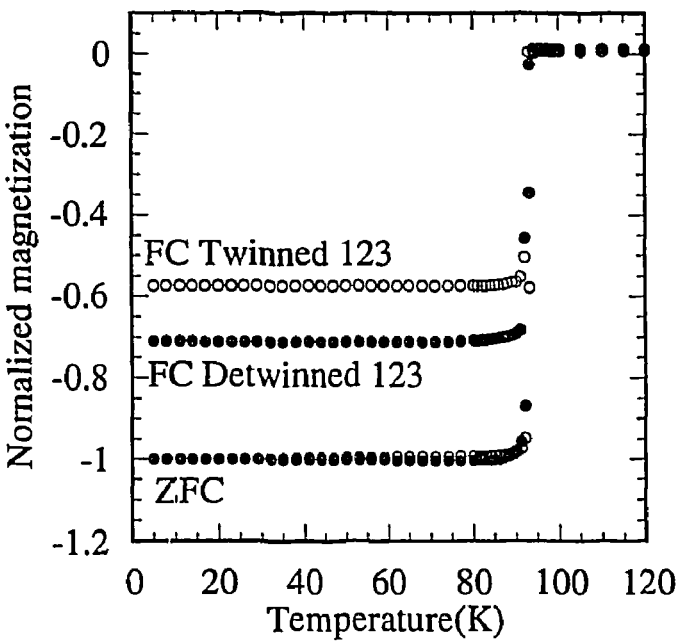

Fig. 5-7. Zero-field-cooled (ZFC) and field-cooled (FC) susceptibility of a twinned and a detwinned $YBa_2Cu_3O_x$ single crystal after oxygen annealing. Magnetic field of 1.0×10^{-3} T was applied along the *c*-axis.

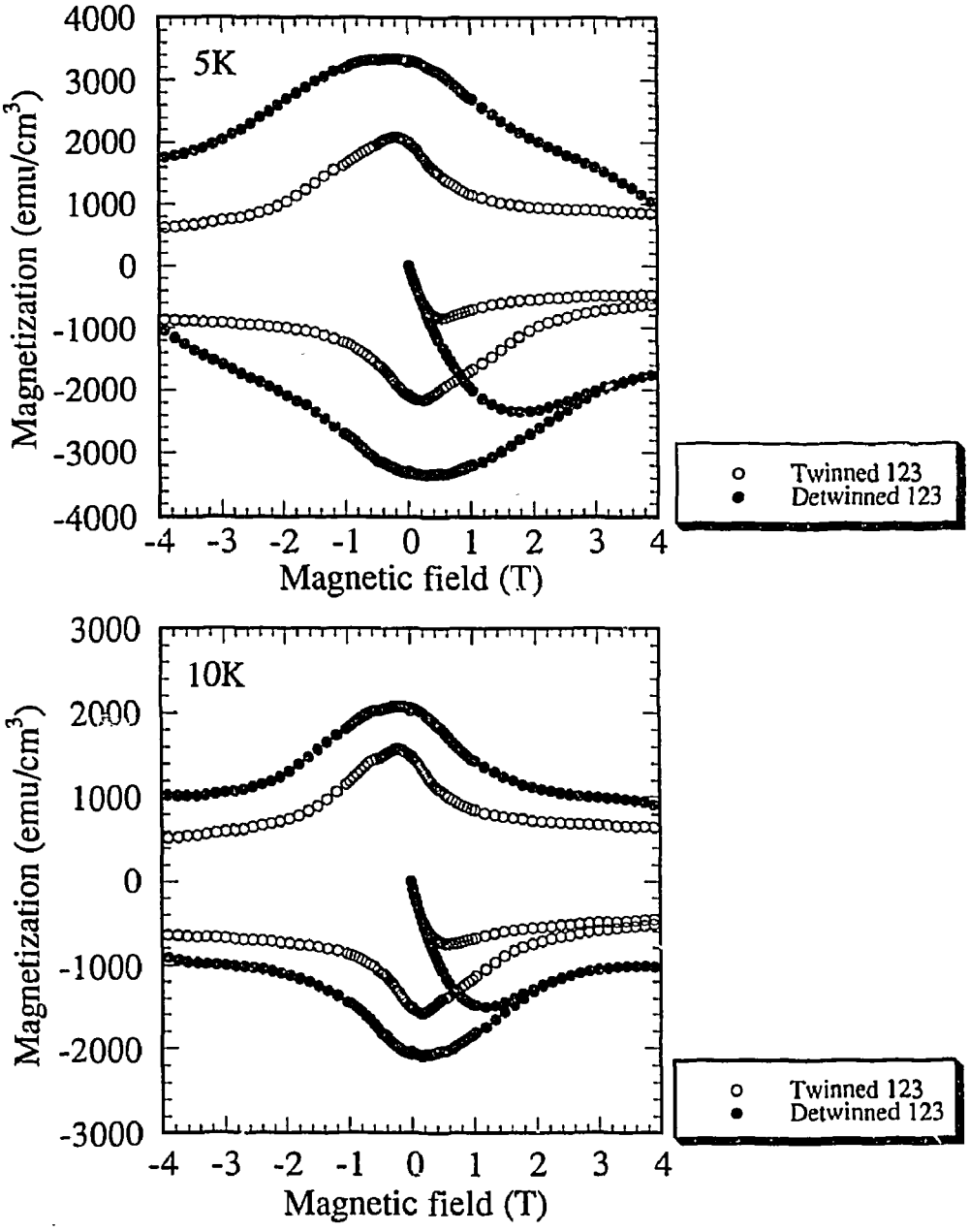

Fig. 5-8. Magnetization hysteresis loops of a twinned and a detwinned $YBa_2Cu_3O_x$ single crystal after oxygen annealing. Magnetic fields up to 5.5 T were applied along the *c*-axis in the temperature range from 5~84 K.

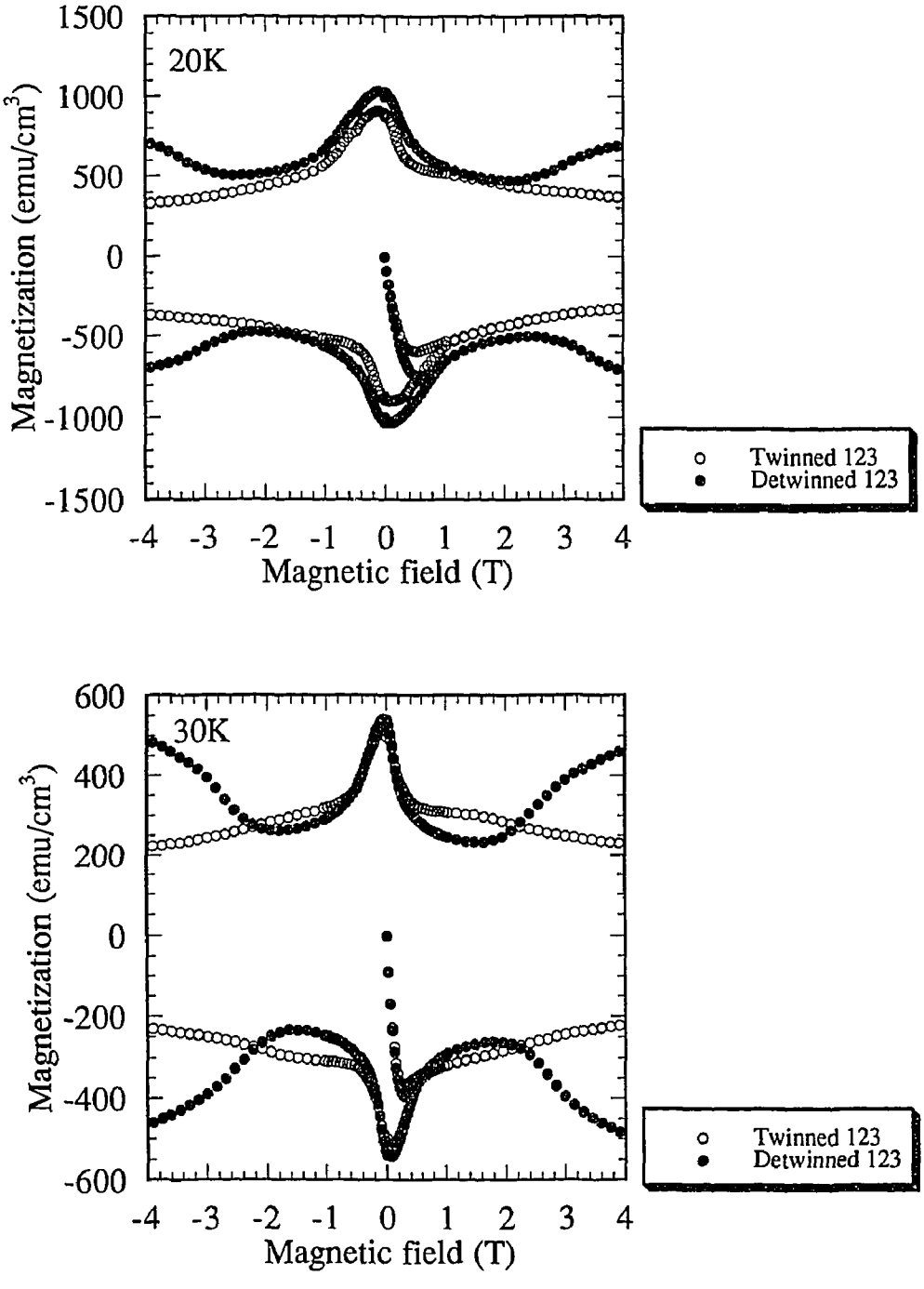

Fig. 5-8. (continued)

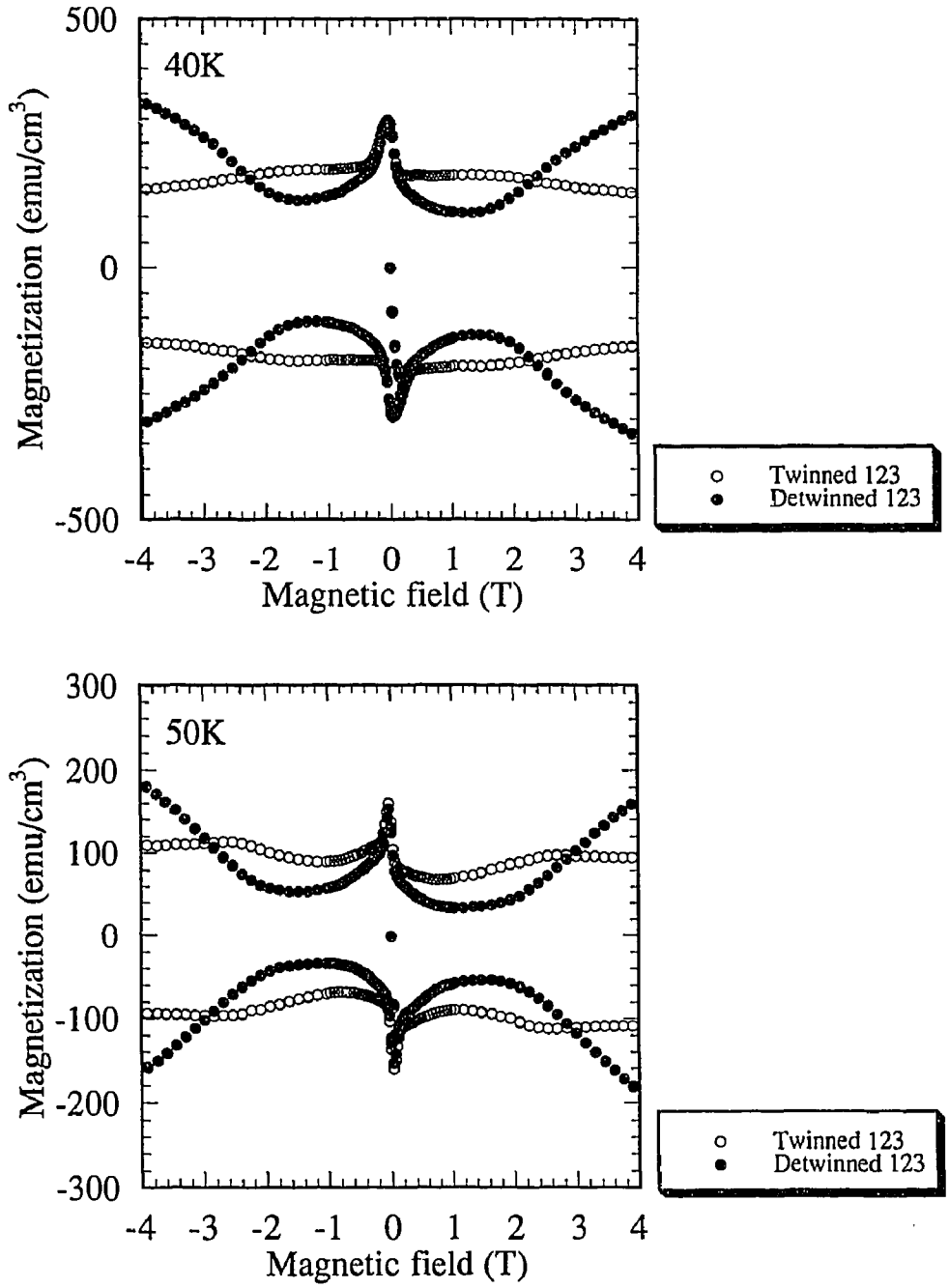

Fig. 5-8. (continued)

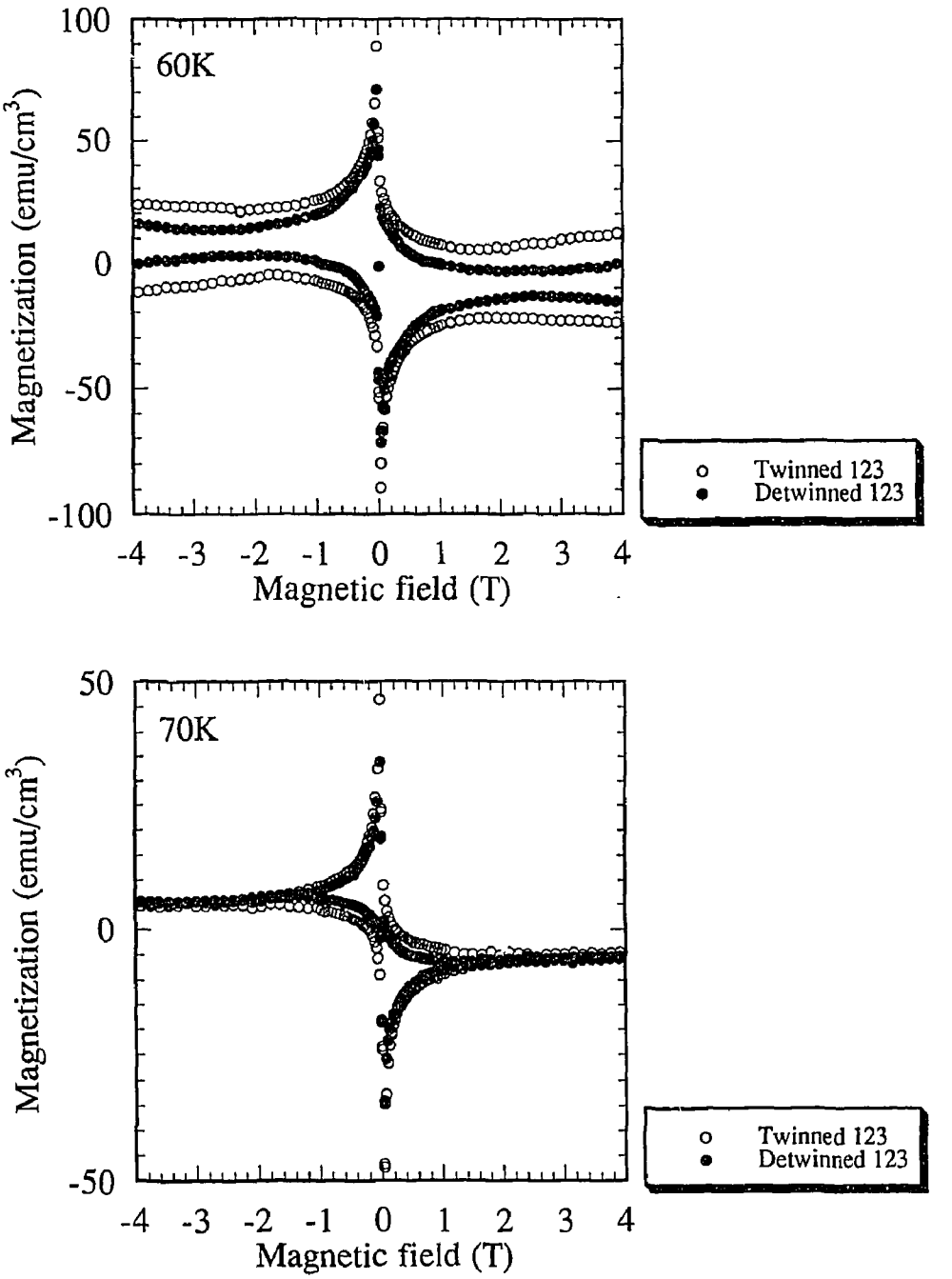

Fig. 5-8. (continued)

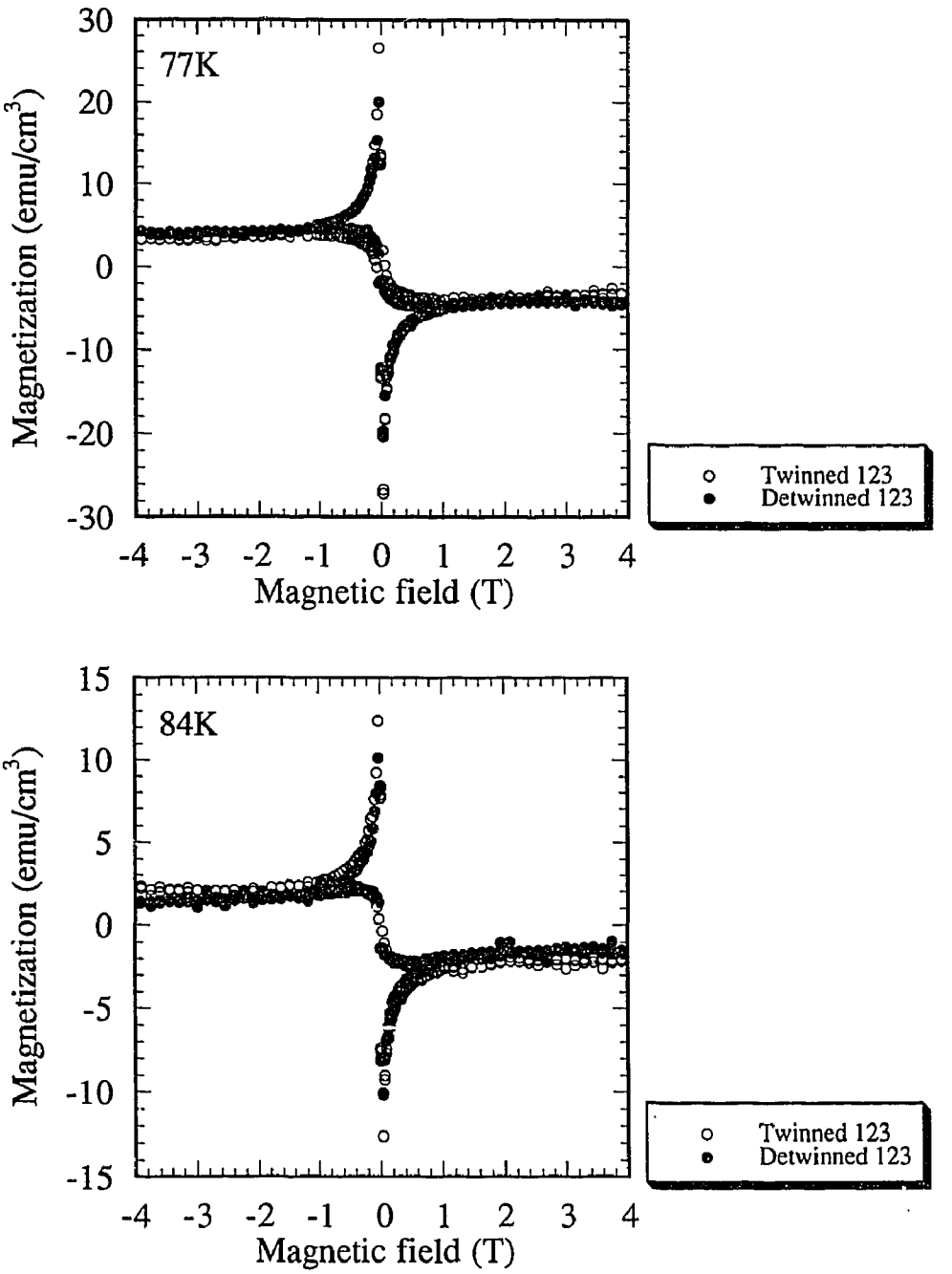

Fig. 5-8. (continued)

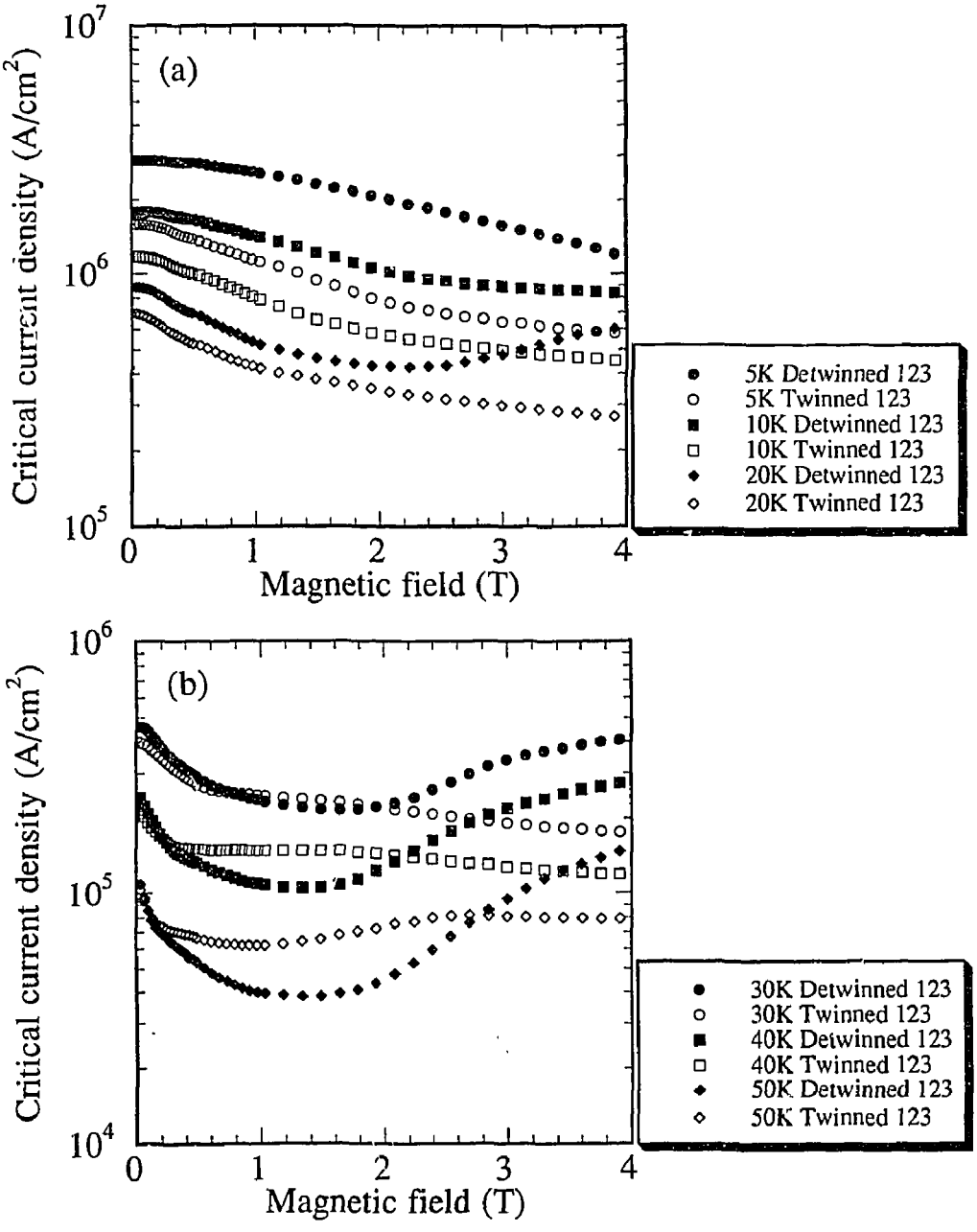

Fig. 5-9. Field dependence of the critical current densities of a twinned and a detwinned $YBa_2Cu_3O_x$ single crystal after oxygen annealing. Magnetic fields up to 5.5 T were applied along the *c*-axis in the temperature range (a) 5~20 K, (b) 30~50 K and (c) 60~84 K.

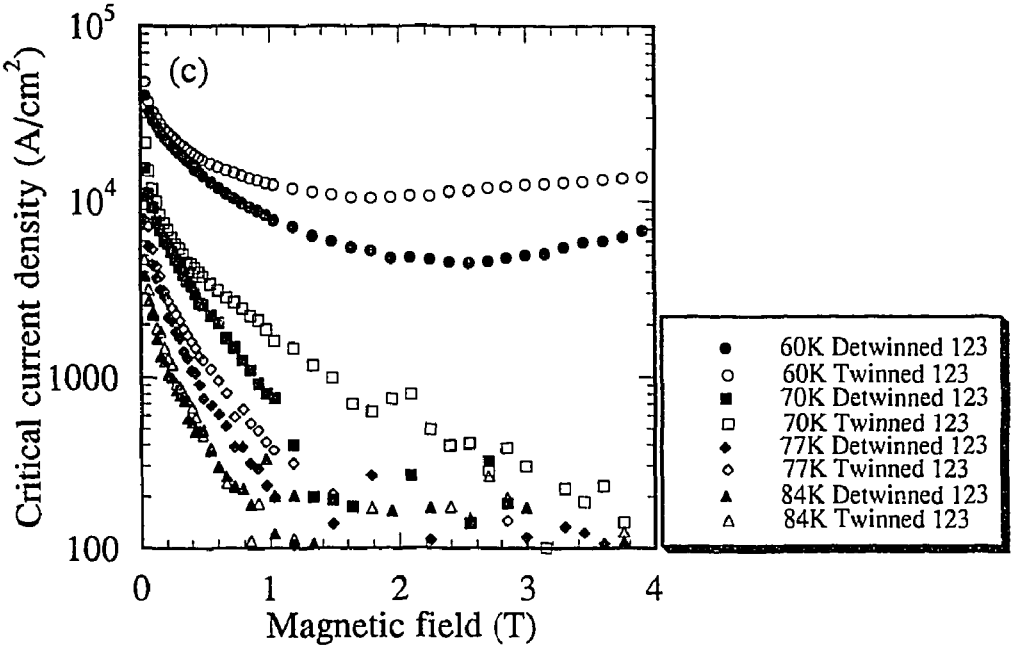

Fig. 5-9. (continued)

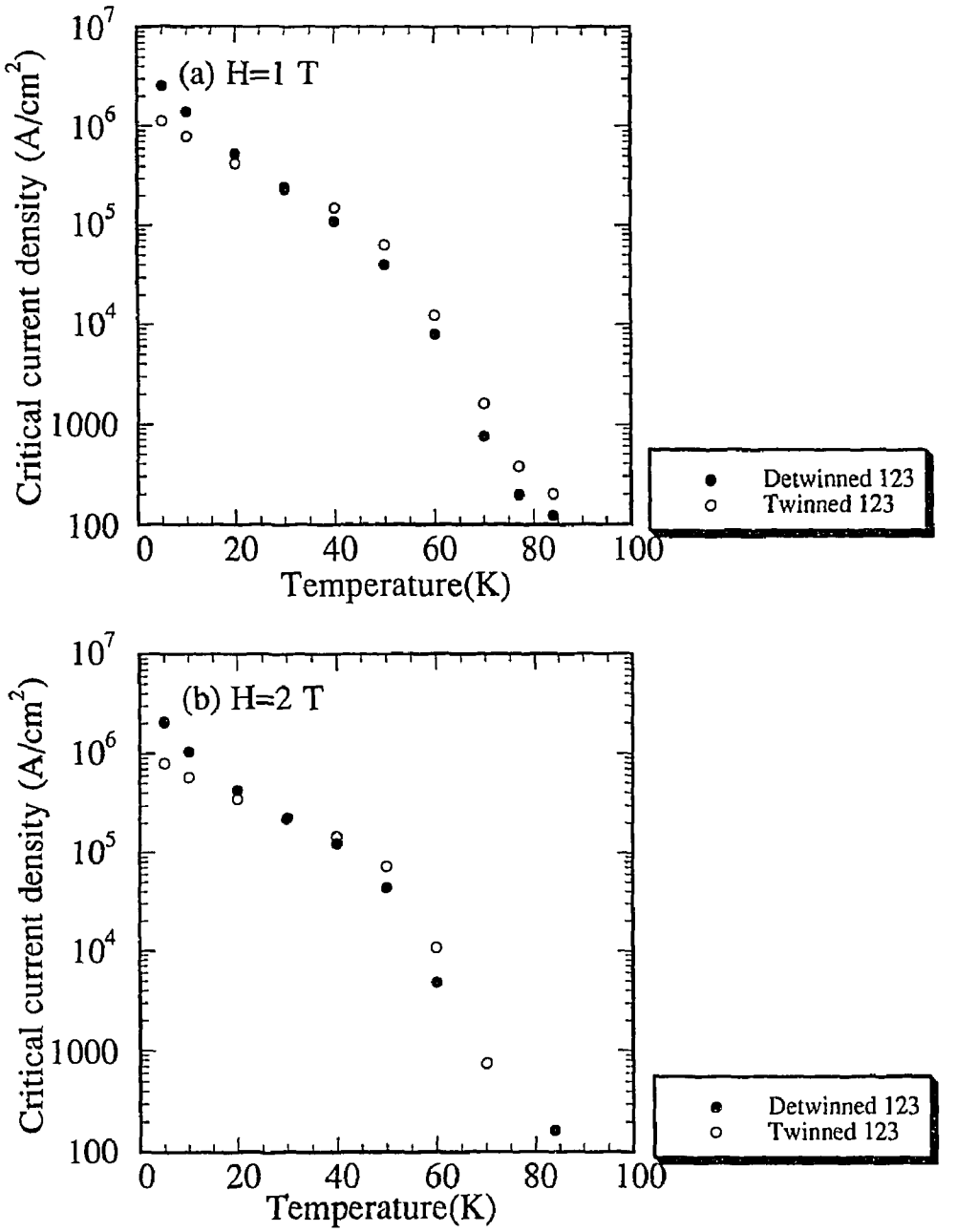

Fig. 5-10. Temperature dependence of the critical current densities of a twinned and a detwinned $YBa_2Cu_3O_x$ single crystal after oxygen annealing. Magnetic fields of (a) 1 T, (b) 2 T, (c) 3 T and (d) 4 T were applied along the *c*-axis.

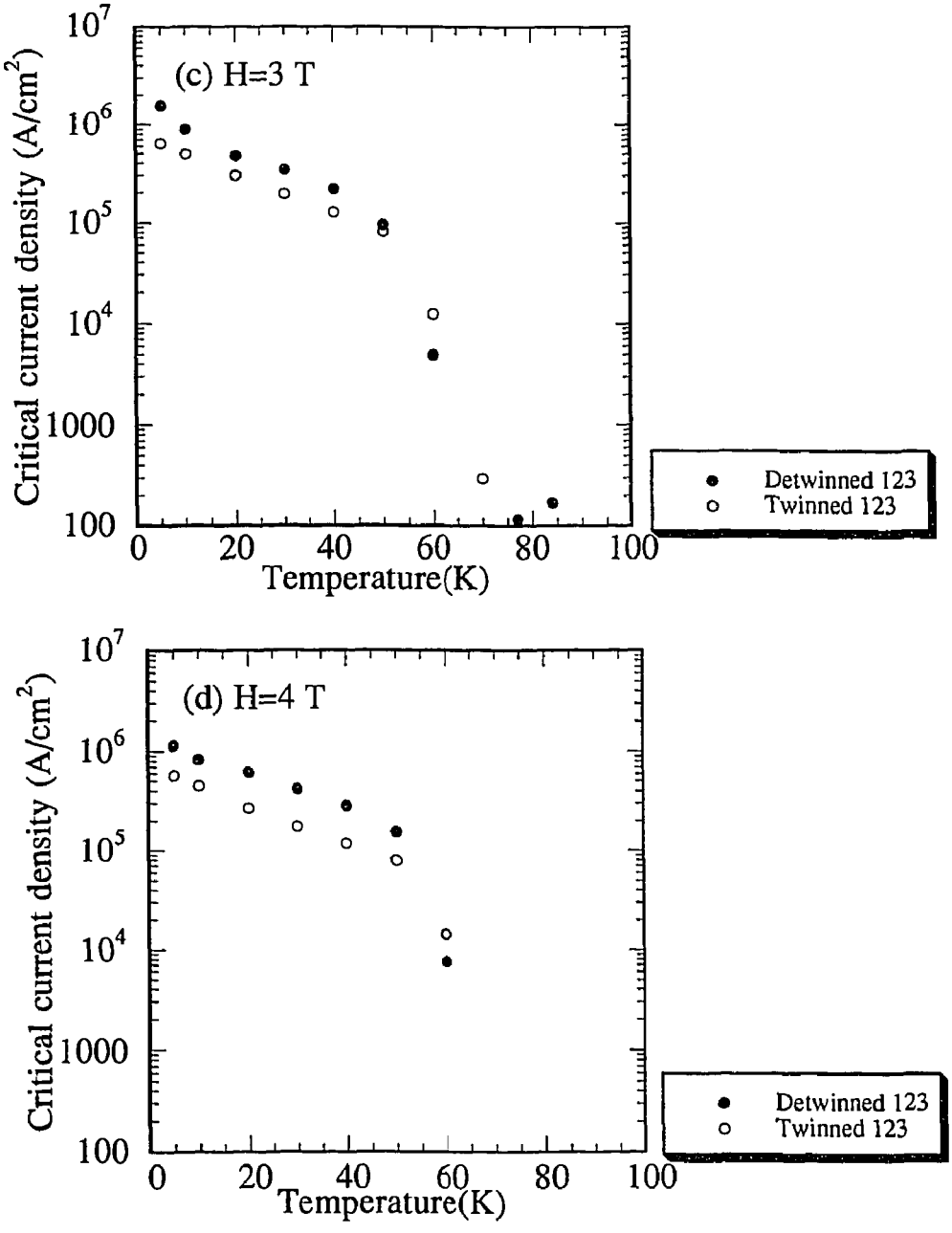

Fig. 5-10. (continued)

Chapter 6. Conclusion

Large isometric single crystals of the oxide superconductor $YBa_2Cu_3O_x$ (123) were grown from a mixed region of the solid Y_2BaCuO_5 (211) and melt. The crystals possessed sharp, shiny habits with a maximum thickness of about 7 mm along the *c*-axis. The best growth conditions were determined for obtaining large single crystals, where the solvent composition was $7BaCuO_2$-11CuO which is close to the binary eutectic of $BaCuO_2$-CuO, and the optimum concentration of the growth system was in the ratio of 1/6 (123) to 1/25 ($7BaCuO_2$•11CuO) of 3:7. The use of a Y_2O_3-crucible prevented contamination from the containers during growth, and facilitated the synthesis of high-purity crystals. The appropriate temperature gradient and the use of seed crystals were both effective for controlling nucleation.

The oxygen-annealed crystals showed a sharp superconductive transition at 91 K. The temperature dependence of the resistivities was found to be metallic both in the *a* (*b*)- and *c*-direction, and was very different from those of other oxide superconductors such as $La_{2-x}Sr_xCuO_4$ and $Bi_2Sr_2CaCu_2O_x$. Sufficient shielding was observed in both the sharpness of the transition at T_c and the required value of the diamagnetism at low temperatures below T_c.

Marked anisotropy was observed in the transition region in the resistivity (ρ)-temperature (T) curve under the applied magnetic field parallel or perpendicular to the *c*-axis. It become clear that the transition width depended not on the direction of transport current but on the direction of the applied magnetic field. A remarkable broadening of the resistive transition was observed when the magnetic field was applied perpendicular to the CuO_2 plane. These phenomena should be interpreted in terms of some anisotropic factor without any Lorentz force, as those obtained in $La_{2-x}Sr_xCuO_4$ single

crystals.

The crystal growth mechanism of 123 from a mixed region of the solid 211 and the melt was investigated regarding the quenched samples between 1050 and 900°C using a polarizing optical microscope, an EPMA, and a X-ray powder diffraction method. The observations suggested the solubility of the 123 phase to the melt, and induction of Ostwald ripening, which acts on the solid-melt interfaces to lower the interface free energy of the growing crystals. These lead to the growth of 123 crystals which progressed due to the peritectic reaction between the 211 and the surrounding melt phase.

We focused on the relationship between J_c and crystalline imperfections using the 123 single crystals which were grown from the mixtures whose compositional ratios of the solid 1/6 (123) to the melt 1/25 ($7BaCuO_2 \cdot 11CuO$) were 3:7, 4.5:5.5 and 6:4. In the cross section of the three 123 crystals, the number of voids increased with a decrease in the melt composition. Sufficient shielding in the field was observed in both the sharpness of the transition at T_c and the required value of the diamagnetism at low temperatures below T_c, guaranteeing the high quality of the three crystals synthesized uniformly as the 123 phase. As the ratios of the melt composition decreased, the Meissner fractions, the electro-magnetic current density and the effective pinning energy were enhanced relatively, which showed there was a strong flux pinning force.

The effect of the twin boundaries on J_c was studied using densely twinned and perfectly detwinned domains in the same 123 single crystal. The high quality of the twinned and detwinned crystals which were free from the contamination of impure metals from containers, had the same homogeneity in oxygen content, x=7.00. The thermomechanical detwinning of the 123 crystals was successfully developed under inert atmoshere, which kept a perfectly detwinned domain after oxygen annealing. The influence

of the twin boundaries on J_c strongly depended on temperature. At low temperatures, the twinned domain showed a smaller J_c than that of the detwinned one. However, as increase in temperature, the twin boundaries worked as strong pins and the twinned domain showed a larger J_c than that of the detwinned one. Remarkable fishtail hysteresis loops were observed, especially in the detwinned crystal.

Acknowledgments

The author would like to express his sincere gratitude to Prof. H. Takei of the Institute for Solid State Physics (ISSP), the University of Tokyo, for his valuable suggestions and heartful encouragement throughout this investigation. He is also grateful to Dr. Y. Kazumata of the Japan Atomic Energy Research Institute (JAERI), for his helpful advice and measurements of the magnetic properties, Dr. H. Ohno and Dr. K. Noda of JAERI for their enthusiastic encouragement and support.

He is also indebted to Prof. Y. Iye of ISSP and Prof. T. Tamegai of Department of Applied Physics, the University of Tokyo, for the advice and help during the measurements of the electrical properties, Prof. M. Kinoshita of the Science University of Tokyo, Yamaguch College and Prof. M. Tamura of the Department of Physics, Toho University, for measurements of the magnetic properties and Prof. T. Ishida of the Department of Physics and Electronics, University of Osaka Prefecture, for his interesting suggestions and encouragement. He would like to express the deepest gratitude to Dr. H. Maeda of JAERI for help in the structural analysis, Messrs. H. Nakajima, K. Ikenoya and Dr. K. Onuki of JAERI, for the chemical analysis and Dr. Y. Katano, Messrs. K. Fukai, K. Fujii and J. Nakano of JAERI, for carrying out the observation of the crystals using TEM and SEM-EPMA. Hearty thanks are also given to Dr. H. Takeya of the National Research Institute for Metal and Dr. M. Hasegawa of ISSP for their advice, Mrs. F. Sakai of ISSP for the chemical analysis and Mr. M. Koike of ISSP for his kind help to take care of all the equipment.

Finally, special thanks is needed for all the members of the Material Innovation Laboratory of JAERI who he has been working with.

References

1) J. B. Bednorz and K. A. Muller: Z.Phys. B **64** (1986)189.
2) S. Uchida, H. Takagi, K. Kitazawa, and S. Tanaka: Jpn. J. Appl.Phys. **26** (1987) L1.
3) M. K. Wu, J. R. Ashburn, C. J. Torng, O. H. Hor, R. L. Meng, Z. J. Huang, Y. Q. Wang and C. W. Chu: Phys. Rev. Lett. **58** (1987) 908.
4) H. Maeda, Y. Tanaka, M. Fukutomi and T. Asano: Jpn. J. Appl.Phys. **27** (1988) L209.
5) S. S. P. Parken, V. Y. Lee E. M. Engler, A. I. Nazzaal, T. C. Huang, G. Gorman, R. Savoy and R. Beyers: Phys. Rev. Lett. **60** (1988) 2539.
6) A. Schiling, M. Cantoni, J. D.Guo and H. R. Ott: Nature **363** (1993) 56.
7) R. J. Cava, B. Batlogg, R. B. van Dover, D. W. Murphy, S. Sunshine, T. Siegrist, J. P. Remeika, E. A. Reitman, S. M. Zahurak and G. P. Espinosa: Phys. Rev. Lett. **58** (1987) 1676.
8) Y. Sayono, M. Kikuch, K. Oh-ishi, K. Hiraga, H. Arai, Y. Matui, N. Kobayashi, S. Tomioka, F. Izumi and K. Inoue: Jpn. J. Appl. Phys. **26** (1987) L498.
9) M. A. Beno, L. S.oderholm, D. W. Capone Ⅱ, D. G. Hinks, J. D. Jorgensen, J. D. Grace, I. K. Schuller and K. Zhang: Appl. Phys. Lett. **51** (1987) 57.
10) F. Izumi, H. Asano, T. Ishigaki, E. Takayama-Muromach, Y. Uchda, N. Watanabe and T. Nishikawa: Jpn. J. Appl. Phys. **26** (1987) L649.
11) W. I. F. David, W. T. A. Harrison, J. M. F. Gunn, O. Mose, A. K. Soper, P. Day, J. D. Jorgensen, D. G. Hinks, M. A. Beno, L. Soderholm, D. W. Capone Ⅱ, I. K. Schuller, C. U. Segre, K. Zhang and J. D. Grace: Nature **327** (1987) 310.

12) R. J. Cava, B. Batlogg, C. H. Chen, E. A. Reitman, S. M. Zahurak and D. Werder: Nature **329** (1987) 423.

13) H. Oyanagi, H. Ihara, T. Matubara, M. Tokumoto, T. Matushita, M. Hirabayashi, K. Murata, T. Yao, H. Iwasaki and Y. Kimura: Jpn. J. Appl. Phys. **26** (1987) L1561.

14) J. Z. Lui, G. W. Crabtree, A. Umezawa and Li Zongquan:Phys. Lett. A **121** (1987) 305.

15) A. Ono and T. Tanaka: Jpn. J. Appl. Phys. **26** (1987) L825.

16) L. Er-Rakho, C. Michel, L. Provost and B. Raveau: J. Solid State Chem. **37** (1987) 151.

17) S. Takekawa and N. Iyi: Jpn. J. Appl. Phys. **26** (1987) L851.

18) T. R. Dinger, T. K. Worthington, W. J. Gallagher and R. L. Sandstorm: Phys. Rev. Lett. **58** (1987) 2687.

19) Y. Hidaka, Y. Enomoto, M. Suzuki, M, Oda, A. Katui and T. Murakami: Jpn. J. Appl. Phys. **26** (1987) L726.

20) D. L. Kaizer, F. Holtzberg, B. A. Scott and T. R. McGuire: Appl. Phys. Lett. **51** (1987) 1040.

21) L.F. Schneemeter, J. V. Waszczak, T. Seigrist, R. B. van Dover, L. W. Rupp, B. Batlogg, R. J. Cava and D. W. Murphy: Nature **328** (1987) 601.

22) D. L. Kaizer, F. Holtzberg, M. F. Chisholm and T. K. Worthington: J. Cryst. Growth **85** (1987) 593.

23) H. J. Sheel and F. Licci: J. Cryst. Growth **85** (1987) 607.

24) W. Sadowski and H. J. Sheel: J. Less-Common Metals **150** (1989) 219.

25) Th. Wolf, W. Goldacker and B. Obst: J. Cryst. Growth **96** (1989) 1010.

26) K. Schonmann, B. Seebacher and K. Andres: J. Less-Common Metals **164/165** (1990) 169.

27) S. W. Tozer, A. W. Kleinsasser, T. Penney, D. Kaisser and F. Holtzberg:

Phys. Rev. Lett. **59** (1987) 1768.

28) Y. Iye, T. Tamegai, H. Takeya and H. Takei: Jpn. J. Appl. Phys. **27** (1988) L658.

29) Y. Yeshrun and A. P. Malozemoff: Phys. Rev. Lett. **60** (1988) 2202

30) T. T. M. Palstra, B. Batlogg, L. F. Schneemeyer and J. V. Waszczak: Phys. Rev. Lett. **61** (1988) 1662.

31) E. M. Chudnovski: Phys. Rev. Lett. **65** (1990) 3060.

32) M. Daeumling, J. M. Seuntjens and D. C. Larbalestier: Nature **346** (1990) 332.

33) R. Wang, h. Ren, L. Xiao, Q. He, C. Wang and D. Yu: Supercond. Sci. Technol. **3** (1990)344.

34) C. A. Durán, P. L. Gammel, R. Wolfe, V. J. Fratello, D. J. Bishop, P. J. Rice and D. M. Ginsbrg: Nature **357** (1992) 474.

35) U. Welp, T. Gradiner, D. Gardiner, D. Gunter, J. Fendrich, G. W. Crabtree, V. K. Vlasko-Vlasov and V. I. Nikitenko: Pysica C **232-405** (1994) 241.

36) L. Ya. Vinnikov, L. A. Gurevich, G. A. Yamelchenko and Yu. A. Ossipyan: Solid State Commun. **67** (1988) 421.

37) G. J. Dolan, G. V. Chandrashekhar, T. R. Dinger, C. Field and F. Holtzberg: Phys. Rev. Lett. **62** (1989) 827.

38) U. Welp, W. K. Kwok, G. W. Crabtree, K. G. Vandervoort: Appl. Phys. Lett. **57** (1990) 84.

39) G. W. Crabtree, W. K. Kwok, U. Welp, J. Downey, S. Fleshler, K. G. Vandervoort, J. Z. Lui: Pysica C **185-189** (1991) 282.

40) L. J. Swartzendruber, A. Roitburd, D. L. Kaiser, F. W. Gayle and L.H. Bennett: Phys. Rev. Lett. **64** (1990) 483.

41) D. L. Kaiser, F. W. Gayle, L. J. Swartzendruber, L.H. Bennett and R. D. McMichael: J. Appl.Phys. **70** (1991) 5739.

42) J. Z. Liu, Y. X. Jia, R. N. Shelton and M. J. Fluss: Phys. Rev. Lett. **66** (1991) 1354.

43) R. Hergt, W. Andrä, K. Fischer, N. M. Tchebotaev and S. L. Town: Phys. Status Solidi A **119** (1990) 241.

44) E. M. Gyorgy, R. B. van Dover, L. F. Schneemeyer, A. E. White, H. M. O'Bryan, R. J. Felder, J. V. Waszczak, W. W. Rhodes and F. Hellman: Appl. Phys. Lett. **56** (1990) 2465.

45) D. F. Lee, V. Selvamanickam and K. Salama: Physica C **202** (1992) 83.

46) Y. Zhu, M. Suenaga, J. Tafto and D. O. Welch: Phys. Rev. B **44** (1991) 2871.

47) T. Hatanaka and A. Sawada: Jpn. J. Appl. Phys. **28** (1989) L794.

48) D. L. Kaiser, F. W. Gayle, R. S. Roth and L. J. Swartzendruber: J. Mater. Res. **4** (1989) 745.

49) U. Welp, M. Grimsditch, H. You, W. K. Kwok, M. M. Fang, G. W. Crabtree and J. Z. Liu: Pysica C **161** (1989) 1.

50) R. Gagnon, C. Lupien and L. Taillefer: Phys. Rev. B **50** (1994) 3458.

51) M. Oussena, P. A. J. de Groot, R. Gagnon and L. Taillefer: Phys. Rev. Lett. **72** (1994) 3606.

52) K. Dembinski, M. Gervais, P. Odier and J. P. Coutures: J. Less-Common Met. **164/165** (1990) 177.

53) B.W.Wanklyn, C. Chen B. E. Watts, P. Haycock, F. Pratt, P. A. J. de Groot and G. P. Rapson: Solid State Commun. **66** (1988) 441.

54) A. Ono, H. Nozaki and Y. Ishizawa: Jpn. J. Appl. Phys. **27** (1988) L340.

55) S. Bosi, T. Puzzer, G. J. Russel and K.N.R. Taylor: J. Mater. Sci. Lett. **8** (1989) 497.

56) P. Murugaraj, J. Maier and A. Rabenau: Solid State Commun. **71** (1989)

167.

57) J. S. Abell, C. N. W. Darligton, C. A. Hollin, E. M. Forgan, D. A. O'Connor and S. D. Sutton: Physica C **162-164** (1989) 909.

58) T. Hibiya, S. Imoto, T. Saito, Y. Nakabayashi and M. Sakonjyu: J. Cryst. Growth **102** (1990) 862.

59) F. Gencer and J. S. Abell: J. Cryst. Growth **112** (1991) 337.

60) K. Watanabe: J. Cryst. Growth **114** (1991) 269.

61) R. Boutellier, B. N. Sun, H. J. Scheel and H. Schmid: J. Cryst. Growth **96** (1989) 465.

62) H. Takei and H. Takeya: *Superconducting Materials* (Jpn. J. Appl. Phys. 1988) Series 1 p.61.

63) T. Ito, H. Takagi, S. Ishibashi, T. Ido and S. Uchida: Nature **350** (1991) 596.

64) S. Kambe, K. Kitazawa, A. Fufuda, M. Naito, I. Tanaka and H. Kojima: Physica C **160** (1989) 35.

65) S. Kambe, M. Naito, K. Kitazawa, I. Tanaka and H. Kojima: Physica C **160** (1989) 243.

66) S. Martin, A. T. Fiory, R. M. Fleming, L. F. Schneemeyer and J. V. Waszcak: Phys. Rev. Lett. **60** (1988) 2194.

67) S. H. Bloom, M. V. Kuric, Y. S. Yao, R. P. Guertin, D. Nichols, C. Tee, A. Kebede, J. E. Crew, T. Mihalisin, G. N. Myer and P. Shulottmann: *High-temperature Superconductors* (MRS 1988) p.19.

68) R. B. van Dover, R. J. Cava, B. Batlogg and E. A. Rietman: Phys. Rev. B **35** (1987) 5337.

69) K. Kitazawa, S. Kambe, M. Naito, I. Tanaka and H. Kojima: Jpn. J. Appl. Phys. **28** (1989) L555.

70) C. P. Bean: Phys. Rev. Lett. **8** (1962) 250.

71) A. M. Campbell and J. E. Evetts: Adv. Phys. **21** (1972) 199.

72) L. F. Schneemeyer, E. M. Gyorgy and J. V. Waszczak: Phys. Rev. B **36** (1987) 8804.

73) V. V. Moshchalkov, A. A. Gippius, A. A. Zhukov, H. H. Nyan, V. I. Voronkova and V. K. Yanovskii: Physica C **165** (1990) 62.

74) M. R. Beasley, R. Labusch and W. W. Webb: Phys. Rev.**181** (1969) 682.

75) M. P. Maley, J. O. Willis, H. Lessure and M. E. McHenry: Phys. Rev. B **42** (1990) 2639.

76) M. E. McHenry, S. Simizu, H. Lessure and M. P. Maley, J. Y. Coulter, I. Tanaka and H. Kojima: Phys. Rev. B **44** (1991) 7614.

77) P. J. Kung, M. P. Maley, M. E. McHenry, J. O. Willis, J. Y. Coulter, M. Murakami and S. Tanaka: Phys. Rev. B **46** (1992) 6427.

78) G. Deutcher and K. A. Müeller: Phys. Rev. Lett. **59** (1987) 1745.

79) P. H. Kes: Physica C **153-155** (1988) 1121.

80) E. V. Thuneberg: Cryognics **29** (1989) 236.

81) I. N. Khulustikov and A. I. Buzdin: Adv. Phys **36** (1987) 271.

82) A. A. Abrikosov: *Fundamentals of the Theory of Metals* (North-Holland, Amsterdam, 1988) p. 489.

83) M. Oussena, P. A. J. de Groot, S. J. Porter, R. Gagnon and L. Taillefer: Phys. Rev. B **51** (1995) 1389.

84) G. Blatter, J. Rhyner and V. M. Vinokur: Phys. Rev. B **43** (1991) 7826.

国際単位系 (SI) と換算表

表1　SI基本単位および補助単位

量	名称	記号
長さ	メートル	m
質量	キログラム	kg
時間	秒	s
電流	アンペア	A
熱力学温度	ケルビン	K
物質量	モル	mol
光度	カンデラ	cd
平面角	ラジアン	rad
立体角	ステラジアン	sr

表2　SIと併用される単位

名称	記号
分，時，日	min, h, d
度，分，秒	°, ′, ″
リットル	l, L
トン	t
電子ボルト	eV
原子質量単位	u

1 eV=1.60218×10^{-19}J

1 u=1.66054×10^{-27} kg

表3　固有の名称をもつSI組立単位

量	名称	記号	他のSI単位による表現
周波数	ヘルツ	Hz	s^{-1}
力	ニュートン	N	m·kg/s^2
圧力，応力	パスカル	Pa	N/m^2
エネルギー，仕事，熱量	ジュール	J	N·m
工率，放射束	ワット	W	J/s
電気量，電荷	クーロン	C	A·s
電位，電圧，起電力	ボルト	V	W/A
静電容量	ファラド	F	C/V
電気抵抗	オーム	Ω	V/A
コンダクタンス	ジーメンス	S	A/V
磁束	ウェーバ	Wb	V·s
磁束密度	テスラ	T	Wb/m^2
インダクタンス	ヘンリー	H	Wb/A
セルシウス温度	セルシウス度	℃	
光束	ルーメン	lm	cd·sr
照度	ルクス	lx	lm/m^2
放射能	ベクレル	Bq	s^{-1}
吸収線量	グレイ	Gy	J/kg
線量当量	シーベルト	Sv	J/kg

表4　SIと共に暫定的に維持される単位

名称	記号
オングストローム	Å
バーン	b
バール	bar
ガル	Gal
キュリー	Ci
レントゲン	R
ラド	rad
レム	rem

1 Å= 0.1 nm=10^{-10}m

1 b=100 fm^2=10^{-28} m^2

1 bar=0.1 MPa=10^{5}Pa

1 Gal=1 cm/s^2=10^{-2}m/s^2

1 Ci=3.7×10^{10}Bq

1 R=2.58×10^{-4}C/kg

1 rad=1 cGy=10^{-2}Gy

1 rem=1 cSv=10^{-2} Sv

表5　SI接頭語

倍数	接頭語	記号
10^{18}	エクサ	E
10^{15}	ペタ	P
10^{12}	テラ	T
10^9	ギガ	G
10^6	メガ	M
10^3	キロ	k
10^2	ヘクト	h
10^1	デカ	da
10^{-1}	デシ	d
10^{-2}	センチ	c
10^{-3}	ミリ	m
10^{-6}	マイクロ	μ
10^{-9}	ナノ	n
10^{-12}	ピコ	p
10^{-15}	フェムト	f
10^{-18}	アト	a

(注)

1. 表1－5は「国際単位系」第5版，国際度量衡局 1985年刊行による。ただし，1 eVおよび1 uの値はCODATAの1986年推奨値によった。
2. 表4には海里，ノット，アール，ヘクタールも含まれているが日常の単位なのでここでは省略した。
3. barは，JISでは流体の圧力を表わす場合に限り表2のカテゴリーに分類されている。
4. EC閣僚理事会指令ではbar，barnおよび「血圧の単位」mmHgを表2のカテゴリーに入れている。

換算表

力	N(=10^{5}dyn)	kgf	lbf
	1	0.101972	0.224809
	9.80665	1	2.20462
	4.44822	0.453592	1

粘度　1 Pa·s(N·s/m^2)=10 P(ポアズ)(g/(cm·s))

動粘度　1 m^2/s=10^{4}St(ストークス)(cm^2/s)

圧力	MPa(=10 bar)	kgf/cm^2	atm	mmHg(Torr)	lbf/in^2(psi)
	1	10.1972	9.86923	7.50062×10^3	145.038
	0.0980665	1	0.967841	735.559	14.2233
	0.101325	1.03323	1	760	14.6959
	1.33322×10^{-4}	1.35951×10^{-3}	1.31579×10^{-3}	1	1.93368×10^{-2}
	6.89476×10^{-3}	7.03070×10^{-2}	6.80460×10^{-2}	51.7149	1

エネルギー・仕事・熱量	J(=10^{7}erg)	kgf·m	kW·h	cal(計量法)	Btu	ft·lbf	eV
	1	0.101972	2.77778×10^{-7}	0.238889	9.47813×10^{-4}	0.737562	6.24150×10^{18}
	9.80665	1	2.72407×10^{-6}	2.34270	9.29487×10^{-3}	7.23301	6.12082×10^{19}
	3.6×10^6	3.67098×10^5	1	8.59999×10^5	3412.13	2.65522×10^6	2.24694×10^{25}
	4.18605	0.426858	1.16279×10^{-6}	1	3.96759×10^{-3}	3.08747	2.61272×10^{19}
	1055.06	107.586	2.93072×10^{-4}	252.042	1	778.172	6.58515×10^{21}
	1.35582	0.138255	3.76616×10^{-7}	0.323890	1.28506×10^{-3}	1	8.46233×10^{18}
	1.60218×10^{-19}	1.63377×10^{-20}	4.45050×10^{-26}	3.82743×10^{-20}	1.51857×10^{-22}	1.18171×10^{-19}	1

1 cal = 4.18605 J (計量法)
= 4.184 J (熱化学)
= 4.1855 J (15 °C)
= 4.1868 J (国際蒸気表)

仕事率　1 PS (仏馬力)
= 75 kgf·m/s
= 735.499 W

放射能	Bq	Ci
	1	2.70270×10^{-11}
	3.7×10^{10}	1

吸収線量	Gy	rad
	1	100
	0.01	1

照射線量	C/kg	R
	1	3876
	2.58×10^{-4}	1

線量当量	Sv	rem
	1	100
	0.01	1

(86年12月26日現在)

GROWTH OF LARGE ISOMETRIC $YBa_2Cu_3O_x$ SINGLE CRYSTALS AND THEIR FLUX PINNING PROPERTIES